JONATHAN SCHÄFER

ATOMISTIC SIMULATIONS OF PLASTICITY IN NANOCRYSTALLINE ALLOYS

Zur Erlangung des akademischen Grades des Doktors der Ingenieurwissenschaften (Dr.-Ing.) genehmigte Dissertation vorgelegt von Dipl.-Ing. Jonathan Schäfer, geboren in Darmstadt

Fachgebiet Materialmodellierung
Fachbereich Material- und Geowissenschaften
Technische Universität Darmstadt

Referent: Prof. Dr. Karsten Albe,
Technische Universität Darmstadt

Korreferent: Prof. Dr.-Ing. Horst Hahn,
Technische Universität Darmstadt

Tag der Einreichung: 13. Juli 2012
Tag der mündlichen Prüfung: 31. Januar 2013

Darmstadt, 2013
D 17

ATOMISTIC SIMULATIONS OF PLASTICITY IN NANOCRYSTALLINE ALLOYS

JONATHAN SCHÄFER

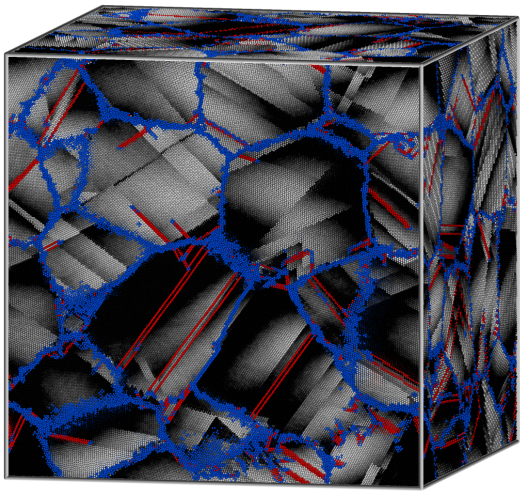

Dissertation

2012

On the cover: Deformed nanocrystalline Ni–Fe alloy with an average grain size of 15 nm. Gradient gray scale corresponds to the local displacement, grain boundary atoms are highlighted in blue, twinning and faulting atoms are shown in red.

CONTENTS

LIST OF FIGURES

LIST OF TABLES

LIST OF ABBREVIATIONS

BMG	bulk metallic glass
CD-EAM	concentration-dependent embedded atom method
CG	coarse grained
CNA	common neighbor analysis
CSL	coincidence site lattice
CSRO	chemical short range order
DSC	differential scanning calorimetry
DXA	dislocation extraction algorithm
EAM	embedded atom method
fcc	face centered cubic
FS	Finnis-Sinclair
GB	grain boundary
IGC	inert gas condensation
MC	Monte-Carlo
MD	molecular dynamics
NC	nanocrystalline
NN	nearest neighbor
ODDA	on-the-fly dislocation detection algorithm
SPD	severe plastic deformation
SRO	short range order
VP	Voronoi polyhedron

ABSTRACT

Due to their extraordinary mechanical properties, the field of research on nanocrystalline metals and their alloys has been steadily growing since the early synthesis attempts [1]. Several recent reviews summarize the subject [2, 3, 4, 5, 6, 7, 8]. Especially for the case of alloyed systems, however, a strong link between the macroscopic mechanical properties and the atomistic mechanisms being at the heart of a materials response to an external load is still missing.

For addressing this problem, atomistic simulation techniques are used in this work. Several metals and their alloys are studied. The main emphasis is on elucidating generalized structure-property relationships for nanocrystalline microstructures.

In the first part, an introduction to the subject and the employed methods is given. Then, the sample preparation technique is explained and the introduction of solute atoms into a nanocrystalline model structure is discussed, where several methods are compared. Characterization of the nanocrystalline alloys with focus on the elemental distribution in the microstructure shows that a high density of grain boundaries can drastically affect the local composition and the phase stability range for a given alloy.

Uniaxial deformation simulations of the nanocrystalline alloys allow us to identify the atomic processes, which control the macroscopic mechanical behavior. Modulating the structural feature, which controls the strength i.e. the free volume in the grain boundaries by the introduction of different amounts of segregating solutes helps to develop a new scaling law, which depends not only on the grain size but also on grain boundary energy and the grain boundary relaxation.
The variation of the concentration of solutes in different parts of the microstructure, where the composition in the grain interior and the grain boundaries is studied independently, reveals that conventional solid solution hardening is absent in nanocrystalline alloys. This supports the finding that the relaxation state of the grain boundary is controlling the strength of the material.
After showing, that dislocation processes in the grain interior do not control the strength of the structures, their role for the ductility of the prepared alloys is tested by introducing intermetallic grains into the microstructure. Thus, the deformation is restricted to processes in the grain boundaries. Here it is demonstrated, that the ductility of the samples is strongly affected by the grain size while the strength controlling parameter is identical to miscible and segregating alloys.

The delicate interplay between the different deformation processes mediated by the grain boundary is investigated for the competition between normal grain boundary motion and mesoscopic grain boundary sliding. It is analyzed, how this competition is altered by segregating solutes and under which conditions each mechanism is contributing to plastic deformation in nanocrystalline metals and alloys.

The results by conventional molecular dynamics simulations are affected by the very high strain rates. Combining molecular dynamics with Monte Carlo simulations can overcome this limitation and allows to explore, how different deformation mechanisms are influenced by the simulation conditions. The Monte Carlo algorithm accounts for local relaxation by trial exchanges, shortcutting diffusional processes. It is shown how the balance between different contributions to plastic deformation depends on the local relaxation and how conventional molecular dynamics straining simulations overestimate the contribution by dislocation processes.

The simulation of thermally activated processes in large systems with molecular dynamics is in general complicated by the limited timescales. Here, designing thermally stable microstructures offers the possibility to study the deformation processes at elevated temperatures without inducing grain growth. Thus, grain boundary creep in nanocrystalline model structures can be studied, if appropriate microstructures are used. Here, the effect of solute atoms is analyzed, where different compositions and different material systems are compared. The results show, how solute atoms affect the creep compliance of a nanocrystalline alloy. The atomic mechanisms governing the mass transport through the grain boundaries are discussed and compared to the processes governing plastic flow in bulk metallic glasses.

Part I

INTRODUCTION

1

NANOCRYSTALLINE METALS AND ALLOYS

1.1 STRENGTHENING METALS

The strength and ductility of metals (of materials in general) are inherently related to the processes governing the way how atoms move past one another [9]. In conventional coarse grained (CG) face centered cubic (fcc) metals and alloys at ambient temperature, this mostly occurs by the multiplication and movement of dislocations [10, 11]. Thus, the movement of dislocations and their interaction or interactions with other defects controls the strength and ductility of CG metals. Methods for strengthening this materials therefore rely on strategies that control the generation, and interaction of dislocations and defects [12].

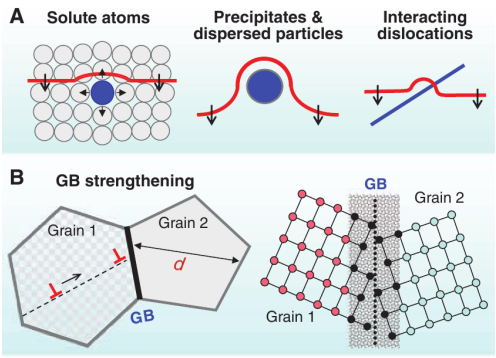

Figure 1: Strategies for strengthening of materials. (Reprint from Science **349**, (2009), © 2009, with permission from the American Association for the Advancement of Science.)

Fig. 1 shows examples of strengthening methods for crystals and alloys, relying on the interaction between dislocations and A) solute atoms, precipitates or other dislocations and B) grain boundaries (GBs).

The fact that GBs provide a barrier for dislocation slip is used to strengthen metals by increasing the density of GBs in the material i.e. decreasing the average grain size. Here, for CG metals a scaling between the yield strength and $1/\sqrt{d}$, where d refers to the average grain diameter (the Hall-Petch law [13, 14]) is commonly observed.

Extrapolating this scaling law into the nanometer grain size regime results in a yield strength drastically increased as compared to the CG material. And

indeed, a severe increase in strength is observed in experiment and simulation for nanocrystalline (NC) metals and alloys [2, 3, 4, 5, 6, 7, 8]. When the grain size is decreased into the nanometer regime, however, the deformation mechanisms as well as the macroscopic behavior change, where limited ductility is frequently reported [2, 3, 4, 5, 6, 7, 8]. The development of a structure-property relationship, where the atomic processes are resolved, is therefore a prerequisite for designing NC alloys with high strength and ductility.

1.2 NANOCRYSTALLINE METALS

1.2.1 *Definition and experimental preparation*

NC metals are polycrystalline structures with a mean grain size below 100 nm. The microstructure therefore contains a significant volume fraction of interfacial regions separated by nearly-perfect crystals [1].

Experimental methods to prepare NC metals can be categorized into bottom-up (or two-step) and top-down (or one-step) approaches [15]. In bottom-up approaches, nanosized particles are prepared (e.g. by inert gas condensation (IGC)) and then compacted to form a bulk NC material [16]. In top-down approaches, a conventional polycrystalline bulk material is heavily deformed by severe plastic deformation (SPD) [17, 18]. Depending on the amount of imposed strain, this can lead to the formation of nanosized grains within the microstructure.

1.2.2 *Mechanical properties of nanocrystalline metals*

The mechanical properties of NC metals are controlled by the high density of GBs in the microstructure [1, 2, 19, 20, 21, 22, 23]. Several reviews summarize the current understanding of this material class [2, 3, 4, 5, 6, 7, 8], much of which has derived also from molecular dynamics (MD) simulations.

One striking observation is, that different studies on the same metal or alloy with a comparable average grain size often report different behaviors. This is due to the fact that the details of simply preparing NC systems, either by experiments or simulation [5], matter greatly in their response to applied stresses. Furthermore, it was shown that grain size alone is not sufficient to fully describe a NC material of a given composition [24, 25]. Several experimental and simulation studies have pointed out that the strength of NC materials in the lower nanometer regime can be influenced by both thermal annealing [26, 27, 28, 29] and the addition of solute or impurities [26, 27, 30, 31, 32, 33]. Compared to the CG counterparts, fully dense NC metals often show drastically enhanced yield stresses [8].

The observations regarding the ductility of NC metals differ significantly. Here, from limited tensile elongation [8] over reasonable ductility [34] to near perfect

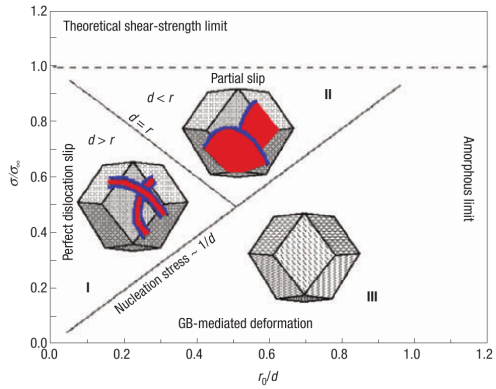

Figure 2: Deformation mechanism map for NC fcc metals expressed in reduced units of stress and inverse grain size, where r_0 is the equilibrium splitting distance between two Shockley partial dislocations at zero stress and σ_∞ is the resolved shear stress at which the splitting distance becomes infinitely large. (Reprint from Nature Materials **3**, (2004), © 2004, with permission from Nature Publishing Group.)

elastoplasticity [35] a wide range of characteristics are reported. Also the ductility of NC metals and alloys can be masked by imperfections introduced during synthesis or later heat treatment [36]. Weissmüller and co-workers showed, that the limited ductility in tension, however, is due to the low strain hardening exponent and the low strain rate sensitivity and not due to pores or flaws [37]. In another study it was emphasized that NC metals are intrinsically ductile as long as strain localization is suppressed [38]. Promising routes to benefit from the high strength of NC material may be a gradient grain size distribution as demonstrated by Lu and co-workers [38] or alternative ways to remove or delay plastic instabilities by designing strain hardening or strain rate hardening schemes as discussed by Wang and Ma [39]. High strength and high ductility in NC metals might also be achieved by SPD as demonstrated by Valiev et al. [40]. Here, the amount of strain during deformation controls the state of the GBs as well as the homogeneity of the grain size and shape and therefore the ductility of the material [40]. Also regarding the ductility of NC metals, it was observed, that grain size alone is not sufficient to characterize a microstructure, where first studies suggest that the intrinsic ductility is unexpectedly independent of the microstructure over the grain size range from 10-80 nm unlike conventional CG metals [41]. Another point, which needs to be considered is the mode of deformation. Birringer and co-workers reported that NC metals show a strong dependence on the loading conditions and go ductile under shear deformation [42]. The explanation for most of the observations goes hand in hand with a change in the underlying deformation mechanisms (Sec. 1.3), where the high density of GBs appears to play the key role. The significant contribution by GB mediated deformation

mechanisms motivated studies, where the temperature range for the occurrence of superplastic deformation was explored as a function of grain size [34, 43]. Here, superplastic deformation and non-negligible creep deformation was observed in NC Cu and Ni, respectively, even at room temperature [34, 44]. As proposed by Lu et al., this may offer innovative material processing techniques for modern industry [34].

Another intriguing often reported feature of NC metals is that they strengthen with decreasing grain size down to very small grain sizes (20-30 nm), but here they reach a maximum in yield strength. Further reduction in grain size results in a plateau or in softening. This so-called "inverse Hall-Petch" behavior has been widely discussed [45, 46], but the underlying reasons have remained largely a matter of speculation [4]. This lack of understanding is partly caused by the difficulty in controlling and characterizing the structure and purity of NC metals, particularly when their grain sizes fall below 30 nm.

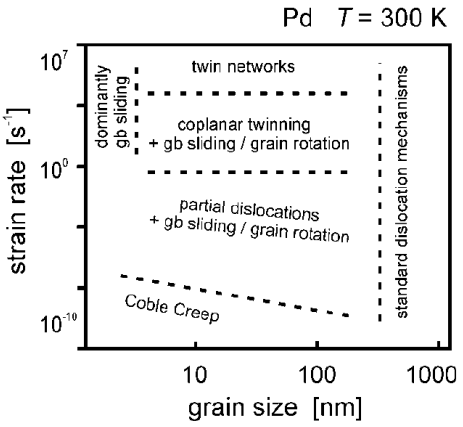

Figure 3: Deformation mechanism map for NC Pd. (Reprint from Advanced Engineering Materials 7, (2005), © 2005, with permission from Wiley-VCH.)

Reasons for the breakdown of the Hall-Petch behavior could be that collective effects vanish and strain proceeds through uncorrelated events of individual dislocation nucleation and propagation [47]. It was proposed by Li, that impurity segregation and grain boundary porosity also could explain the grain size dependence of the yield stress [48]. A study by Lu and coworkers on NC Cu even suggests that the Hall-Petch relation is valid down to grain sizes as small as 10 nm [49].

For pure NC metals deformation mechanism maps such as in Fig. 2 by Yamakov et al. [21] and in Fig. 3 by Weissmüller and Markmann [22] are evolving, where also computer simulations contributed to the understanding [50]. They can, however, not aspire to represent a complete picture but rather represent a snapshot of the available knowledge [22]. The large number of available deformation mechanisms (Fig. 3, Fig. 4) and their interaction is hampering the general understanding of deformation in NC metals and alloys [22].

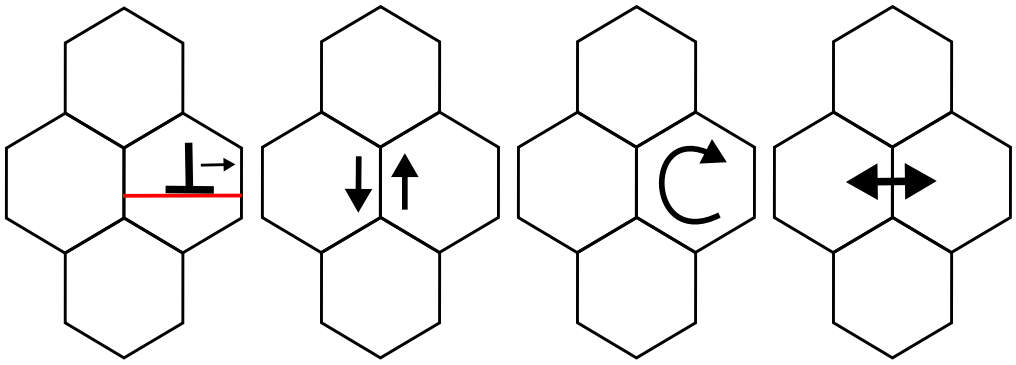

Figure 4: Schematics of potential deformation processes in NC fcc metals including a) dislocation emission from GBs, b) GB sliding, c) grain rotation and d) stress coupled GB motion.

1.3 ATOMISTIC SIMULATIONS AND DEFORMATION MECHANISMS

MD simulations have proved very helpful in providing insight into the strength of NC materials at the atomistic level as pointed out by van Swygenhoven [51]. Gumbsch and co-workers furthermore showed, how MD simulations play a crucial role in advancing our understanding of mechanical behavior [52]. Regarding the macroscopic mechanical properties, MD simulations on NC materials, which were mostly carried out for pure samples [53, 54, 55, 56, 50], hardly report a lack of ductility as the grain size is reduced. Only for NC body centered cubic metals some intergranular fracture at low strains is observed [57, 58]. MD simulations on fcc metals also support the existence of a cross-over from Hall-Petch strengthening to "inverse Hall-Petch" softening [53, 54, 55, 56, 50], coinciding with a potential transition in the active deformation mechanism at grain sizes around 15 nm as reported by Schiøtz [59].

Several different deformation mechanisms of NC metals were identified by MD simulations [54, 3, 60, 2]. Distinct from CG metals, they are mainly mediated by the high density of GBs in NC microstructures. Here, the GBs can act as sources and sinks for lower-dimensional defects and can contribute to plastic deformation by their multi-directional response to applied stresses [21, 2]. It was revealed that e.g. dislocation emission from and absorption in GBs (Fig. 4 (a)), GB sliding (Fig. 4 (b)) and grain rotation (Fig. 4 (c)), twinning and faulting as well as diffusional creep and GB migration or stress coupled GB motion (Fig. 4 (d)) are potential deformation mechanisms operational in NC fcc metals [60, 61, 8, 3, 2].

The balance between the contributions of the different distinct mechanisms as well as the identification of the limiting process is, however, still a matter of debate. The delicate interplay between the different mechanisms, which need

(to some extend) act in synergistic ways due to geometrical constraints, is also not fully resolved. On the one hand side, it was reported by Schiøtz et al. from simulations that at the smallest grain sizes mainly GB sliding contributes to plastic deformation, even at zero temperature [62], where the sliding of the GB is thought to be triggered by atomic shuffling and to some extent free volume migration [63]. Here, a close relationship between atomic-scale relaxation and inter-grain deformation mechanisms is suggested [64]. On the other hand, it was stated by van Swygenhoven et al. that the most important suggestion resulting from MD simulations on NC fcc metals is that even in the absence of dislocation sources in the grain interior, dislocations still play an important role in the deformation [63]. Here, GBs can act as alternative sources and sinks [53], a concept which was introduced well before the era of NC metals [65, 66].

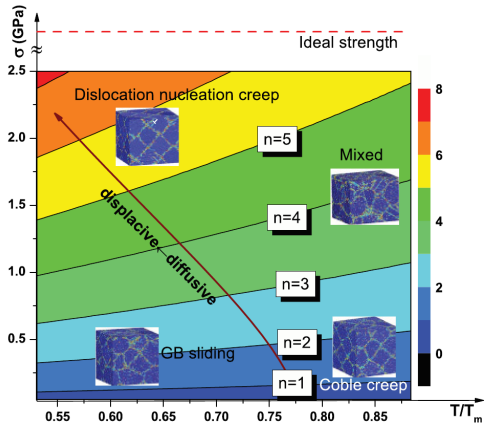

Figure 5: Deformation mechanism map for NC Cu by MD. (Reprint from Physical Review B **84**, (2011), © 2011, with permission from the American Physical Society.)

Also not completely resolved is, how the results by MD straining simulations are affected or controlled by the high strain rates, adherent to this simulations. It is without debate that the extrapolation to the experimental regime requires a clear understanding of the modeling technique, a detailed structural characterization of the simulated sample [67] and careful consideration of the temperature dependence of the deformation mechanisms [68]. It is, however, not resolved, whether this constraint allows for the development of deformation mechanism maps by MD simulations such as in Fig. 5 [69] or whether atomistic simulations alone are at the present not suited to set up deformation mechanism maps analogous to constitutive plasticity [51] where the mechanisms are quantified according to the applied stresses, the grain size, strain rates and temperature.

Experimentally, the active deformation mechanisms are analyzed by identifying the respective "kinetic fingerprint" (i.e. strain rate sensitivity and activation volume) of deformation as discussed by Meyers et al. [2] or Wei [70]. Some results indicate that GB sliding is the dominant deformation mechanism for grain sizes around (and below) 10 nm in various fcc metals [71, 72, 73]. Other studies analyzing strain rate sensitivity and activation volume in NC Cu (10 nm) suggest that GB mediated processes are active, but not dominant [49]. Alternative rate-controlling mechanisms accommodating the plastic flow could be the interaction of dislocations with grain boundaries [74], the nucleation of partials [75], GB shear promoted by a pile-up of dislocations [76] or dislocation-accommodated

boundary sliding [46]. The evolution of the strain rate sensitivity as well as the temperature dependence of the apparent activation volume seem to coincide with GB processes such as migration, sliding and dislocation nucleation [77, 76], while the evolution of the grain size in other samples yields evidence for stress coupled GB motion [9, 78, 38, 79].

For dislocation based mechanisms, a transition to partial dislocation mediated plasticity can be proven by the detection of twins for metals where the formation of deformation twins does not occur at larger grain sizes such as Al [80]. The observation that dislocation processes are different for the case of NC metals is also consistent with in-situ x-ray diffraction data, which can be interpreted in terms of dislocation emission and absorption from the GBs, while no dislocation debris is stored inside the grains during deformation, which also falls in line with the absence of substantial work hardening [81]. The energy barrier for dislocation nucleation and twinning in fcc metals, however, depends not only on the grain size but also on the deformation conditions such as temperature and strain-rate [82, 68].

Regarding the delicate interplay between the different deformation mechanisms, it apparently has to be considered that the transition from intragranular to intergranular plasticity is determined not only by the grain size. Also other factors, like the stacking fault energy or the nature of the GBs [83, 56] influence the individual contribution to macroscopic plastic deformation. The individual contributions are furthermore dependent on the deformation conditions, where it is observed, that at increasing strain rate plastic deformation shifts from GB creep mechanisms to grain interior plasticity [84].

1.4 NANOCRYSTALLINE ALLOYS

In pure metals, grain sizes in the nanometer range are difficult to stabilize, whence (segregating) solutes can been used to prevent grain growth, i.e. tailor the grain size [85, 86, 87, 88, 37] as demonstrated also by computer simulations mainly by Millett et al. [89, 90, 91, 92]. Solute segregation to the GB can decrease the GB energy to zero. This leads to an equilibrium grain size, which depends on the concentration of segregating solute as shown by Trelewicz and Schuh [93].

Furthermore, miscible solute atoms in principle allow to specially tune certain material properties such as the generalized planar fault energy (GPFE) of the bulk material [94, 89, 90, 91, 95, 96] which is in turn considered to control dislocation nucleation and slip in NC fcc materials [75, 97] and affects the twinability [98, 99, 100, 101].

Moreover, it is well known that the GB structure and energy depend on the type and concentration of solutes [102], and therefore chemical equilibration of GBs should also affect the properties of alloyed nanocrystals.

1.4.1 *Mechanical properties of nanocrystalline alloys*

Regarding the effect of alloying on the mechanical properties of NC microstructures, Schuh and co-workers showed, that addition of alloys significantly influences the mechanical response [103]. Substitutional solute addition can increase the strength of the material to very high levels, which is not expected based on traditional solid solution strengthening [103]. Alternatively, an increase in hardness (strength) can be achieved by annealing and GB segregation [104]. Here, Derlet et al. report, that solutes and impurities can have a dramatic effect on atomic activities in the GBs [67]. Furthermore, alloying may shift the breakdown of the Hall-Petch strengthening to finer grain sizes [105].

The effect of impurities, commonly present in experimental samples, is rarely considered in the atomistic simulations [6, 51]. A small increase in strength on adding 2 at.% Fe (i.e., average sample concentration) to the GB was reported for NC Cu by Caro et al. [32]. Furthermore, Saxena and co-workers showed, that a small increase in the strength (by about 10%) of NC Cu could be gained by adding up to 1 at.% Sb to the GBs [33]. A stronger increase was observed by Mishin and co-workers, who randomly introduced Ta into the GBs of NC Cu [106].

Here, however, significant progress still needs to be made understanding even individual processes such as the dislocation activity for the case of a heterogeneous composition [107].

The interplay between different deformation mechanisms operational in NC metals is not fully explored (Sec. 1.3). The dependence on the presence of solute atoms on the hierarchy of deformation mechanisms is often not even considered.

The interplay between distinct modes of plasticity, operational in NC metals may, however, be affected by the presence of solutes [108, 109, 110]. The nucleation of partial dislocations, for instance, is stimulated by miscible solutes as shown by MD simulations [111]. For the case of solutes in the vicinity of the GB it was shown experimentally by Hemker and co-workers [110] and by Gottstein and co-workers [112], that they can hinder normal GB motion. This is supported by results from simulations by van Swygenhoven and co-workers, showing that solutes increase the necessary stress for coupled GB motion [113, 109]. Additionally, Millett et al. observed by MD simulations, that segregated solutes can increase the GB sliding resistance [108].

1.5 OPEN QUESTIONS

Based on the existing knowledge on the structure and mechanical properties of NC metals and their alloys as presented above, several open questions can be formulated regarding the simulation of NC alloys and their mechanical properties. These questions will be addressed in the following. The order of the topics given below is a guideline for the structure of the presented work.

Simulation of NC alloys

- **What is a suitable simulation procedure to introduce solute atoms into a NC microstructure?**
  Several procedures to create NC single-element microstructures for MD simulations have been developed. For studying alloyed systems, no general preparation route has been established. Here, different attempts are possible, which might show an effect on the macroscopic behavior. (Chap. 3)

- **What is the equilibrium elemental distribution in a NC microstructure for the case of a miscible system?**
  The elemental distribution also of a miscible system can deviate from the global composition in the vicinity of a GB. Here, the employed modeling scheme enables to explore an equilibrated distribution for a NC microstructure. (Chap. 4)

- **Does a NC microstructure change the phase diagram of an alloy?**
  A microstructure with a nanometer grain size can have a significant effect on the phase diagram i.e. the phase stability due to the excess in interfacial (GB) area. For an alloy with an ordering tendency, we compare, how the stability range of an intermetallic phase is affected by a NC microstructure. (Chap. 4)

- **How does the excess volume and the GB energy correlate for NC metals and how do they change with composition?**
  The excess volume in a given microstructure as well as the GB energy depend on grain size and the type of the GBs in a delicate manner. Additionally, both are affected by the introduction of solute atoms into the GB. How they scale with the concentration of solute atoms needs to be discussed. (Chap. 4)

Grain boundary mediated plasticity

- **How do intrinsic material parameter affect the mechanical response of a NC alloy?**
  For a CG material, the deformation behavior strongly depends on intrinsic material parameters such as shear modulus, stacking fault energy, twinnability, etc.. Most of them vary with composition for a given binary alloy (Chap. 5). For the case of a NC alloy, it is neither established, whether the same parameters influence the mechanical behavior, nor whether intrinsic material parameters have an effect at all. (Chap. 6)

- **Which parameter does control the strength of NC metals and alloys?**
  It is frequently reported, that established scaling laws for CG metals such as the Hall-Petch behavior fail to fully describe the properties of NC structures,

i.e. that the grain size alone is not a sufficient parameter. Other than that it is unknown, which properties may have a crucial influence on macroscopic properties. (Chap. 6)

- **How are the mechanical properties affected by the way, solute atoms are introduced?**
  Experimentally as well as in simulations, there are different ways to introduce solute atoms into a given microstructure as well as different successive treatments, leading to a differing elemental distribution (Chap. 4). How the elemental distribution especially in the vicinity of GBs affects the macroscopic properties of an NC needs to be resolved. (Chap. 6)

- **How can the state of the GBs be modulated?**
  For testing the influence of the state of the GB on the mechanical properties of a NC microstructure, it needs to be systematically modulated. This can be done by introducing solutes into the GBs. Here, the effect of different solutes and the respective concentration needs to be explored and understood. (Chap. 7)

- **Is there solid solution hardening in NC microstructures?**
  For CG alloys, the way how miscible solutes can increase the resistance of the crystal lattice against dislocation motion (Fig. 1) is mostly understood. For NC alloys, where it is not fully resolved which parameters control the strength of the material, the question arises whether a change of composition in the grain interior has an effect on the macroscopic mechanical properties. (Chap. 8)

- **How do intermetallic systems with a NC microstructure deform?**
  For NC metals, it was reported that a significant contribution to plastic deformation is accounted for by dislocation slip. For intermetallic systems the question arises, whether they are brittle also with a nanometer grain size because of a lack of dislocation and/or a low dislocation mobility. Furthermore it needs to be explored whether similar parameters control the strength of the material as observed for other alloys. (Chap. 9)

Coupled motion and mesoscopic GB sliding

- **Does coupled motion contribute to deformation in NC metals and alloys?**
  From bicrystal simulations, it was shown that stress coupled GB motion can lead to a shearing of two crystals versus each other. From experimental results on NC metals, it was reported, that under the influence of an applied stress grain size increases more drastically than can be explained by curvature driven grain growth. Here, it needs to be explored whether

and how stress coupled GB motion contributes to plastic deformation in NC microstructures. (Chap. 10)

- **How does coupled motion compete with mesoscopic GB sliding?**
  For NC metals it was supposed, that GBs can align themselves, leading to GB sliding on a mesoscopic scale. Experimental evidence for aligned GBs in deformed microstructures supports this. Stress coupled GB motion and mesoscopic sliding, however, exclude each other. Here, it needs to be resolved how the two competing processes interact. (Chap. 10)

- **What are the atomistic processes of coupled motion in a general high angle GB?**
  From bicrystal simulations of special coincidence site lattice (CSL) boundaries, it could be shown which structural units are responsible for the normal motion of the GB. For stress coupled GB motion occurring in a NC microstructure, it needs to be understood whether the atomistic mechanisms are similar to the ones in CSL boundaries and how the findings from the bicrystals can be transferred. (Chap. 10)

- **How is the competition between mesoscopic sliding and coupled motion affected by solutes?**
  It was shown by experiment and bicrystal simulation, that solutes in the vicinity of the GB can hinder stress coupled GB motion as well as GB sliding. Here, it needs to be understood, how solutes affect the competition between stress coupled motion and mesoscopic sliding for the case of a NC microstructure. (Chap. 11)

- **Is the effect independent of the alloying procedure?**
  Also for the competition of coupled motion with mesoscopic GB sliding it is of interest to resolve, whether the way the solute atoms are introduced changes their interaction regarding the competition between mesoscopic GB sliding and normal GB motion. (Chap. 11)

- **What is the effect of solutes with differing segregation tendency?**
  Whether the effect of segregating solutes on the competition between mesoscopic GB sliding and normal GB motion can be transferred to other alloys with a segregation tendency needs to be discussed. Here, one has to understand, which parameters (heat of mixing, size mismatch, etc.) controls the effect on the competing mechanisms in a sensible manner. (Chap. 11)

Hierarchy of deformation processes

- **Does the hierarchy of deformation processes change with the deformation conditions?**

MD simulations have contributed significantly to identify and understand the mechanisms contributing to the deformation of NC microstructures. The high strain rates, adherent to MD simulations might, however, change the hierarchy between the contributing processes with individual activation enthalpies and activation volumes. Here it needs to be explored, how the hierarchy of the deformation processes changes with the deformation conditions. (Chap. 12)

- **Can the short MD time scale be overcome?**
  Crucial for understanding the effect of the peculiar deformation conditions in MD straining simulations on the various contributing processes is to overcome the short time scales. This can be done by using other simulation techniques together with MD simulations. Here, e.g. MC trial exchanges can overcome the time scales which would be necessary for thermally activated processes such as diffusion. (Chap. 12)
- **Do the contributions change, when local relaxation is accounted for?**
  When local relaxation by diffusional processes is accounted for it then needs to be resolved whether and how the contribution by individual processes changes during straining. (Chap. 12)
- **How are GB mediated processes affected by local relaxation attempts?**
  Taking advantage of the understanding of GB mediated processes, it can be resolved how individual GB mediated processes are affected by local relaxation attempts. (Chap. 12)

Grain boundary creep

- **Can coble creep be simulated by MD?**
  MD simulation are limited to rather short time scales and therefore to high strain rates. This usually contradicts the observation of thermally activated processes such as GB creep. Several workarounds have been used, where a strong increase in temperature appears to be a very promising strategy. Here, several constraints regarding a suitable microstructure need to be considered. (Chap. 13)
- **How do segregating solute affect the creep compliance of NC microstructures?**
  Segregating solutes in the GB can stabilize a given microstructure against (thermally activated) curvature driven grain growth. Here, it needs to be resolved whether they also affect the creep resistance of a NC metal. (Chap. 13)
- **How can the creep resistance be affected? What are the reasons?**
  If the creep resistance is altered by the introduction of segregating solutes

into the GB, the question arises how this effect can be explained. The according material parameters need to be systematically studied and the controlling parameters need to be identified. (Chap. 13)

- **What are the atomistic mechanisms of mass transport in the GB?**
  GB creep relies on atomic mass transport through the GBs. The atomic processes, accounting for this mass transport may depend on the type and state of the GB. A generalized understanding of the contributing processes as a function of type and state of the GB would be beneficial. Furthermore, it is still widely discussed, how GBs in a NC microstructure compare to bulk amorphous material. Here, MD simulations can contribute to gain some insight and compare the two different cases. (Chap. 13)

2

METHODS

2.1 MOLECULAR DYNAMICS SIMULATIONS

Atomistic simulations provide unique insights into atomic-scale processes [114, 115]. They are a useful tool to develop an understanding of structure-property relationships [52] and have provided unprecedented insights into the structural and mechanical properties of NC materials [51].

2.1.1 *Basic principles*

MD simulations allow to study the dynamics of a given set of mass points (atoms). The interactions between the atoms are defined by interatomic potentials (Sec. 2.1.2). The force $\mathbf{F}_i$ on a given atom i at the position $\mathbf{r}_i$ due to its interacting neighbors is computed as the gradient of the scalar potential $V(\mathbf{r}_i)$

$$\mathbf{F}_i = -\boldsymbol{\nabla} V(\mathbf{r}_i), \quad i = 1...\mathrm{N}. \tag{2.1}$$

According to Newtons' equation of motion

$$\mathbf{F}_i = m_i \mathbf{a}_i, \tag{2.2}$$

the acceleration $\mathbf{a}_i$ of the atom i with the mass m_i can be computed.

To evaluate the atomic trajectories, a differential equation for the position of each atom is formulated and numerically solved. Within the framework of the LAMMPS MD code [116], which is used in this work, this is done according to the Velocity Verlet [117] algorithm. Here, for a given set of atomic positions $\mathbf{r}$ and velocities $\mathbf{v}$ at a given time t, the positions after a time increment δt are computed according to

$$\mathbf{r}(t+\delta t) = \mathbf{r}(t) + \delta t \mathbf{v}(t) + \frac{\delta t^2}{2}\mathbf{a}(t). \tag{2.3}$$

The atomic positions $\mathbf{r}(t+\delta t)$ then describe the state of the system after evolving for the time increment δt. Successive iterations, where positions, velocities and accelerations of each atom in the system are computed therefore yield the atomic

trajectories of all atoms in the system. The total simulated time equals the number of iterations multiplied with the time increment δt of each iteration.

During one iteration the atomic forces are, however, assumed to be constant. The time increment δt therefore needs to be in the range of a few femtoseconds only. The total time, accessible by MD simulations is thus typically in the range of a few nanoseconds [118].

Regarding the size of the model systems, limitations can be overcome by parallelization. Here, billions of atoms can readily be treated [119]. Compared to conventional experimental samples (which usually contain on the order of 10^{23} atoms), however, also the accessible spatial dimensions are small.

MD nevertheless allows to study atomic processes in structures with according dimensions such as nanoparticles, nanowires or NC systems. A proper selection of the boundary conditions furthermore allows to mimic bulk material [114]. Here, commonly three dimensional periodic boundary conditions are applied. In this way, identical images of the system are introduced at the boundaries, filling the space around the studied structure. This geometry avoids the occurrence of surfaces. It does, however, allow for interaction across the edges of the system bearing the risk of self interaction for the case of very small systems or long range interactions.

All MD simulations presented in this work were carried out using the freely available LAMMPS MD code [116]. The code was modified to carry out additional computations and characterizations as described below. For all simulations, periodic boundary conditions were applied in all three dimensions. The sizes of the model structures were chosen large enough to prevent self interaction of individual grains across the periodic boundaries.

2.1.2 *Interatomic potentials*

At the core of a MD simulation is the description of the interaction between the atoms in the system. In the past, several formalisms for interatomic potentials have been developed [114]. Depending on the material of interest and the properties which need to be reliably reproduced, different formalisms are required [118]. For a variety of fcc metals, embedded-atom method (EAM) potentials showed a good agreement with experimental results regarding the properties of the material while conserving a comparably low computational effort. All of the systems studied in the presented work were described by EAM type [120] potentials. For one system, a modified EAM, namely a *concentration-dependent embedded-atom method* (CD-EAM) [121, 122] potential was employed. For another alloy, an empirical manybody potential in the framework of the Finnis-Sinclair (FS) [123] model was used. The details of the interatomic potentials are given in the following.

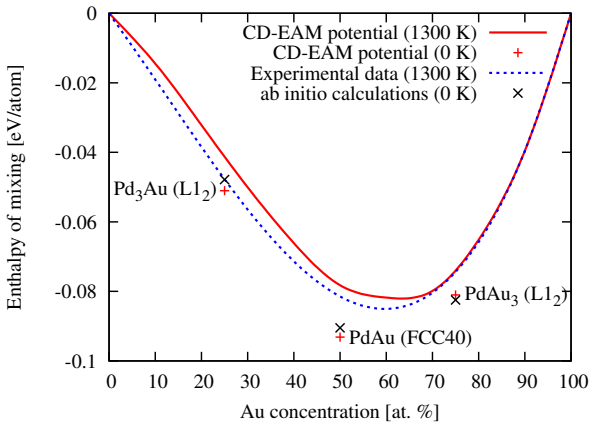

Figure 6: Enthalpy of mixing of the Pd–Au binary alloy.

PdAu

For studying the Pd–Au alloy we use a semi-empirical interatomic potential. Pure elements are described by EAM potentials for Pd [124] and Au [125]. The EAM potentials for the elements yield elastic constants and stacking fault energies that are in good agreement with experimental data. The cross interaction follows a recent formulation of the CD-EAM [121, 122] that has been developed to exactly reproduce the enthalpy of mixing of alloys over the full compositional range. The Pd–Au binary system has a negative enthalpy of mixing and is completely miscible at higher temperatures [126]. The CD-EAM formalism helps us to derive the cross potential V_{AB} from the experimental enthalpy of mixing curve in a very straightforward manner. In this formalism, the cross potential, $V_{AB}(x,r) = h(x)\Phi_{AB}(r)$, is composed of two parts: (i) the concentration-dependent function, $h(x)$, which is a forth-order polynomial of the local gold concentration, x, and (ii) the static cross potential, Φ_{AB}, which we choose to be the arithmetic mean of the elemental pair potentials: $\Phi_{AB} = (V_{AA} + V_{BB})/2$.

The EAM potentials of the pure elements were normalized to an *effective pair representation* [122] that preserves all properties of the pure elements in order to make them compatible and to minimize nonlinear contributions of the embedding terms to the formation energy. The five coefficients of the $h(x)$ polynomial were then determined such that the experimental enthalpy of mixing curve at 1300 K [126] is reproduced by the potential for a random solid solution (figure 6). Table 1 lists the coefficients of the $h(x)$ polynomial after fitting.

The potential has exclusively been fitted to the enthalpy of mixing of the disordered high-temperature phase of Pd–Au at 1300 K. Experimental data [127, 128] and *ab initio* calculations [129, 130, 131] indicate that additionally ordered phases occur at low temperatures. The formation energies of these phases, which

Table 1: Coefficients of the 4th order polynomial $h(x) = \sum_{n=0}^{4} h_n x^n$ for the Pd–Au potential. Here, x denotes the local Au concentration ($0 \leq x \leq 1$).

h_0	h_1	h_2	h_3	h_4
1.159085	−0.126781	0.481763	−0.488693	0.203778

were not part of the fitting procedure, are also properly predicted by the CD-EAM potential (Fig. 6).

FeNi

The atomic interactions for the case of Fe–Ni are described by the EAM type potential by Bonny et al. [132]. It was developed to reproduce the phase diagram of the presented system [132]. The description of the pure elements is according to the interatomic potential by Mendelev ("potential 2") [133] for the case of Fe and according to the interatomic potential by Voter and Chen [134] for the case of Ni. In coincidence with experimental findings, the potential for the Fe–Ni alloy describes the $L1_0$ FeNi and the $L1_2$ $FeNi_3$ intermetallics as the only ground states. Furthermore are the defect properties for the ferritic phase as well as for the austenitic phase in reasonable agreement with literature [132].

Cu+X

Also for the description of the various Cu alloys studied in the presented work, we used semi-empirical EAM type potentials and one potential based on the FS model.

For Cu–Nb, we employed the interatomic potential by Demkowicz and Hoagland [135]. It was constructed in part, to reproduce the large, positive heat of mixing [135]. The cross potential was fitted to the dilute enthalpies of mixing obtained from analytic fitting of the phase diagram and to the lattice constant and bulk modulus of a hypothetical Cu-Nb crystal as obtained from *ab initio* calculations [135]. The descriptions of the pure elements was shown to be in excellent agreement with *ab initio* calculations regarding energy and stability of several nonequilibrium structures for Cu [136]. The potential for pure Nb was fitted to the cohesive energy, the lattice constant, the three cubic elastic constants and the unrelaxed vacancy formation energy [137].

For Cu–Ag, we used the EAM potential by Williams et al. [138]. Here, the identical Cu potential as for Cu–Nb was used [136]. The EAM potential for Ag was shown to correctly reproduce the lattice parameter, cohesive energy, elastic constants, phonon frequencies, thermal expansion, lattice-defect energies as well as energies of alternate structures [138]. The potential for the binary Cu–Ag system was then fitted to the energies of imaginary phases from *ab initio* calculations. The resulting potential was shown to be in good agreement with

experimental observations for the whole composition and temperature range [138].

For Cu–Fe, we used the potential by Ludwig et al. [139]. Here, for the pure phases, the Cu potential by Voter [140] and the iron potential by Simonelli [141] were used. Both fit Roses' equation of state and properly reproduce other element properties including lattice constant, cohesive energy, elastic constants and vacancy formation energy [139]. The potential for the alloy was then constructed to reproduce physical parameters of the alloy, such as the heat of solution of Cu in Fe and the binding energy of a vacancy and a Cu atom in the α-Fe matrix [139].

The Cu–Zr alloys of varying composition are described by the FS type potential by Mendelev et al. [142]. It reproduces the amorphous alloy structure in agreement with x-ray diffraction data and can be used to model the properties of Cu–Zr alloys [142]. Here, the potentials for the pure phases were developed to reproduce several *ab initio* configurations and high-temperature phase transitions for the case of Zr [143] and to yield better agreement with the first-principle and measured liquid diffraction data for the case of Cu [144].

2.2 MONTE-CARLO SIMULATIONS

2.2.1 *The semi-grandcanonical ensemble*

Monte-Carlo (MC) simulations sampling the semi-grandcanonical (SGC) ensemble allow to equilibrate the composition and distribution of the constituents of the system for a specified chemical potential difference $\Delta\mu$.

The probability distribution function for the SGC ensemble is

$$\pi_{\mathrm{SGC}} = \mathcal{Z}_{\mathrm{SGC}}^{-1} \exp[-\beta(E + \Delta\mu c)], \tag{2.4}$$

where $\mathcal{Z}_{\mathrm{SGC}}$ is the partition function of the SGC ensemble, $\beta = \frac{1}{k_B T}$, where k_B is the Boltzmann constant and T is the temperature, E is the internal energy and c is the concentration.

For the present purpose, it is convenient to introduce the parameter $\mu = \beta\Delta\mu$ and rewrite equation 2.4 as

$$\pi_{\mathrm{SGC}} = \mathcal{Z}_{\mathrm{SGC}}^{-1} \exp[\beta E - \mu c]. \tag{2.5}$$

The SGC ensemble can be sampled using a simple transmutational MC algorithm (Metropolis algorithm, Fig. 7): (1.) one atom is picked at random, (2.) the chemical identity is changed e.g., from A to B or B to A, (3.) the energy change is computed according to $\Delta E = E_{\mathrm{new}} - E_{\mathrm{old}}$, (4.) the exchange is accept or reject according to the transition matrix

$$K_{\mathrm{SGC}} = \min\{1, \exp[-\beta\Delta E - \mu\Delta c]\} \tag{2.6}$$

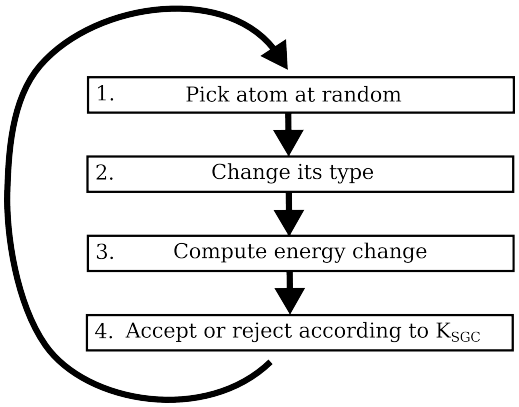

Figure 7: Metropolis algorithm of the SGC ensemble

where $\Delta c = c_{\text{new}} - c_{\text{old}}$ is the concentration change associated with the trial move. The algorithm then returns to the initial step, carrying out the same trial exchange on another randomly picked atom.

The SGC ensemble is well suited for massive parallelization. The details of the spatial decomposition and handling of the system boundaries are described in Ref. [145].

2.2.2 *The variance-constrained semi-grandcanonical ensemble*

For single phase systems, one can readily employ the SGC ensemble, as described above, where the composition is determined by the difference in chemical potential $\Delta\mu$. The SGC is in principle, however, limited to one-phase regions, since it cannot deal with situations where the relation between the concentration c and the chemical potential difference $\Delta\mu$ has an infinite slope, such as in two-phase regions of the phase diagram [146]. Here, an additional constraint needs to be introduced, in order to keep the global composition at the desired value [146]. This can be realized by controlling the reservoir of the ensemble via additional parameters [145]. The probability distribution function of the variance-constrained semi-grandcanonical (VCSGC) ensemble thus is

$$\pi_{\text{VCSGC}} = \mathcal{Z}_{\text{VCSGC}}^{-1} \exp[-\beta(E) - \beta c(\phi + \kappa c)], \tag{2.7}$$

where $\mathcal{Z}_{\text{VCSGC}}$ is the partition function of the VCSGC ensemble and the two independent variables ϕ and κ are Lagrange multipliers associated with the constraints on the first and second moment of the concentration [145].

The transition matrix for the accepting or rejection of trial exchanges then reads

$$K_{\text{VCSGC}} = \min\left\{1, \exp[-\beta(\Delta E + \Delta c(\phi + 2\kappa\tilde{c}))]\right\}, \tag{2.8}$$

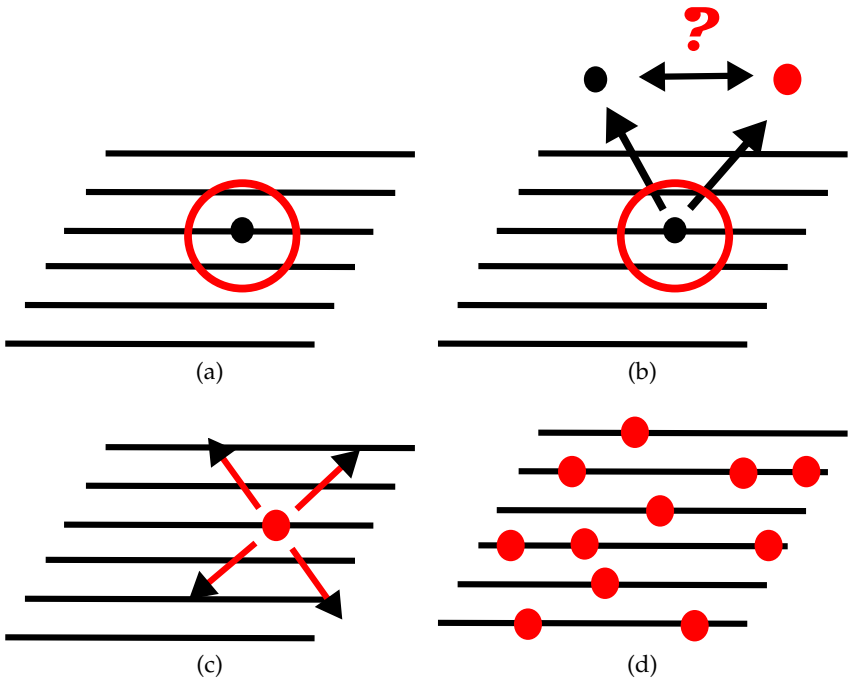

Figure 8: Hybrid MD/MC scheme: a) Atoms are picked at random, b) their chemical identity is changed and the resulting difference in energy is computed. The trial exchange is rejected or accepted according to a transition matrix K_{SGC} (see text). c) MD is employed, to structurally relax the new configuration. d) In this way, the crystal lattice is decorated with solutes, where the solute atoms are introduced at energetically favorable positions, while relaxations and thermal vibrations are taken into account.

where $\tilde{c}$ refers to the average concentration between two successive trial moves. The ensemble can be categorized as an extended Gaussian ensemble, being in contact with a finite reservoir. It allows for the simulation of compositions in a two-phase region of the according phase diagram [145].

For some cases (Chap. 12), the variance control is employed in the presented work to restrict the global composition to a desired value during MC simulations.

2.3 HYBRID MOLECULAR DYNAMICS / MONTE-CARLO SCHEME

In the previous section we introduced the parallel SGC-MC algorithm, which allows to study systems with millions of particles. In many applications, however, the configuration space includes continuous (off-lattice) particle positions which allow for structural relaxations and thermal vibrations. This local structural relaxations can be crucial to properly describe a given system [147, 148].

Therefore the transmutational MC scheme has to be combined with an algorithm that captures the structural as well as the vibrational degrees of freedom.

This can be achieved by a combination of the transmutation MC moves with MD simulations (Fig. 8): After MC trial exchanges are carried out the system, a certain number of MD steps allows for structural and vibrational relaxation, before returning to the MC part. The number of MD steps between series of MC moves as well as the number of MC trial exchanges during one MC series can be adjusted to optimize the convergence of the simulation. In this way, a given crystal lattice or off-lattice configurations such as GBs can be decorated with solute atoms in accordance with the thermodynamic driving forces, where structural and vibrational degrees of freedom are taken into account.

This algorithm was implemented [145, 149] into the freely available LAMMPS MD code [116]. In case of an accepted type swap, the velocity of an atom is rescaled to conserve its kinetic energy. Both, the MD and MC parts of the simulation code are parallelized to enable large-scale simulations of NC alloy structures.

2.3.1 *Simulation procedure*

For modeling the equilibrium properties of NC alloys, we utilize the hybrid simulation method as described above. In that way, we account for structural relaxations and thermal vibrations as well as the exchange of atom types.

This hybrid simulation procedure is employed, to carry out the annealing and alloying for some of the microstructures (Chap. 3). For the initial relaxation and for the most cases of mechanical testing (Chap. 2.5) conventional MD simulations are conducted. Here, the MC algorithm is not employed, but the simulation procedure (Fig. 9) is otherwise identical.

Fig. 9 visualizes the workflow of a typical simulation. Crucial for the quality of the simulations and the according results is a suitable input structure and proper selection of the simulation parameters. Subsequent to the (hybrid) simulations, the thermodynamic output as well as the evolution of the microstructure needs to be analyzed. The characterization techniques are used to analyze the initial alloyed microstructures (Chap. 4) as well as the microstructures during straining (Chap. 6-Chap. 13). A short description of the techniques is given below.

2.4 CHARACTERIZATION

The result of the simulations consists of thermodynamic parameters and atomic configurations (Fig. 9). While the thermodynamic output contains readily interpretable system averages which represent the macroscopic behavior, the atomic configurations need further characterization. Here, the information of the atomic evolution is contained in a dataset of coordinates representing the centers of

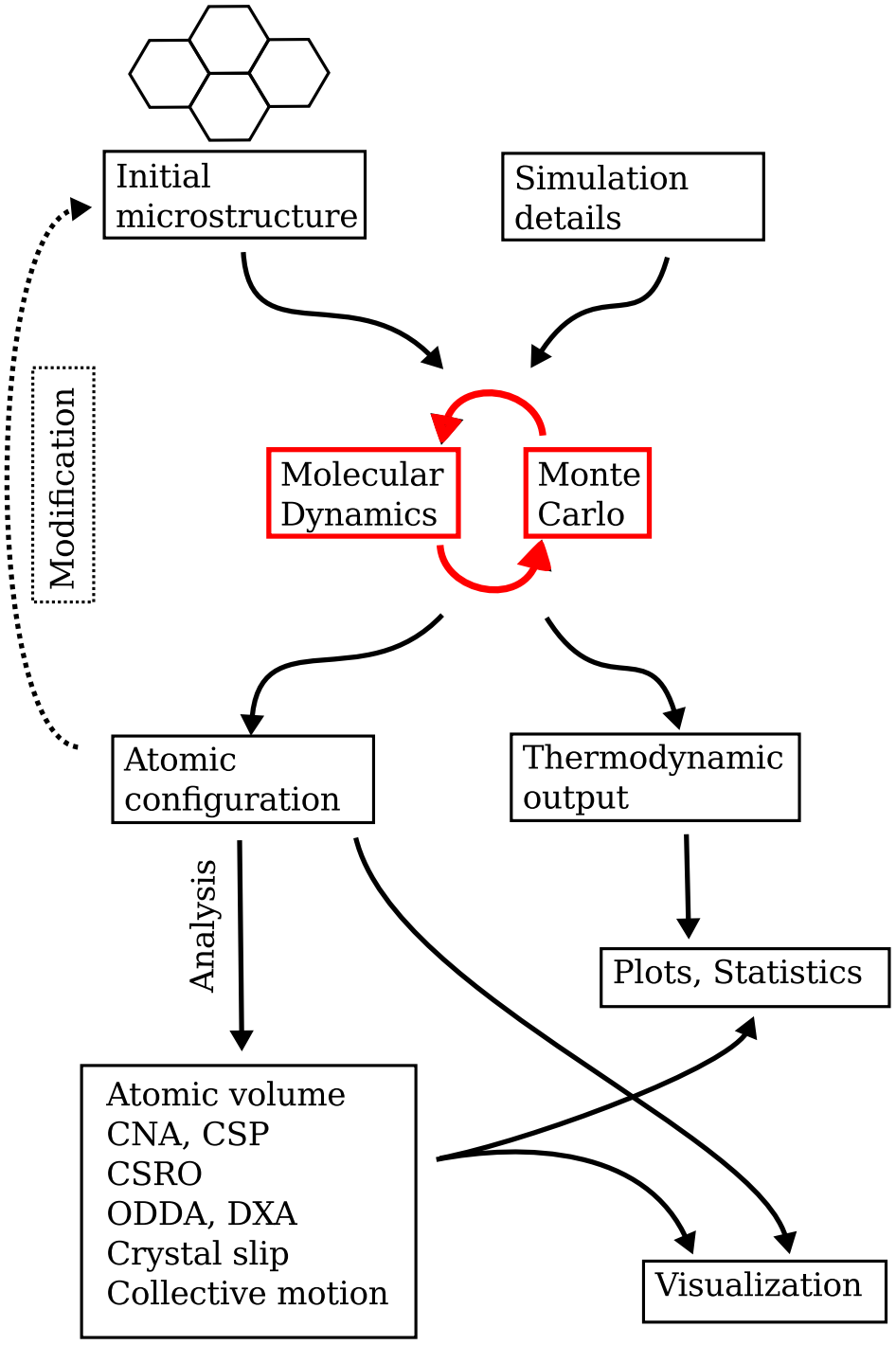

Figure 9: Workflow of typical hybrid MD/MC simulation. The algorithms and methods are described in the text.

mass of the atoms. Information about changes in the atomic configuration, about the nucleation and evolution of defects of multiple dimensionality needs to be extracted from snapshot of atomic positions. Several methods which are used throughout the presented work to extract this information from the temporal evolution of atomic positions are introduced below.

2.4.1 *Atomic Volume*

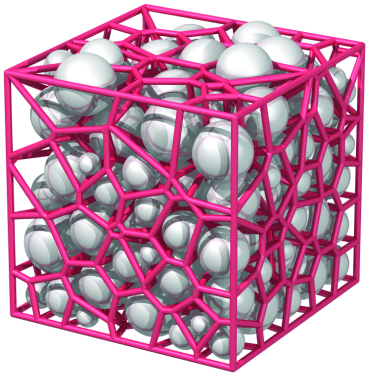

Figure 10: Radical Voronoi tessellation for a polydispersed packing of 159 particles in a cube. (Reprint from Chaos **19**, 041111 (2009), © 2009, with permission from the American Institute of Physics.)

The atomic volume, or the excess volume of an atom (as compared to the atomic volume in the ground state lattice) can be used to quantify the character of a GB. In fact, the free volume is considered to be the best single criterion for characterization of GBs [150]. We use the Voronoi tessellation method [151], to compute the local atomic volume of each atom. The Voronoi tessellation divides the simulation cell into Voronoi polyhedrons (VPs). Around each atom, the lines joining an atom and its neighbors are bisected at a right angle by interface planes. The set of planes enclosing a given atom are its VP and define the atomic volume and neighborhood as shown in Fig. 10.

The excess volume per atom is then the difference between the calculated volume for an atom in a given structure and the average volume of an atom of the same type within a single crystal of identical global composition at identical conditions. If the analysis is carried out for an alloy, a single crystal of a random solid solution with an identical composition serves as a reference. We define the free volume of the GB atoms as the sum over the excess volumes of all atoms belonging to the GB according to structural criteria such as common neighbor analysis or centrosymmetry-parameter (see below).

2.4.2 *Structural short range order*

For distinguishing atoms located in GBs from atoms located in the grains, we use structural short range order (SRO) parameters such as the common neighbor analysis (CNA) [152] or the the centrosymmetry parameter (CSP) [153].

Common Neighbor Analysis

The CNA is a decomposition of the radial distribution function according to the local environment and allows for a systematic analysis of the local atomic structure [154, 152]. It is a useful measure for the structure around an atom and mostly used in mono-component solid-state systems. Also for an alloy, the CNA can serve as an analysis tool as long as the lattice structure of the alloy is known and not strongly distorted. For the case of multiple phases with different lattice constant, the CNA can only analyze one phase at once.

For a given cutoff parameter, the CNA analyses the neighborhood of an atom with respect to the position of the neighbors. If the pattern of the neighboring atoms matches a known crystal lattice, the configuration is recognized and the atom is labeled as belonging to this crystal lattice. If the pattern does not match a known crystal lattice, the atom is considered to belong to a strongly distorted region such as GBs or dislocation cores.

The cutoff parameter R_{CNA} for identifying nearest neighbors (NNs) was set between the first and second NN shells in the fcc lattice according to:

$$R_{\mathrm{CNA}} = a_0(c,T) \cdot (1+\sqrt{1/2})/2, \tag{2.9}$$

with $a_0(c,T)$ being the average lattice parameter for a given concentration c and temperature T.

Centrosymmetry Parameter

The CSP can also be employed as a measure of the local lattice distortion around a given atom [153]. It is calculated according to

$$CSP = \sum_{i=1}^{N/2} |\boldsymbol{R_i} + \boldsymbol{R_{i+N/2}}|^2, \tag{2.10}$$

where the N nearest neighbors are identified and $\boldsymbol{R_i}$ and $\boldsymbol{R_{i+N/2}}$ are vectors from the central atom to a particular pair of neighbors. From the $N*(N-1)/2$ possible neighbor pairs, the $N/2$ smallest are used. Those are typically pairs of atoms in symmetrically opposite position (with respect to the central atom). N is an input parameter which is typically the number of nearest neighbors for the underlying crystal lattice. For a fcc crystal lattice, N equals 12.

While the CNA strictly categorizes the atoms in the system according to the local lattice topology (or to an unknown structure), the CSP quantifies the deviation from a perfectly symmetric coordination. Both can be used in a similar manner to identify atoms which belong to a distinct group of atoms e.g. the GBs [155]. Locally, the results from either method may, however, deviate.

2.4.3 *Chemical short range order*

For a given alloy not only the structural order by means of defects, but also the chemical order can drastically influence the macroscopic behavior. The elemental distribution around a given atom is quantified by evaluating the chemical short range order (CSRO). Here, we compute an ordering parameter for each atom surrounded by its N nearest neighbors in accordance with the ordering parameter by Warren and Cowley [156] as

$$\alpha_i = 1 - \frac{Z_j}{N \times (1 - c_i)}, \tag{2.11}$$

where α_i denotes the ordering parameter for atom of type i, Z_j is the number of atoms of the according other type among the N nearest neighbors and c_i is the global concentration of atoms of type i. In a fcc lattice, each atom has 12 nearest neighbors. We implemented this chemical analysis into the freely available LAMMPS MD code.

2.4.4 *Extended defects*

Methods such as CNA and CSP (as introduced above) are well suited, to identify atoms belonging to structural defects like vacancies, dislocations, planar faults or GBs. In most cases, they can, however, neither distinguish between the different defects nor extract characteristic higher-level information such as the Burgers vector of a dislocation. Here, more sophisticated analysis algorithms need to be employed, in order to extract the according information from atomistic data. Two algorithms for extracting dislocations (and other defects) from atomistic simulations were used in the present work, which are briefly introduced below. For a full description of the analysis procedure and the according capabilities, the reader is referred to the original publications [157, 158].

ODDA

The on-the-fly dislocation detection algorithm (ODDA) [157] is derived from the original definition of dislocations and conducts a local Burgurs circuit search around defected atoms. This allows to locate dislocation cores and to determine their Burgers vector. This information can then be used for constructing a discrete dislocation representation. After the dislocation network is extracted from the atomistic data, it can be further analyzed with respect to dislocation reactions, types of dislocations and dislocation densities. The algorithm is readily implemented in existing MD code and can be used to efficiently analyze also large-scale atomistic simulations [157].

DXA

The dislocation extraction algorithm (DXA) [158] also extracts information about defects from atomistic data. In contrast to ODDA, it directly translates a given network of distorted atoms into a network of connected dislocation segments, preserving the true topology. In that way, it generates the geometric description of dislocation lines and nodes while it outputs the remaining crystal defects as triangulated surfaces. Similar to ODDA, the extracted dislocation network can then be analyzed with respect to detailed dislocation processes such as nucleation or interaction or with respect to dislocation types and the respective densities [158].

2.4.5 *Decomposing crystal slip*

The algorithms described above allow to extract information about the type and density of dislocations as well as other defects within the microstructure at a given time for an individual snapshot. They do, however, not reveal the respective contributions of the individual defects to the overall deformation. At this point, an algorithm was used, which decomposes the deformation field into elastic and plastic parts for the case of crystalline materials. It allows to quantify the plastic deformation in a crystalline material due to dislocation movement [159].

The algorithm was used to extract the contribution of dislocation motion to the overall deformation for deformed microstructures. For a full description of the decomposition details and the capabilities of the algorithm, the reader is referred to Ref. [159].

2.4.6 *Collective atomic motion*

For an atom, which is part of a given crystal lattice, the nature of potential displacements is well defined by the lattice itself where (e.g. during dislocation motion) several atoms can move in a collective manner for a well defined amount in a well defined direction.

For the case of an off-lattice configuration such as a GB or a bulk amorphous material, the situation is somewhat different. Here, neither the amount, nor the direction of the movement can be estimated from geometrical considerations. Furthermore is the interaction between a collection of particles more complex than for the case of a crystalline structure.

Thus we implemented the following algorithm into a standalone analysis tool to examine the atomic motion within off-lattice configurations such as GBs. First, all atoms (independent of their type) moving more than half the NN distance within a given time window were identified as a function of time. The nature of movement of those atoms was then analyzed, following an approach by Donati

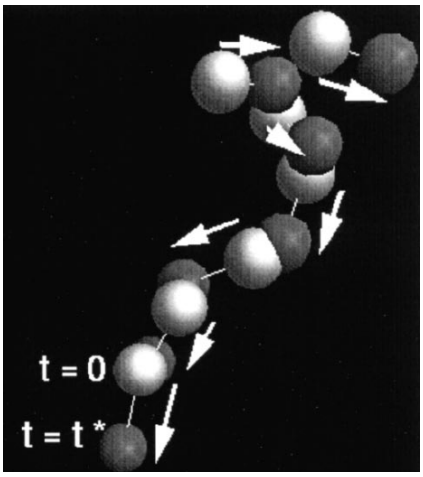

Figure 11: Stringlike collective motion: Particles at t=0 are shown in white, same particles at later time are shown in dark grey. (Reprint from Physical Review Letters **80**, 2338 (1998), © 1998, with permission from the American Physical Society.)

et al. [160] (Fig. 11), where atomic motion is considered stringlike or collective if the former position of a moving particle is occupied by another mobile particle. Otherwise the motion was considered independent.

This allows to extract the amount of collectively (stringlike) moving particles from snapshots of atomistic simulations. The nature of displacement inside the GBs can thus be characterized for different external conditions.

2.5 SIMULATION OF MECHANICAL TESTING

Mechanical testing was simulated at constant temperature by imposing a constant engineering strain rate in uniaxial direction on the simulation cell. If the deformation temperature deviated from the annealing temperature, the samples were quenched to the desired temperature, before uniaxial testing was conducted.

As shown in Fig. 12, the samples are elongated or compressed along the z-direction. For all cases, periodic boundary conditions were applied in all directions. The lateral dimensions were adjusted using a Berendsen barostat [162]. This controls the lateral box length by homogeneously rescaling all atom coordinates such that the components σ_{xx} and σ_{yy} of the stress tensor are zero. The temperature during straining is controlled using a Berendsen thermostat [162]. The resulting simulation setup corresponds to a mixed ensemble consisting of a constant volume–constant temperature (*nvt*) ensemble in the loading direction, and a constant pressure–constant temperature (*npt*) ensemble in the lateral directions.

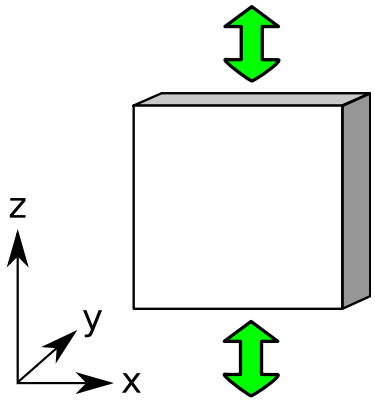

Figure 12: Simulation of uniaxial mechanical testing: Samples are deformed in z-direction. The lateral boundaries (x and y) are periodic. During straining, pressure control allows for lateral relaxation.

For most of the cases an engineering strain rate of 10^8 1/s was applied. Lower or higher rates (10^7 1/s or 10^9 1/s, respectively) were used to test the strain rate dependence of our results and/or to speed up the simulations.

For the simulations of thermal creep (Sec. 13), the uniaxial testing was carried out at constant load. Here, the barostat was used, to adjust the components of the stress tensor in all three dimensions (σ_{xx}, σ_{yy} and σ_{zz}). In this case, the simulation setup corresponds to a constant pressure–constant temperature (*npt*) ensemble. In the lateral dimensions (x- and y-direction), the pressure was also controlled to be zero, while the pressure in z-direction had a finite value (on the order of 500 MPa).

Part II

SIMULATION OF NANOCRYSTALLINE ALLOYS

The following part is devoted to the preparation and characterization of samples for atomistic simulations. After describing the different routes of solute introduction, the obtained samples are characterized in terms of elemental distribution where the main emphasis lies on the regions in the vicinity of the GBs. Additionally, selected material properties, which change as a function of composition are discussed.

3

PREPARATION OF MODEL STRUCTURES

3.1 PREPARATION OF NANOCRYSTALLINE MODEL STRUCTURES

For modeling the properties of NC alloys, we utilize classical MD simulations or the hybrid MD/MC scheme (Sec. 2.3). In contrast to most experimental attempts, where composition and grain size are varied at the same time, we can produce samples of differing composition for a given average grain size. In general, we first created NC model structures of the pure host metal. In all cases, the Voronoi tessellation method [161] was used to set up the grain shapes based on randomly placed center points in a cubic simulation box. Similar to the extraction of an atomic volume, where the volume of the sample is distributed over all atoms (see Sec. 2.4.1), the Voronoi tesselation allows to divide the volume of the simulation box into different VPs i.e. grains. Here, for a given set of grain center points, the surrounding space is divided such, that an arbitrary point in space belongs to the closest center point. The space belonging to each center point is then filled with atom positions located on the according crystal lattice, where the lattice orientations of the grains are taken from a random isotropic distribution. Three-dimensional periodic boundary conditions are applied in all three dimensions to model a bulk structure. We deleted atoms from the grain boundaries that were closer than 2.0 Å to other atoms prior to initial relaxation, to avoid spurious configurations in the as-prepared Voronoi samples (Fig. 13).

Initial relaxation was then done at 300 K to minimize the enthalpy, where the system was also relaxed to zero pressure. Berendsen's [162] thermostat and barostat were used for conrolling temperature and pressure. After initial relaxation, annealing and alloying was carried out. This was done at zero pressure and at moderate temperatures (in the range of 500 - 600 K, see below). Regarding the alloying two distinct ways were compared (Fig. 13): In one case, the solute atoms were introduced by randomly replacing host atoms in the microstructure or in a specific region of the microstructure (such as the GB). In the other case, the solute atoms were introduced into the microstructure using the hybrid MD/SGC-MC algorithm, which locates the solutes at energetically and entropically favorable positions by carrying out the trial exchanges as described in Sec. 2.3.1. The latter

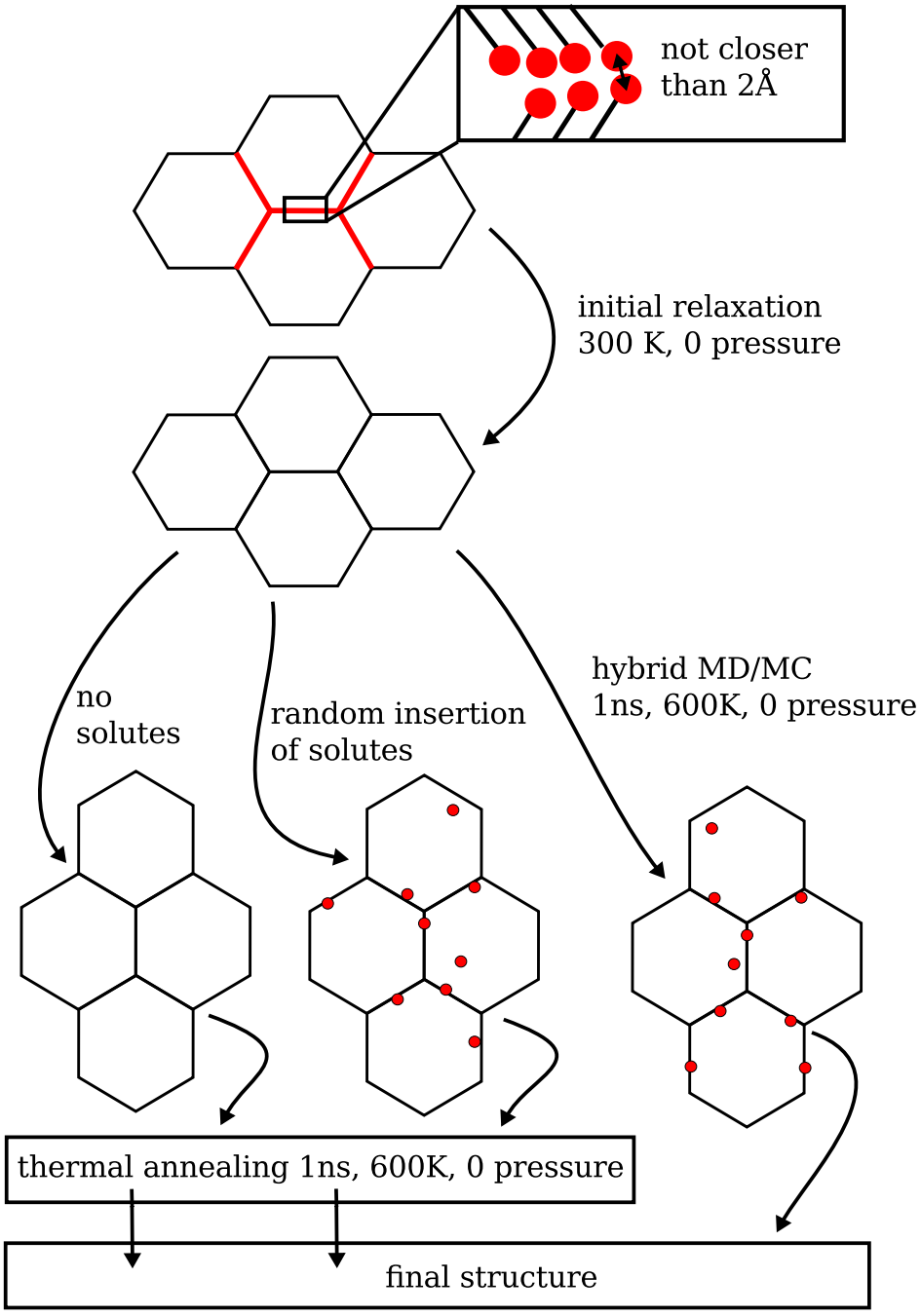

Figure 13: Alloying and equilibration of NC structures: Spurious configurations in the GBs are excluded by deleting atoms, which are located too close to each other. Solutes are introduced either randomly or using the hybrid MD/MC scheme. Equilibration is done for 1 ns at elevated temperature.

not only allows to equilibrate the given distribution of the constituents but also the composition of the system for a chemical potential difference $\Delta\mu$.

For both cases, annealing and alloying was carried out at the identical temperature. If MC was employed, the temperature parameter for the Metropolis MC algorithm was also set to the annealing temperature.

3.1.1 *PdAu*

We created NC model structures with average grain sizes of 5, 10 and 15 nm consisting of 432, 128 and 54 grains, respectively. After initial relaxation at 300 K, annealing and alloying was performed at 600 K for 1 ns at zero hydrostatic pressure using Berendsen's [162] thermostat and barostat. For the alloying, both methods of solute insertion were used. While the random distribution of solutes over the whole microstructure by random atomic exchanges serves as a reference structure, the hybrid MD/MC algorithm was employed to construct fully equilibrated samples, where the solutes are distributed according to the thermodynamic driving forces. Here, the temperature parameter for the Metropolis MC algorithm was also set to 600 K as in the MD stage. One full MC step was performed every 40 fs, i.e., 25,000 trial exchanges were performed on each atom in the system. At this temperature, some ordering effects in the Pd–Au solid solution have been described by several authors [129, 130, 131]. Indeed, we observe differences between MC equilibrated single crystals and random solid solutions in the SRO, which also affect the elastic properties as shown in Sec. 6.

3.1.2 *FeNi*

To model NC Fe–Ni, the atomic interactions were described by the EAM type potential introduced above (Sec. 2.1.2). Initially, we created NC model structures of perfectly ($L1_2$) ordered $FeNi_3$ with average grain sizes of 5 and 15 nm consisting of 432 and 54 grains, respectively. After initial relaxation at 300 K, annealing and equilibration of the composition and distribution of the constituents was then performed with the hybrid MD/MC algorithm at 600 K, for 1 ns at zero hydrostatic pressure. During this MD equilibration, one full MC step was performed every 40 fs, i.e., 25,000 trial exchanges were performed on each atom in the system on average. The temperature parameter for the MC algorithm was the same as in the MD stage, to obtain the equilibrium chemical distribution for a given composition. For the variation of the global composition, we choose differing $\Delta\mu$ to chemically equilibrate the system at concentrations deviating from the stoichiometric composition.

3.1.3 *Cu+X*

For the case of dilute NC Cu alloys, the description of the atomic interactions is given by the EAM and FS type potentials as described in Sec. 2.1.2. Here, we created a NC model of pure Cu consisting of 38 grains with an average grain size of 8 nm. The center points of grains, and the grain orientations were also randomly selected. Initial relaxation of the structure was carried out at 300 K and zero hydrostatic pressure. Afterwards annealing and alloying were performed at 500 K over a period of 1 ns also at zero hydrostatic pressure with the hybrid MD/MC scheme. During this MD run, an MC trial exchange was carried out on average on each atom every 200 fs, i.e., 5,000 trial exchanges were performed on average on each atom in the system. The temperature for the Metropolis MC algorithm was the same as for the MD part. Without additional constraints, the SGC MC cannot treat two-phase regions in the phase diagram (Sec. 2.2). We nevertheless started from pure Cu and adjusted $\Delta\mu$ such that a desired overall composition was obtained during alloying. The values of $\Delta\mu$ were not necessarily restricted to the single phase region of the equilibrium phase diagram. Precipitation of a second phase, however, which requires to overcome a nucleation barrier, was not observed. The reported concentrations, therefore, may correspond to oversaturated solid solutions, exceeding the solubility in Cu. For comparison we created samples where the solute atoms were randomly inserted prior to annealing (by regular MD), which serve as a reference during high temperature deformation (Sec. 13). Here, however, solutes were introduced exlusively in the GBs through random atomic exchanges of atoms which were identified to belong to the GBs according to CSP.

4

ELEMENTAL DISTRIBUTION

In a first characterization step, the elemental distribution in the prepared model structures (Sec. 3) annealed and alloyed by the hybrid MD/MC scheme were analyzed in order to quantify the local compositions.

The hybrid MD/MC scheme (Sec. 2.3) distributes solute atoms according to the thermodynamic driving forces, where vibrational and structural degrees of freedom are taken into account. The algorithm therefore distributes the solutes also at off-lattice sites such as GBs (Fig. 14). Here, the composition, obtained for a given $\Delta\mu$ may differ from the composition inside the grains or inside a singlecrystal. We therefore quantified the local compositions for distinct structural features such as GBs and grains.

At finite temperature, the instantaneous element distribution is fluctuating and therefore analyzing a single snapshot is not suitable for characterizing the site occupancy. Here, it is useful to introduce the concept of an "effective atom" [163], which describes the average occupancy of an atomic position. We have therefore calculated the site occupancy in the semi-grandcanonical ensemble by taking the ensemble average over a large number of MC steps. The time-averaged position and occupancy of each site is expected to converge to a constant value [164].

4.1 MISCIBLE SYSTEMS

4.1.1 *Solute distribution in PdAu*

Fig. 15 shows the local site occupancy variations for NC Pd–Au within the microstructure of a sample with 15 nm average grain size. Each picture is showing another global Au concentration. The gradient color scale has been chosen such that a green color always corresponds to the global concentration, whereas blue denotes a gold depletion of -10%, and red an enrichment of +10%. In the GBs, regions can be found where either Pd or Au is preferred. In addition, the magnitude of the variations (not shown) depends on the global concentration. The thickness of this "deviation zone" changes with the global concentration as well. Note that the slice shown here is representative for the whole polycrystalline

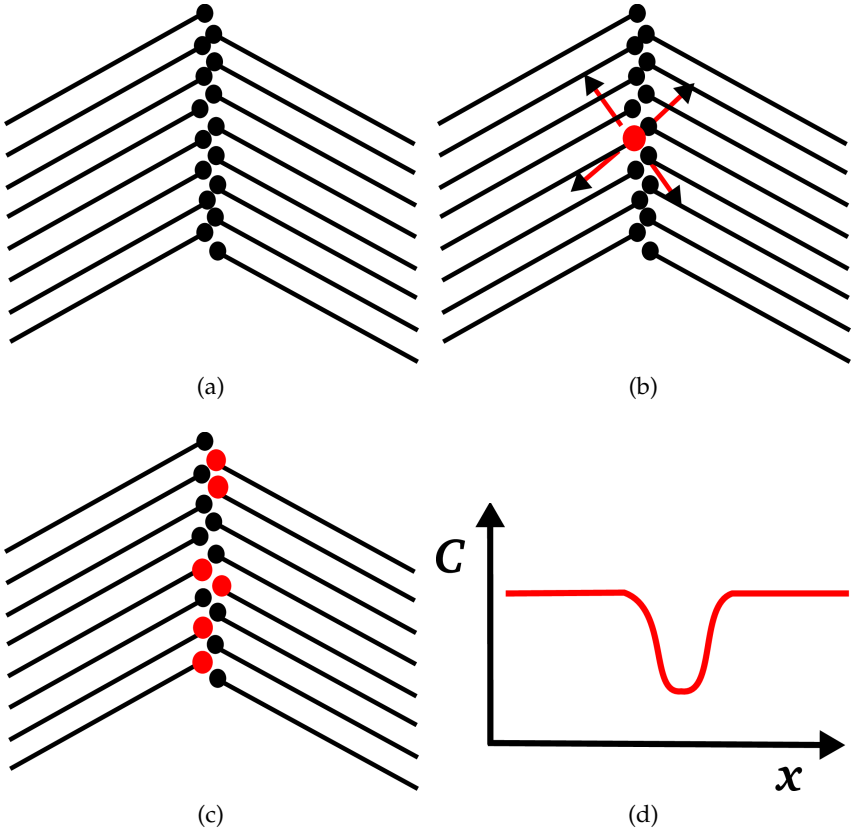

Figure 14: Hybrid MD/MC scheme in the vicinity of the GBs: a) From the atoms in the vicinity of the GB, b) one is picked at random and the chemical identity is changed in accordance with the transition matrix (Sec. 2.3), where MD is employed, to structurally relax the new configuration. c) In this way, also the GB is decorated with solute atoms, introduced at energetically favorable positions. d) The local composition in the GB may deviate from the composition in the grain interior due to segregation or as the case may be depletion effects.

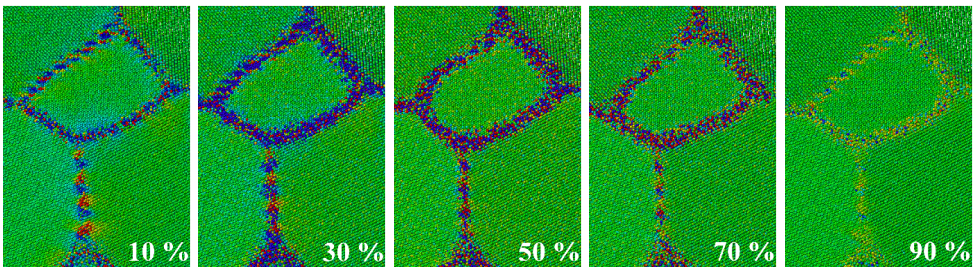

Figure 15: Cross-sections of a grain and its surrounding GBs and triple junctions in NC Pd–Au for various global Au concentrations ranging from 10% to 90%. The gradient color scale indicates deviations of local concentration from global concentration (green). Blue denotes Au depletion of 10%, red denotes Au enrichment of 10%. In this context, the concentration is defined as the average occupancy of a lattice site with an Au atom in the statistical semi-grandcanonical ensemble. (Snapshots were generated using OVITO [165])

structure, pretty much independent of the GB orientation, and we obtained comparable results for various planar symmetric GBs in bicrystal geometry.

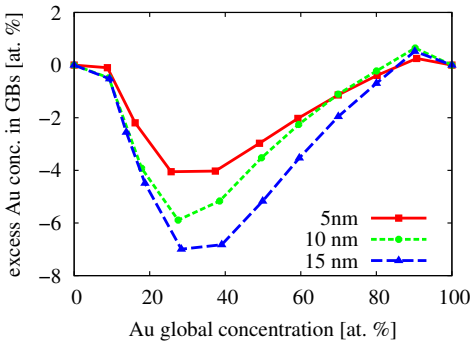

Figure 16: Average GB excess concentration in NC Pd–Au as a function of global concentration and grain size.

The GB concentration was determined by averaging the site occupancy of all disordered atoms according to the CNA. For most compositions, the GBs contain less gold than the bulk (Fig. 16). This finding is superimposed by the aforementioned variation in thickness of the "depletion zone", which depends on the global solute concentration and does not coincide with the thickness of the GB.

GB enrichment in NC metals was studied computationally and experimentally also in segregating systems [87], but GB depletion in NC miscible systems has, to our knowledge, not been reported before.

As can be seen in Fig. 16, the strength of the GB depletion effect depends on grain size. This can be explained with the GB area to bulk ratio, which is smaller for large grain sizes. Therefore, a small excess concentration in the bulk is sufficient to balance a large depletion in the grain boundaries. Moreover, this observation is in agreement with the expectation that in the case of a very small

grain size, i.e. in the amorphous limit, the material is a homogeneous phase again and all local deviations from the global composition must vanish.

4.2 ORDERING SYSTEMS

4.2.1 *Solute distribution in NiFe*

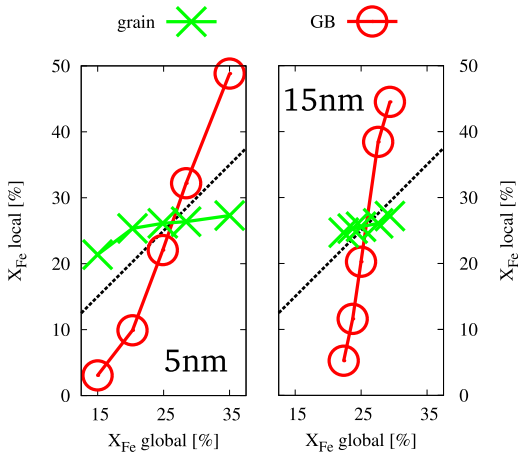

Figure 17: Local composition of the grain interior and the GBs in NC Ni–Fe as a function of the global composition for two different grain sizes.

Fig. 17 shows the local composition in NC Ni–Fe according to the local site occupancy for the different structural elements (grains and GBs), which were identified by the CNA. It can be seen that the GB composition shows a strong dependency on the global composition whereas the grain interior is less affected and stays close to the stoichiometric composition of the $L1_2$ structure (25 % of Fe). The GB therefore acts as a "buffer", accommodating any excess of Fe or Ni, respectively. This allows the grain interior to stay in the ordered and stoichiometric state. Furthermore, it can be seen, that the change in GB composition shows a stronger dependency on the global composition for a 15 nm average grain size. This can be explained with the smaller volume fraction of GB atoms as compared to the 5 nm case, which need to accommodate the excess in either Ni or Fe. For the atomic arrangement inside the grains we find $L1_2$ ordering, irrespective of global composition. It shall be noted that this finding is independent of the initial configuration prior to equilibration and alloying (Sec. 3), i.e. whether we start from a perfectly ordered or a disordered state (not shown). Fig. 18 shows representative slices through individual grains and the surrounding GBs for different grain sizes and composition. In the inset, the slice is colored according to the deviation from perfect $L1_2$ CSRO (Sec. 2.4.3), where green refers to a perfect $L1_2$ structure. For all atoms in the grain interior perfect $L1_2$ CSRO (and consequently also long range order) is conserved for both studied grain sizes. Furthermore, it is visualized (for the 5 nm case), that also for a deviation from stoichiometric composition, the grain interior stays ordered while the GB accommodates the excess in either Ni or Fe. Interestingly, for the maximum deviation from stoichiometric composition, the GB is either almost free of Fe or enriched up to 50 %, respectively (Fig. 17).

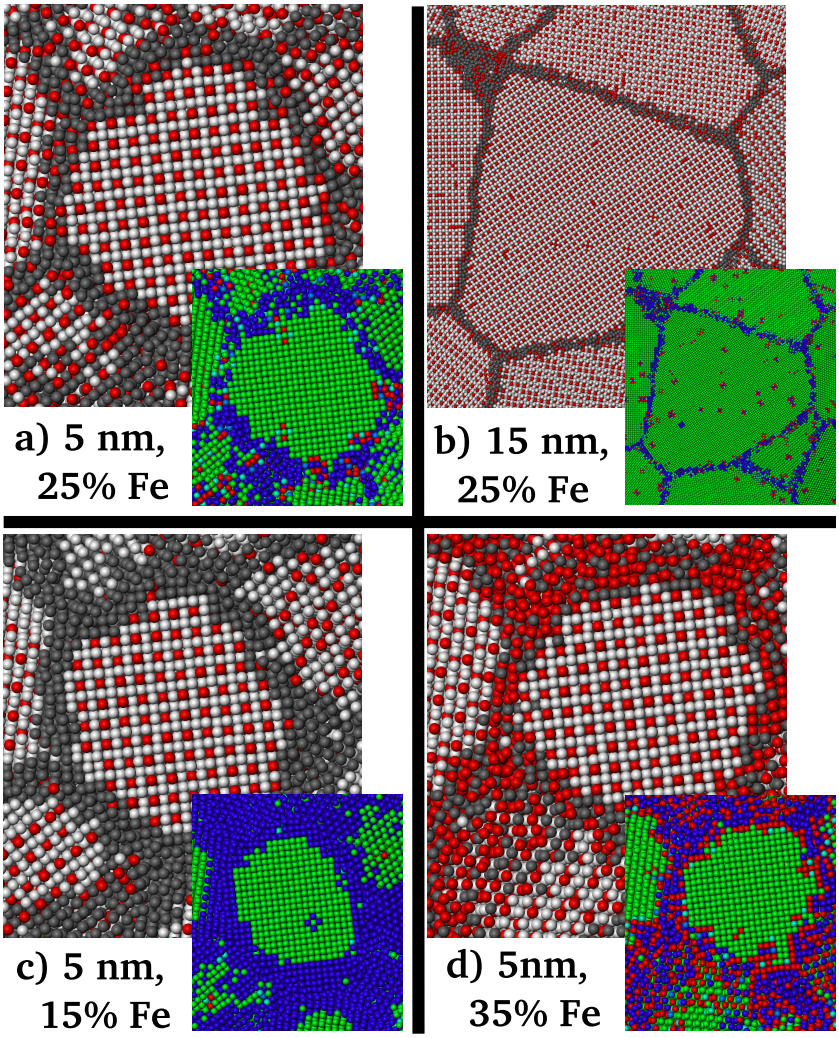

Figure 18: NC Ni–Fe: Atomic configurations after annealing with the hybrid MD/MC scheme. Ni atoms in the grain interior are white, Ni atoms in the GB are dark grey, Fe atoms are red. In the inset, the color coding is according to the deviation from perfect $L1_2$ CSRO, where green refers to perfect $L1_2$ structure, while red and blue refer to a positive and negative deviation, respectively. a) 5nm grain size with a global concentration of 25 % Fe. b) 15 nm grain size with a global concentration of 25 % Fe. c) 5 nm grain size with an (understoichiometric) global concentration of 15 % Fe. d) 5 nm grain size with an (overstoichiometric) global concentration of 35 % Fe. Snapshots were generated using OVITO [165].

The experimentally observed disordered state of NC Ni–Fe with an Fe content of up to 28 % [166] produced by electrodeposition is therefore considered to result from the route of processing, leading to a kinetically trapped disordered elemental distribution and not due to a differing stable configuration for the case of a nanometer grain size as observed for other systems [167]. On the contrary, the stability range of the ordered $L1_2$ structure in the phase diagram is even widened by a reduction in grain size, where the grains stay ordered and the GBs act as a buffer layer. It shall be noted that some of the compositions reported here, which show an ordered $L1_2$ structure inside the grains, lie outside the phase field of the $L1_2$ structure (at 600 K) in the phase diagram reproduced by the interatomic potential [132].

4.3 SEGREGATING SYSTEMS

4.3.1 *Solute distribution in CuNb*

After relaxation and the introduction of segregating solutes into the microstructure, also the model structures for the dilute Cu alloys were analyzed with respect to the solute distribution and local compositions. Atoms located in grain boundaries were distinguished from bulk atoms according to CSP. The inset of Fig. 21 shows a slice through a part of the computational cell for the case of NC Cu–Nb. It highlights a representative grain and its grain boundaries after equilibration and alloying of the system with the highest concentration of solute atoms. Gray markers show GB atoms (according to CSP), white markers correspond to atoms belonging to the grain interior, and red markers represent Nb atoms. Visual inspection clearly illustrates that virtually all solutes are located in the grain boundaries, which is expected due to the large size mismatch between Cu and Nb. The inset of Fig. 21 also shows that even for the largest amount of introduced Nb, no significant clustering of Nb occurs within the grain boundaries.

5

MATERIAL PROPERTIES

In a second characterization step, properties of the material, which are considered to influence the mechanical behavior [83, 56] and depend on the elemental distribution as well as the local composition were analyzed. Here, the generalized planar fault energy and the GB energy were investigated as a function of the concentration of solute atoms.

5.1 GENERALIZED PLANAR FAULT ENERGIES

The generalized planar fault energy (GPFE) is an intrinsic material property. It is considered to control dislocation nucleation and slip in NC fcc materials [75, 97] and affects the twinability [98, 99, 100, 101] of a given material. For fcc systems, the GPFE describes the energetic cost per unit area to form a n-layered fault by shifting n successive $\{111\}$ crystal planes along $\langle 112 \rangle$ direction [97]. Each plane is shifted for the length of a Burgers vector of a Shockley partial $b_P = a_0/\sqrt{6}$, where a_0 refers to the static lattice constant of the given material [168]. During shearing of a perfect crystal, an energy barrier needs to be overcome, which is called unstable stacking fault energy (γ_{usf}, Fig. 19) [169, 170]. It has been shown, that in reality the shearing of the crystal lattice has to occur along the identical energy path, resulting in the same extrema [170]. After the introduction of a stacking fault, further shearing of successive planes leads to the formation of a twin embryo [171].

The unstable fault energies define the barrier which needs to be overcome during shifting [97]. They can not be measured and need to be computed [168]. The evolution of the GPFE as reproduced by interatomic potentials for a given material may, however, deviate significantly with the description of the interatomic interaction [169]. For the unstable fault energies, it is not clear, whether this values even qualitatively agree with the real values, since they are not experimentally accessible [172].

The GPFE are commonly computed in two distinct ways. In one case, the shifting of two halves of the crystal versus each other is carried out as a rigid movement (unrelaxed GPFE). In the other case, the atoms in both crystal halves are allowed to relax perpendicular to the shearing plane (relaxed GPFE). The

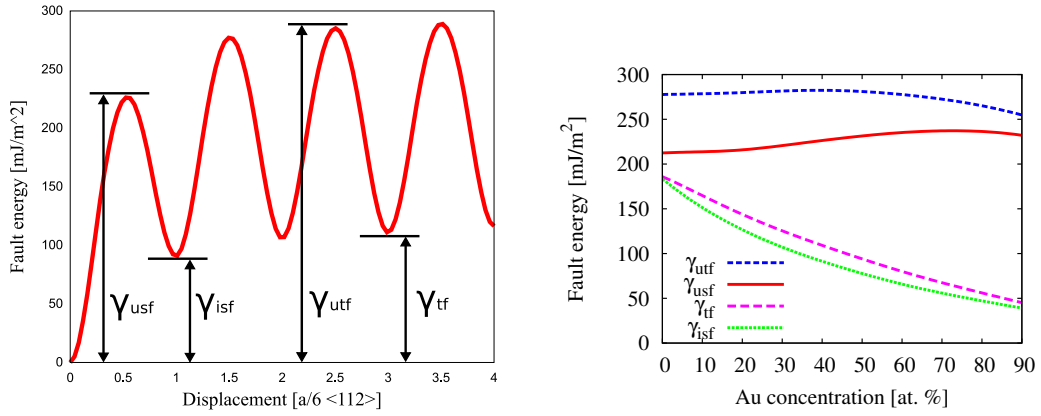

Figure 19: GPFE: (a) Relaxed generalized planar fault energy curve of Pd–Au (40%). The minima and maxima correspond to the unstable stacking fault, γ_{usf}, intrinsic stacking fault, γ_{isf}, unstable twinning fault, γ_{utf} and coherent twinning fault, γ_{tf}, energies; (b) γ_{usf}, γ_{isf}, γ_{utf} and γ_{tf} as functions of the Au concentration.

relaxed GPFE for the studied material systems as a function of composition (Fig. 19, Fig. 20) are discussed in the following.

PdAu

The relaxed GPFE for a Pd sample with 40% gold is shown in Fig. 19 a). The minima and maxima, which correspond to the unstable stacking fault, γ_{usf}, the intrinsic stacking fault, γ_{isf}, the unstable twinning fault, γ_{utf} and the coherent twinning fault, γ_{tf} are indicated. Fig. 19 b) demonstrates how the stable and unstable fault energies vary with the atomic fraction of Au. Notably, both, the intrinsic stacking and twinning fault energy decrease with increasing gold content, whereas the unstable stacking and twinning fault energies are only slightly varying with the Au concentration. The ratio between γ_{usf} and γ_{isf}, which is considered to control the nature of slip in NC metals [97], therefore depends on the composition of the alloy.

NiFe

The relaxed GPFE for Ni as reproduced by the interatomic potential used in this work [134] is in fair agreement with density functional theory calculations [169], even though the stable stacking fault energy is underestimated. Fig. 20 shows the evolution of the GPFE for various compositions of Ni–Fe for the case of a random alloy. It can be seen, how the intrinsic stacking fault energy (γ_{isf}) changes with the amount of Fe, while the unstable stacking fault energy (γ_{usf}) is nearly

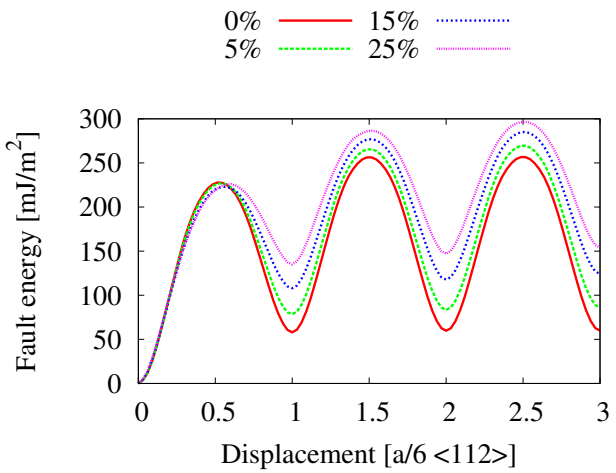

Figure 20: GPFE: Relaxed generalized planar fault energy curve of Ni–Fe (random alloy) for various compositions, where the Fe concentration varies from 0 to 25%.

unaffected. In contrast to Pd–Au (see above), where the introduction of Au is reducing the intrinsic stacking fault energy, the introduction of solute increases γ_{isf}. The presence of 25% of Fe in fcc Ni increases γ_{isf} by more than a factor of two as compared to pure Ni.

Consequently, the ratio between γ_{usf} and γ_{isf}, controlling the nature of slip in NC metals [97], changes with composition also for this material system.

In the following chapters (Sec. 6 and Sec. 8) it is explored, how a change of the intrinsic material properties through alloying affects the macroscopic deformation properties.

5.2 GRAIN BOUNDARY EXCESS VOLUME AND GRAIN BOUNDARY ENERGY

The free volume in the GBs or GB excess volume is one possible criterion for characterizing GBs [150]. The GB energy determines the energetic state of the interfacial configuration with respect to the ground state and is the major driving force for the elimination of boundary area, i.e. the occurrence of grain growth [173, 174]. Both, the GB excess volume and the GB energy can be drastically affected by the presence of solute atoms.

5.2.1 *The effect of segregating solutes*

Segregating solutes can suppress grain growth. This was confirmed experimentally for several systems [175] including Cu–Nb. The effect is mainly caused by a drastic reduction of GB energy, eliminating the driving force for an increase in grain size [173, 174].

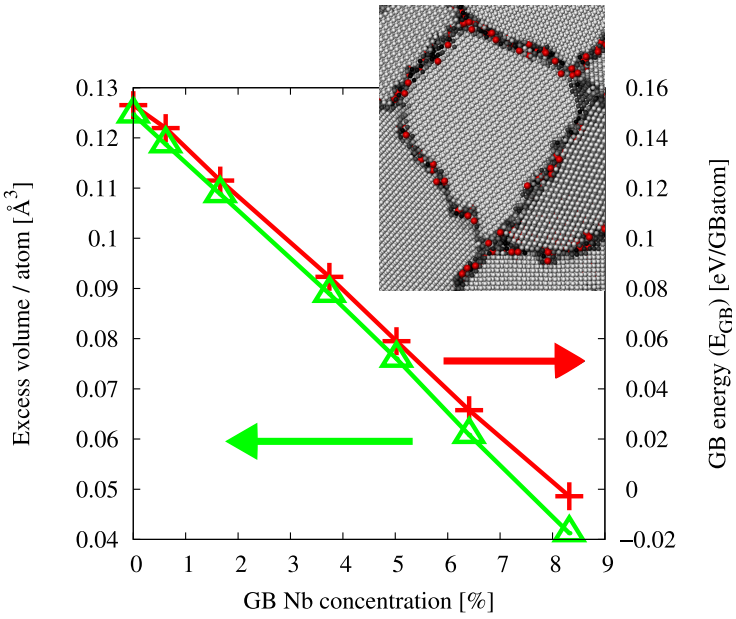

Figure 21: Atomic excess volume (green) and GB energy (red) in NC Cu–Nb at 0 K as a function of composition. Inset: cross-section of a grain and its surrounding GBs and triple junctions after equilibration and the introduction of solutes for 8.3 at.% of Nb in the GBs (corresponding to 1.9 at. % global concentration). The gradient gray scale corresponds to the centrosymmetry-parameter (a measure of the local lattice disorder) where light gray corresponds to 0 (grain interior) and dark grey to 5 (highly distorted regions). Nb atoms are highlighted in red. Snapshots were generated using OVITO [165].

In atomistic simulations, the total GB area is not easily accessible whereas the number of GB atoms can be readily obtained according to structural criteria (Sec. 2.4.2). Therefore, the GB energy E_{GB} is calculated at T=0 K from the relation,

$$E_{GB} = (E_{total} - E_{SC})/N_{GB} \tag{5.1}$$

where E_{total} is the total potential energy, E_{SC} is the energy of a cell with the same number of atoms contained in a single crystalline specimen of identical composition, and N_{GB} is the number of atoms in the GB according to CSP. (The single crystal reference structure was prepared as a random solid solution, thermally equilibrated and quenched to 0 K.) Under the assumption of constant GB widths, E_{GB} is proportional to the GB energy per unit area γ. Fig. 21 shows that the GB energy decreases linearly with solute concentration, in agreement with the findings of Millett et al. [90]. Noteworthy is that the GB energy falls slightly below 0 for the highest amount of introduced Nb. The absolute value of the GB energy, however, depends on its definition and the choice of the reference system. It shows, nevertheless, that the GB energy is dramatically reduced by the segregation of Nb to GBs. Fig. 21 also shows a similar dependence on composition for the atomic excess volume ΔV_{at},

$$\Delta V_{at} = (V_{total} - V_{SC})/N, \tag{5.2}$$

where V_{total} is the total volume of the system at its current state, V_{SC} is the volume of the same number of atoms contained in a single crystal of identical composition at the same temperature, and N is the number of atoms. The free volume in the GBs thus decreases with increasing content of Nb in the GBs. The observation that both energy and volume decrease linearly with concentration in Fig. 21 is a further indication that no significant precipitation is taking place and the GB remains homogeneous, since segregation energy and therefore GB energy as a function of composition may change due to solute-solute interactions away from the dilute limit [92].

The expansion of the GB e_{GB} due to the excess volume stored in the GB is a quantity, which is accessible also experimentally. It is defined as the change of the Volume V with the GB area A,

$$e_{GB} = \left(\frac{\partial V}{\partial A}\right)_{T,p,n_i} \tag{5.3}$$

at constant temperature T and pressure p and for a constant number of atoms n_i. The GB expansion is an excess property with respect to the ideal crystal and its value can be as low as 1/10 of the lattice constant [176]. From dilatometry a value of 0.32-0.35 Å was reported for ultra fine grained Ni [176], from density measurements a value of 0.23 Å was reported for NC Pd [177], while MD results yield an GB expansion of 0.28-0.42 Å in high-angle GBs in Ni [178].

For the NC Cu samples used in the presented work, we observe an average GB expansion of about 0.25 Å for pure NC Cu after thermal annealing under the assumption, that the GB area did not change drastically during annealing. The GBs in our computational model structures of pure metals seem therefore in good agreement with the GBs in experimental samples and other computational work. During alloying, however, the excess volume in the GBs and therefore also the GB expansion is drastically decreased as visualized in Fig. 21.

Part III

GRAIN BOUNDARY MEDIATED PLASTICITY

The following part deals with the effect of solute atoms on the macroscopic mechanical properties. Samples from different routes of solute introduction are compared, which helps to identify the atomic characteristics controlling the macroscopic properties.

Systematic variation of the strength controlling structural feature, the excess volume in the GBs furthermore allows the development of a new scaling law, which depends not only on grain size but on the GB excess volume and the GB relaxation state.

6

THE INFLUENCE OF MISCIBLE SOLUTES

The influence of miscible solutes on the deformation properties of NC microstructures is studied for the case of Pd–Au model structures of varying grain size (5-15 nm). Although this is a fully miscible system, the solute distribution is not fully homogeneous as reported in Sec. 4. By analyzing dislocation activity, atomic free volume in the grain boundaries, stacking and twin fault densities we make a connection between composition-dependent properties of the miscible alloy and the observed stress-strain behavior.

6.1 STRESS-STRAIN BEHAVIOR

6.1.1 *Compositional effects*

The observed stress-strain behavior for NC Pd–Au with two different grain sizes and three different concentrations is shown in Fig. 22 a). The slope in the elastic regime is larger for the samples with increased gold concentration, which is due to the enhanced elastic modulus of the bulk crystal at intermediate compositions as predicted by the Pd–Au potential. This stiffening is also caused by an increase of the modulus of the GB by chemical relaxation as will be shown below.

Besides the variation in the elastic regime, the yield stress shows a clear dependence on the concentration. This is particularly pronounced for the intermediate concentrations as can be seen in Fig. 23 a), where the maximum stress versus composition is plotted for different grain sizes.

The NC Pd–Au alloy exhibits an overshoot in the stress-strain behavior, which varies in height with composition. The origin of this overshoot, which is usually explained by the ultra-high strain rates used in MD simulations [54], is obviously more intricate in the case of the NC alloys.

For larger grain sizes, we observe strain softening at larger deformations irrespective of composition. This effect, which is also observed in experiments [35], was explained with residual internal stresses due to dislocations by Tang and Schoenung [179], and with the occurrence of cross slip by Brandl et al. [180]. Since we observe mainly partial dislocations in our samples, especially in Au rich samples, the later explanation cannot hold true for our simulations.

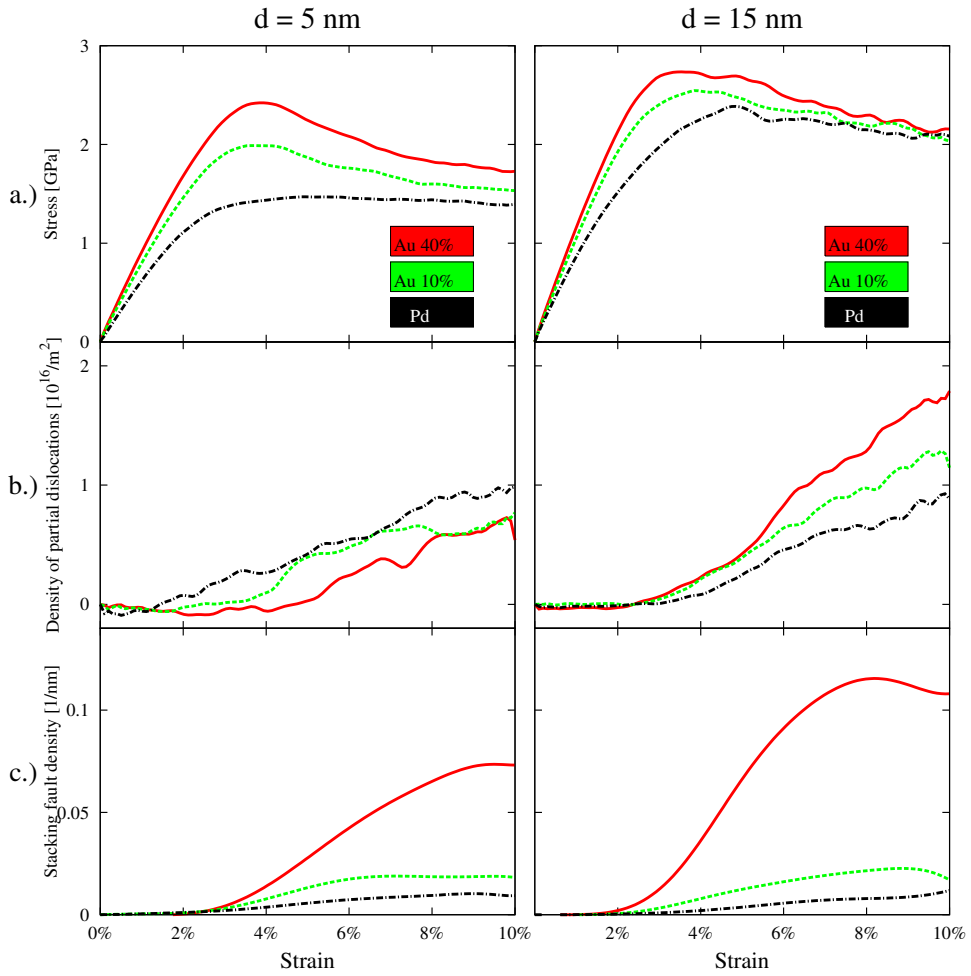

Figure 22: Compositional Effects: Stress strain behavior a), partial dislocation density b) and stacking fault density c) for two different grain sizes and three different compositions as a function of macroscopic strain.

As discussed in Sec. 5, the stable and unstable fault energies predicted by our model potential for Pd–Au are composition-dependent. That is, we can expect the deformation mechanisms to be composition-dependent as well. For investigating this dependence, we analyzed the activity of dislocations in the samples during deformation using ODDA (Sec. 2.4). This method allows to monitor the dislocation lines in all grains and to determine their Burgers vector. A statistical analysis of this data gives the total dislocation density, which continously increases during plastic deformation after dislocation nucleation from the grain boundaries has started (Fig. 22 b)). Since perfect $(a/2)\langle 110\rangle$ dislocations are resolved as two separate Shockley partials by the analysis algorithm, even for very small dissociation widths, the instantaneous dislocation density results mainly from Shockley partial dislocations. Note that dislocations in small-angle GBs are also detected by the analysis algorithm, resulting in a finite initial dislocation density in the as-prepared samples, which is assumed to be constant and subtracted from the instantaneous dislocation densities. Fig. 22 b) displays the measured dislocation densities in the NC alloys of different compositions. For the 15 nm grain size one can observe an increased dislocation activity in alloys with higher Au content at a given strain level. The leading partial nucleation resistance parameter ($R_{leading}$), which is obtained according to

$$R_{leading} = \gamma_{\mathrm{usf}}/Gb \tag{6.1}$$

[181, 182] can explain this findings. At intermediate compositions, $R_{leading}$ is reduced as compared to pure Pd (Fig. 23 b)) . However, the intrinsic stacking fault energy, γ_{isf}, is lowered by the addition of gold as well. This leads to a higher resistance parameter for the nucleation of trailing partials (quantified by $(\gamma_{\mathrm{usf}} - \gamma_{\mathrm{isf}})/Gb$), effectively locking leading partials in the grain interior. In addition, lowering the stacking fault energy leads to a widening of intrinsic stacking faults and increases the probability of dislocation-dislocation reactions, which result in immobile products like stair-rod dislocation segments. For the case of the 5 nm samples, the algorithm detects mainly dislocations in small-angle GBs. This results in a high initial dislocation density (not shown) and in larger scatter of the results as the GB structure is changed by GB sliding, hindering the identification of dislocations. Comparing the measured dislocation densities for the 5 and 15 nm grain size shows that in the 5 nm structures there is less dislocation activity, which is consistent with the general picture of a change from intragranular to intergranular mechanisms when the average grain size is decreased below a certain limit [183, 184, 185].

We have also measured the total density of intrinsic stacking faults (ISF) and coherent twin boundaries (not shown) in the samples as functions of strain (Fig. 22 c)). As expected, the addition of gold leads to a strong increase of ISF density.

While the composition-dependent fault-energies and derived properties like the resistance parameter R [181, 182] for (leading) partial nucleation can explain

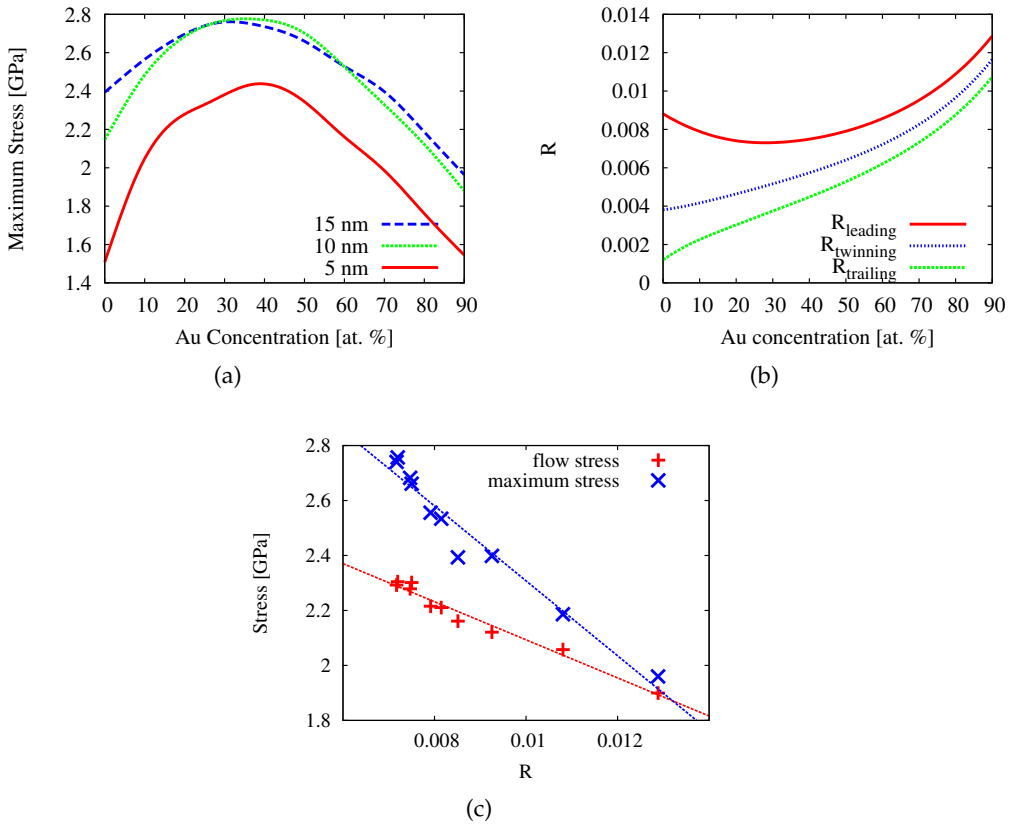

Figure 23: Compositional Effects: (a) Maximum yield stress as a function of composition for different grain sizes. (b) Resistance parameters R for the nucleation of leading partial dislocations (γ_{usf})/Gb, twinning partial dislocations ($\gamma_{utf} - \gamma_{tf}$)/Gb and trailing partial dislocations ($\gamma_{usf} - \gamma_{isf}$)/Gb as function of the Au concentration. (c) Correlation between Maximum Stress, Flow Stress and the resistance parameter R for leading partial nucleation in the case of the 15 nm grain size.

the measured defect density at a given strain (see above), they can not explain the increase in stress at the onset of plastic deformation. If the nucleation of a partial dislocation into the grain was the barrier to overcome at the onset of plastic deformation, one would expect a correlation between the maximum stress and the resistance parameter. Fig. 23 c) shows that the contrary is the case. Namely that the observed maximum stress in the stress-strain behavior correlates inversely with the resistance parameter to leading partial dislocation nucleation. Therefore, we can reason that it is not the nucleation of leading partial dislocations, which controls the maximum strength of this NC alloy.

Additionally, we can conclude, that the composition dependent resistance against partial dislocation nucleation into the grain has a minor effect on the observed stress-strain behavior. Since the model for the resistance to dislocation nucleation comes from the nucleation at a surface [170], it describes the resistance against nucleation into the grain. The model does, however, not include the necessity of accommodating the slip on the side of the GB. A change in the barrier for nucleation from the GB (for accommodating the slip) might therefore still affect the maximum strength especially in the case of a well equilibrated GB structure of high density.

Since we can exclude the composition dependent bulk material properties (controlling the intragranular deformation) from causing the composition-dependent increase in yield stress, we focus on the influence of the intergranular region in the following. To resolve, whether the increased maximum stress for the intermediate concentrations results from the introduction of solutes in general, or the positional configuration, we evaluate the impact of chemical GB relaxation in the next section.

6.1.2 *Chemical grain boundary relaxation*

Recently, Vo et al. [28] showed for NC Cu that the stress-strain behavior and the respective contributions of different deformation mechanisms depend on the state of GB relaxation of the sample. In order to elucidate the role of GB relaxation, we first performed an additional mechanical cycling (loading/unloading) of three times up to 2% strain in the elastic regime with one sample before doing the actual tensile test. This mechanical equilibration step in addition to the annealing treatment, however, did not change the stress-strain behavior of the sample as can be seen in Fig. 24.

As mentioned above, the high strain rate applied in the simulation is another factor that can affect the stress-strain behavior and possibly leads to an overshoot in the stress-strain curve [54]. For verifying this, we repeated the tensile test simulation at a 10 times lower strain rate, but find only a slight reduction of the height of the overshoot (Fig. 24). This provides evidence that the profile of the

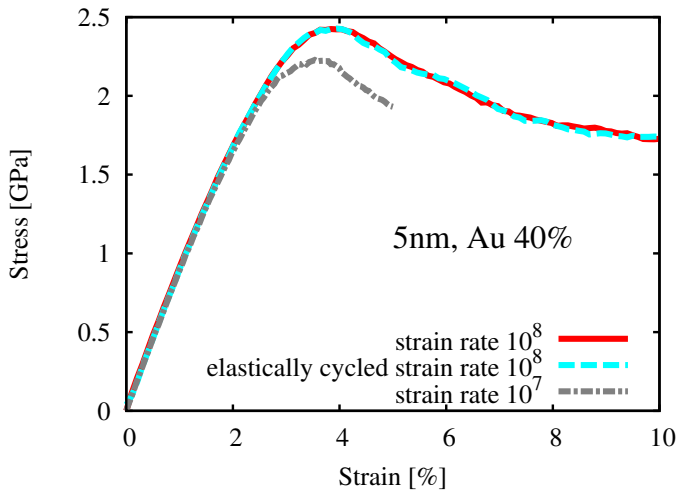

Figure 24: Strain rate effects and mechanical equilibration: Stress strain behavior of a (5nm, 40% Au) mechanically cycled sample (3 times to 2% strain) and deformed at a different strain rate (10e7) as compared to the chemically equilibrated structure. (One sample was only strained to 5% and did not fail where the stress strain curve ends.)

stress-strain curve is more influenced by the characteristics of the sample before deformation than by the suppression of thermally activated processes.

The fact that the overshoot occurs in the intermediate concentration range raises the question whether it is only caused by the increased modulus of the material or by some other property of the NC alloy. For answering this question, we generated NC samples with different degrees of chemical equilibration (Table 2).

Table 2: Different sample types and the according states of equilibration

Type	**Equilibration**
A	structurally and chemically equilibrated by hybrid MD/MC method
B	only structurally equilibrated random alloy
C	same as Type A but chemically disordered GB

The fully equilibrated samples (Type A) were discussed in Sec. 6.1.1. The samples of Type B were not chemically equilibrated. That is, the chemical ordering and composition of the GBs was left in the as-prepared state of an homogeneous, random solid solution similar to the bulk material. Additionally, we created samples (Type C), where the compositional deviation of the GBs (Sec. 4.1.1), was conserved, but the positioning of the different species within the GBs was chosen at random. That is, the local composition was in accordance with the results from

the chemical equilibration procedure, but the positional distribution of the solutes within the GB was not.

The results of the successive straining simulations are shown in Fig. 25. As mentioned above, the increase in modulus with increasing gold concentration is less significant for the case of the not fully equilibrated samples (Type B and C). Therefore we can reason that the stiffening also results from the chemical relaxation of the grain boundaries.

Most interestingly, for the samples of Type B and C, the yield stress drops massively and the profiles of the stress-strain curves become flat and similar to pure Pd as can be seen for the case of 5 nm grain size in Fig. 25 a). Note again that we have only changed the distribution of the solutes and/or the chemical structure of the GBs, but kept all other properties including the structural equilibration, global composition etc., the same. This shows that the details of the element distribution in the GBs play a very important role for the yield strength of this miscible alloy.

Comparing the dislocation activity of the samples of Type A (Fig. 25 b)) with the samples of Type B and C we can conclude, that the mechanisms within the grains are not significantly affected by the chemical relaxation state. Especially for the 15 nm grain size, where dislocation mechanisms contribute significantly to plastic deformation, we observe similar dislocation densities but a differing maximum stress for the samples of Type A and the samples of Type B and C, respectively.

This hints to the fact that the chemical relaxation leads to a low energy GB configuration being more stable against yielding than the GB present in the random alloy.

Monitoring the atomic volume in the GB as compared to the atomic volume in a single crystal of identical composition (Fig. 25 c)) shows that the samples of Type A have a lowered initial free volume in the GB than the samples of Type B and C. A significant part of this lowered initial free volume is due to the varying composition in the GBs, which can be seen while comparing Type B and C. During the course of deformation, the free volume in the GB of sample Type A is raised more significantly indicating a possible origin of a differing stress-strain behavior.

The relative change of the free volume in the GB (Fig. 25 d)) visualizes that for the case of the samples of Type B and the samples of Type C, the change in free volume in the GB does not deviate significantly from the behavior of pure Pd, which is the case for the samples of Type A. This supports our hypothesis that a GB structure stabilized by chemical equilibration is influencing the maximum strength.

The additional stabilization by chemical equilibration within the GBs has to be overcome to deform plastically resulting in an increased yield stress. That is, the free volume in the GB which is related to the relaxation state of the GB has to be increased more significantly in the GB of fully chemically equilibrated samples.

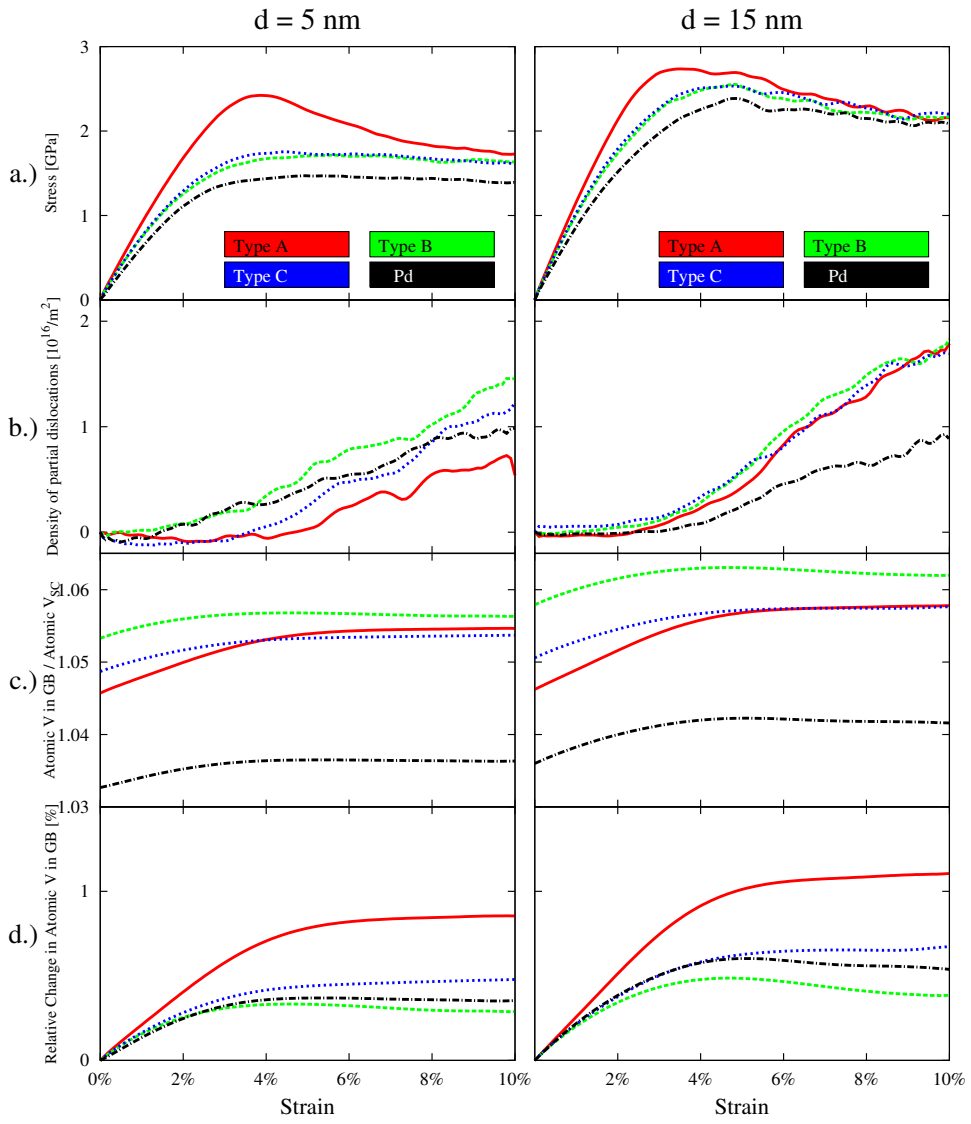

Figure 25: Effect of chemical GB relaxation: Stress strain behavior a), partial dislocation density b), atomic volume in the GB as compared to a singlecrystal c) and relative change in atomic volume in the GBs d) for two different grain sizes as a function of macroscopic strain for samples that were fully equilibrated (Type A), samples that were only structurally and not chemically equilibrated (Type B) and for structures, where the chemical order in the GBs was destroyed (Type C).

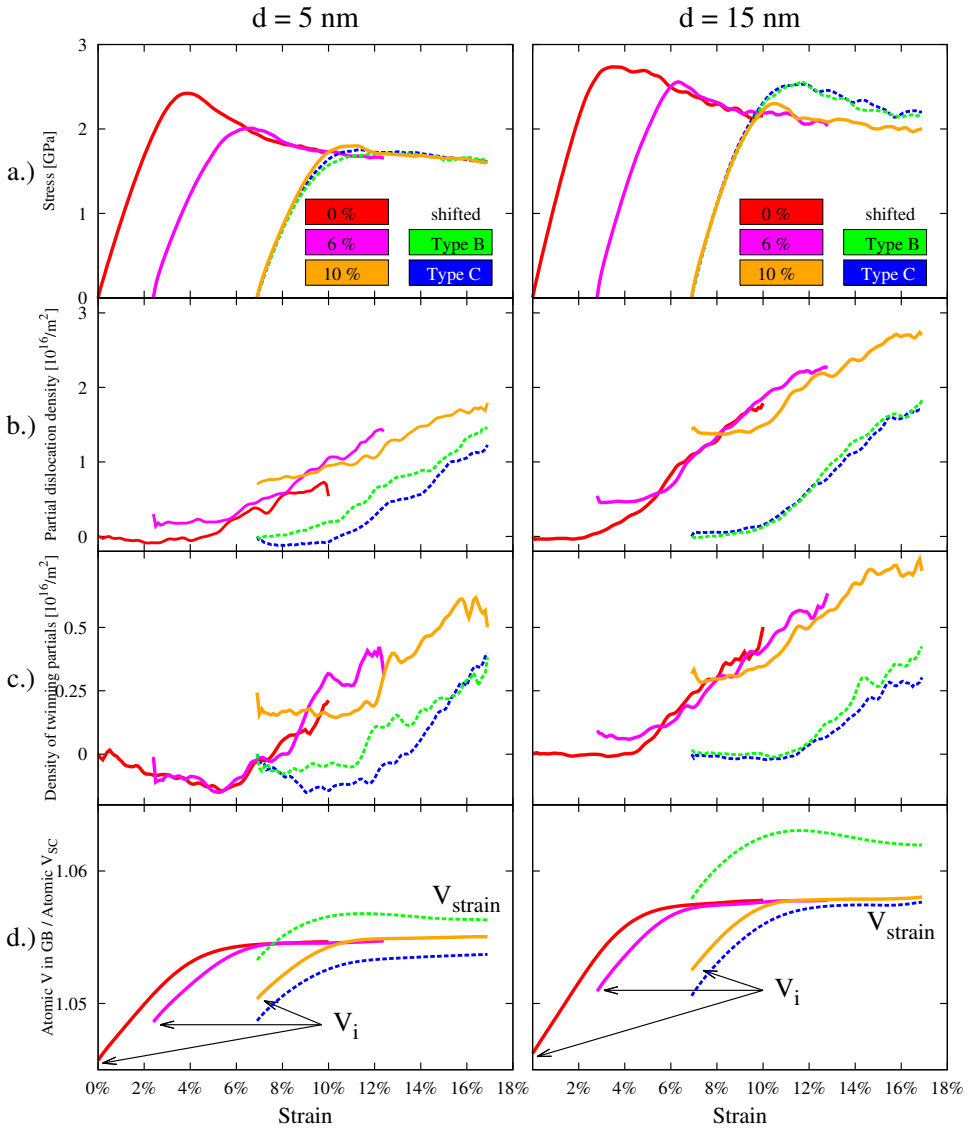

Figure 26: Restraining of the PdAu structures with 40% gold: Stress strain behavior a), partial dislocation density b), twinning partial density c) and atomic volume in the GBs d) for two different grain sizes and three different states of previous loading and relaxation as a function of macroscopic strain (full lines). For comparison, the data of the initial Type B and Type C samples (section 6.1.2) is also included and shifted accordingly (dashed lines).

For testing our hypothesis of the relaxation state of the GB controlling the yield strength, we investigate the influence of plastic deformation on consecutive deformation simulations in the following section.

6.1.3 *Re-straining effects*

The influence of the elemental distribution on deformation processes was studied in more detail by comparing the macroscopic mechanical properties and the defects within the structures for the case of fully equilibrated samples (Type A) with samples that were strained to 6% and 10%, relaxed to 0 pressure and then tested by means of a tensile straining simulation. For the grain sizes of 5 and 15 nm with 40% gold, the results are shown in Fig. 26. In order to facilitate comparison with the initial samples of Type B and C (Sec. 6.1.2) the data is also included and shifted accordingly. Note that the samples of Type B and C did not undergo the pre-straining procedure.

For the case of 5 nm grain size, re-straining a sample that was deformed to 10 % results in a stress-strain behavior similar to the case of the samples of Type B and C (included in Fig. 26 to facilitate comparison) where the overshoot decreases and strain softening is reduced (Fig. 26 a)). Re-straining a sample that was deformed to a lesser extent (6 %) results in a stress-strain behavior intermediate between the chemically equilibrated structure and a sample that was deformed to 10 %. Hence, a gradual destruction of the equilibrated structure causes a lowering of the maximum flow stress. For the 5 nm sample, which deforms plastically by GB mediated processes, we can therefore reason that chemical equilibration impedes GB plasticity. If the chemical order is destroyed (e.g. by a preceding deformation) or not reached in the first place (see Sec. 6.1.2), the sample approaches a steady-state deformation regime. The change in free volume in the grain boundary (Fig. 26 d)) supports this picture, where the re-strained samples start from a higher initial value and converge to a steady-state deformation level. The detected dislocations (Fig. 26 b, c)) also show an increase with increasing strain, but again less significant and with more scatter as compared to the larger grain sizes because of the contribution of GB dislocations as explained in Sec. 6.1.1.

For the samples with 10 and 15 nm average grain size, where intragranular deformation processes are more pronounced, the results are somewhat different (Fig. 26). Here, the re-strained samples (after 10 % strain), also show a reduced maximum stress, but their stress-strain curves fall below the ones of the samples of Type B and C (Fig. 26 a)). The deviation from the behavior observed for the 5 nm grain size can be explained by the evolution of defects within the grains of the samples. The grains within the initial, chemically or only structurally equilibrated samples are defect free whereas the preloaded samples contain a significant amount of planar defects and dislocations (Fig. 26 b, c)). Monitoring the dislocation activity shows that for the case of 15 nm samples, the increase in

partial and twinning partial dislocation density (partial dislocations on stacking fault or twinning fault planes) is more pronounced. The increase in twinning partial dislocations can explain the observed softening as compared to the sample of Type B and C based on an observation that was made for nanotwinned Pd [186].

Besides the increase in partial and twinning partial dislocations also an increase in free volume, plateauing in a steady state deformation level is observed for the restrained samples of 10 and 15 nm grain size.

We can therefore conclude that the relaxation state of the GB indeed controls the maximum strength of our NC material. Most surprisingly, the relaxation state has a significant influence also in the case of the 15 nm samples, where dislocation motion contributes significantly to plastic deformation.

The atomic free volume in the GB can, however, not explain the softening as compared to the samples of Type B and C as observed for the 15 nm grain size (Fig. 26 d)), since the change in free volume is similar. Therefore the differences in the stress-strain behavior must be caused by the intragranular defects (dislocations).

6.2 DISCUSSION

The stress-strain behavior of our model structures depend on the introduction of miscible solutes, where the positional distribution of the solutes plays a key role, while compositional deviations show a minor effect. For the case of fully equilibrated structures (Type A, Fig. 22) a significant increase in stiffness and strength is achieved by alloying. This effect vanishes for samples, which were not chemically equilibrated (Type B, C), irrespective of the compositional deviation of the GB (Fig. 25) and for samples, where the distribution of solutes is destroyed by deformation (Fig. 26). The monitored dislocation and ISF densities are not affected by the chemical equilibration. That is, the samples of Type B and C show the same dislocation behavior as the fully equilibrated structures (Type A). Thus, the observed differences in the stress-strain curves between the samples of Type A and the samples of Type B and C must arise from changed intergranular deformation mechanisms like GB sliding or from an increased nucleation barrier for dislocation processes because of GB equilibration. This is confirmed by the observed change in free volume in the GBs, where the fully equilibrated structures (Type A) show an initially lower atomic volume in the GB which needs to be raised more significantly in order to deform plastically.

Fig. 27 shows, that the observed maximum stress in the stress-strain behavior correlates to the increase in atomic volume in the GB during deformation for all observed relaxation states. The increase in atomic volume during deformation is here defined as the ratio between the (plateauing) free volume during straining

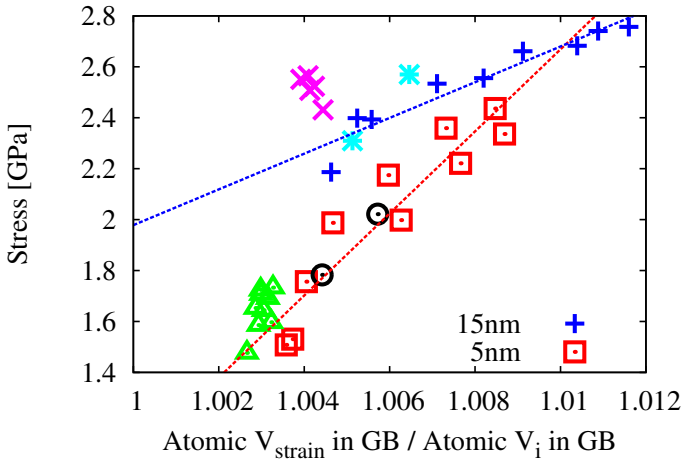

Figure 27: Correlation between maximum stress and the ratio between free volume during straining and the initial free volume for 5 and 15 nm grain size and different states of relaxation. Open symbols refer to the 5 nm grain size and crosses to the 15 nm grain size. Shown is the data for the chemically equilibrated samples (red, blue), the only structurally equilibrated samples (green, pink) and the restrained samples (black, turquoise). The data of previously not presented simulations (varying Au concentration from 10 to 90%) is also shown.

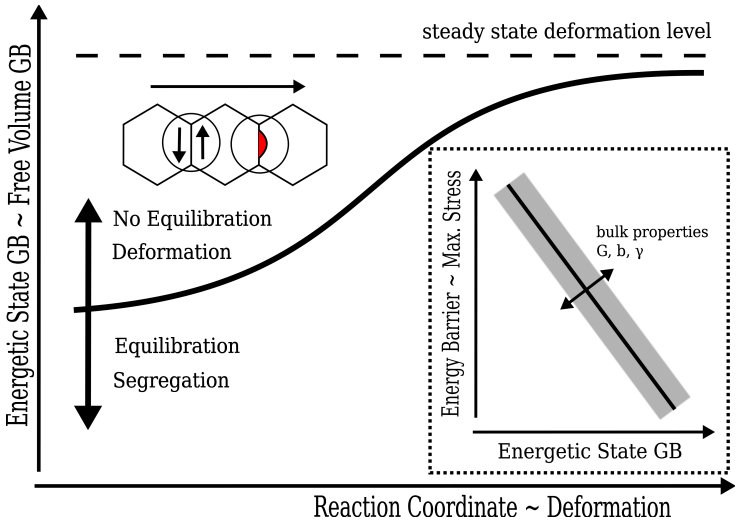

Figure 28: Schematic of the energetic state of the GB and its dependence on initial relaxation, GB segregation and deformation. The inset shows, how the energetic state of the GB influences the barrier for the onset of plastic deformation or the maximum stress, where properties of the bulk material play a minor role (see text).

and the initial free volume (Fig. 26 d)). That is, the more free volume needs to be generated, the higher the maximum strength.

For the case of larger grain sizes, GB equilibration can, however, not explain that the stress-strain curve for the re-strained samples falls below the stress-strain behavior of the samples of Type B and C (Fig. 26 a)). According to our hypothesis of the relaxation state of the GB controlling the maximum strength, one would expect a similar stress level, independent on the way, in which the chemical order in the GB was destroyed. Here, the dislocation analysis reveals that the observed differences originate from the presence of defects within the grains. Fig. 26 shows how the density of twinning dislocations depends on the condition of the material. In the re-strained samples, the nucleation of twinning partials is facilitated by the pre-existing stacking and twinning faults, resulting in a softening of the material. This effect is in agreement with an observation that was made for nanotwinned Pd [186].

According to our observations, one can reason, that the energetic state of the GB is correlated to the free volume in the GB and depends on the treatment of the structure and equilibrating processes (e.g. the positional configuration of solutes within the GB). During the course of plastic deformation (Fig. 28), this energetic state of the GB (and the atomic volume in the GB) has to be raised to a steady state deformation level. The initial energetic state of the GB in turn controls the barrier for the onset of the deformation mechanisms, which is correlated to the maximum strength (inset of Fig. 28). The properties of the bulk material (e.g. shear modulus, burgers vector) appear to have a less significant influence. For the case of a grain size, where intragranular mechanisms contribute significantly to plastic deformation, the initial density of defects within the grains also plays a role.

6.2.1 *Experimental evidence*

Relaxation of GBs can experimentally be accessed by differential scanning calorimetry (DSC). Here, GB relaxation is manifested through a large heat release in the absence of grain growth (and significant hardening) as reported for NC Ni–W [27].

In order to measure the relaxation of the GBs also for the presented Pd–Au alloy, NC IGC samples were prepared, equilibrated and deformed at the Saarland University and then tested in an heatflow differential calorimeter (DSC Q2000 from TAInstruments) [187]. Fig. 29 (a) shows the measured heat flow as a function of temperature for the case of an as-prepared sample (initial) and a sample which was annealed. For the initial as-prepared sample, a clear DSC signal prior to grain growth is present. Grain growth then sets in at a temperature of about 200 $^{\circ}C$ as indicated by a large increase in heat flow. The annealed sample on the contrary, which was tempered at about 150 $^{\circ}C$, does not show the DSC signal

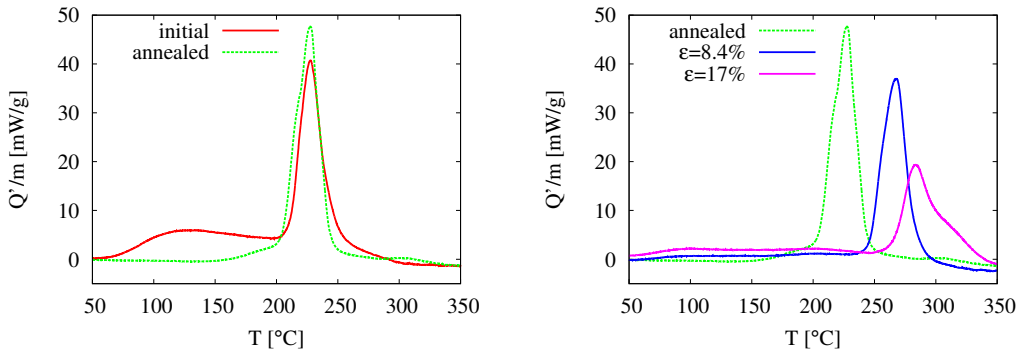

Figure 29: DSC measurements of NC Pd–Au (16%) [187]. Heat flow as a function of temperature for various sample conditions: (a) after initial preparation ("initial", red) and after GB equilibration ("annealed", green); (b) after GB equilibration ("annealed", green) and after successive deformation to a total strain of 8.4 and 17 % (blue and pink, respectively). (Courtesy of M. Deckarm, C. Braun, K. Schmitt, and R. Birringer.)

attributed to GB relaxation. This approves that as-prepared GBs are not in a well equilibrated state, which can be achieved by thermal annealing below the onset of grain growth. It also shows that once the GBs are equilibrated, no heat release occurs prior to grain growth. Fig. 29 (b) shows the DSC measurements after deformation to 8.4 and 17 % of strain, respectively. Obviously, the heat release in the temperature range of GB relaxation is increased as compared to the equilibrated sample [187]. This supports our finding from MD simulations, where we showed that a well equilibrated GB structure offers an additional barrier to deformation, which needs to be destroyed in order to deform plastically. The observed shift of the signal attributed to grain growth after deformation is subject of ongoing research.

7

MODULATING THE FREE VOLUME IN THE GRAIN BOUNDARY

In the previous chapter (Sec. 6) we showed that the free volume in the GBs is a good measure of the equilibration state of a GB and controls the strength of a NC microstructure. In Sec. 5.2 we showed for the case of segregating solutes and the dilute limit that the free volume in the GBs scales linearly with the concentration of the segregating solute as does the GB energy. Now we investigate the yield strength of dilute NC Cu alloys.

For testing the influence of various segregating solutes on the deformation properties of NC microstructures, NC Cu samples of 8 nm grain size consisting of 38 grains were prepared and decorated with different segregating solutes as described in Sec. 3. The samples were then tested in compressive straining simulations as described in Sec. 2.5 at an engineering strain rate of 10^9 1/s.

7.1 STRESS-STRAIN BEHAVIOUR

7.1.1 *Compositional effects*

The segregating solutes, Nb, Fe and Ag were introduced into NC Cu samples with average compositions varying from 0 to 1.9 at.% for Nb, 1.5 at.% for Ag, and 1 at.% for Fe. The interatomic potentials introduced earlier (Sec. 2.1.2) were employed, to describe the atomic interactions. The yield strength of the samples was determined from stress–strain curves obtained in uniaxial compression. A deformation rate of 10^9 1/s was employed, since calculations with a lower strain rate (10^8 1/s) showed no qualitative difference. The yield strength is defined here as the stress obtained using a 1% offset in the stress–strain curve, since this represents the approximate strain at which the deformation becomes irreversible in MD simulations [29].

In Fig. 30 the yield strength in NC Cu as a function of solute concentration is shown for the three investigated alloys. The yield strength increases nearly linearly with solute concentration up to 1.2 at.% for the three types of solute. At larger concentration, the strength of the Cu–Nb samples shows a deviation from the linear trend. The solute concentration in the GB at this transition point

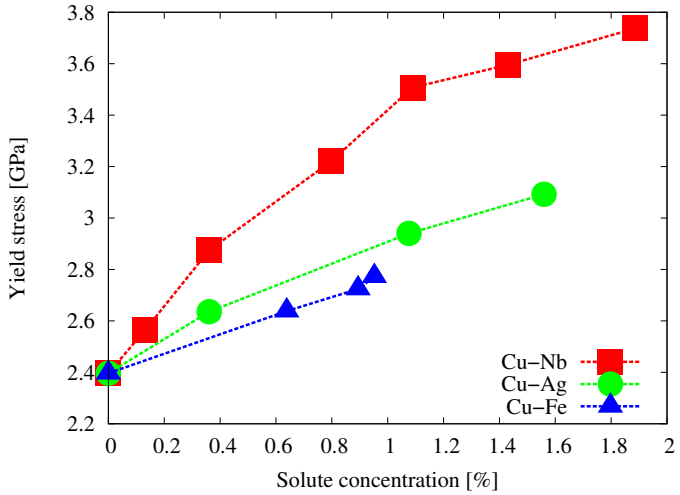

Figure 30: Yield stress as a function of composition for three different segregating NC Cu alloys.

is 6 at.% for Cu–Nb, and solute–solute interactions at the onset of deformation are likely to become significant. The yield strength of the sample with 1.2 at.% Nb has increased by about 60% with respect to the pure sample, while for the samples with 1.2 at.% Ag or Fe, the increase is about 30% and 20%, respectively. These large increases in yield strength are remarkable considering the already high strength of pure NC materials. For example, the strength of defect-free single crystalline Cu deformed in compression along [1 0 0] is about 3.7 GPa [188]. The strength of the NC Cu–Nb sample thus appears to be reaching the value of this "theoretical" strength of Cu. This observation is analogous to the so-called Borisov model of diffusion [189], for which the activation energy for GB diffusion increases to that of self-diffusion as the GB energy goes to zero. For all three segregating solutes, the GB energy decreases nearly linearly with the average solute concentration. It is observed, moreover, that the addition of about 1.9 at.% Nb (which corresponds to a concentration in the GBs of about 8.3 at.%) leads to a reduction in the GB energy to about 0 eV/atom (Sec. 5.2).

The correlation between yield strength and specific GB energy is shown in Fig. 31, where the yield strengths for all samples are plotted as a function of their GB energy. The data for nearly all samples lies on a single curve. The correlation between yield strength and GB energy is next explained using the simple model introduced in [28] to explain the dependence of flow stress on grain size and GB energy. In that model the flow stress was written in the form

$$\frac{1}{\sigma} = \frac{1}{k_1 + k_2/\sqrt{d}} \cdot \left(1 - \frac{N_{GB}}{N_{total}}\right) + k_3 \cdot E_{GB} \cdot \frac{N_{GB}}{N_{total}} \tag{7.1}$$

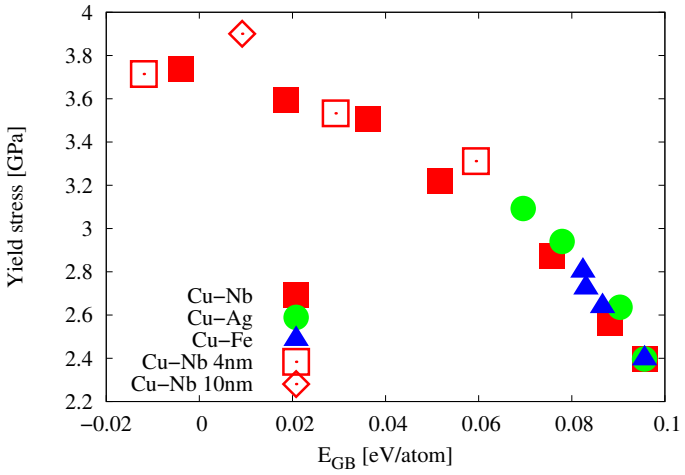

Figure 31: Yield stress as a function of GB energy for the three studied NC Cu alloys, where different grain sizes are compared for the case of Cu–Nb (see text).

where σ is the flow stress, d is grain size, k_1, k_2 and k_3 are fitting parameters, E_{GB} is the specific GB energy, and N_{GB} and N_{total} are the number of atoms in the GBs and the total number of atoms, respectively. The two terms on the right-hand side of Eq. (7.1) represent a competition between traditional Hall–Petch hardening and GB softening. For samples with a large ratio, N_{GB}/N_{total} (small grain size), the second term dominates, while the first term dominates for samples with relatively few GB atoms (large grain size). Eq. (7.1) was shown to fit well to a large data set obtained for different grain sizes and thermal annealing times [28]. At small strains of 4-5%, GB sliding is known to predominate, and the second term is far more important [29, 50, 190]. The stress in Eq. (7.1) refers in the present work to the yield stress, i.e., small-strain regime, and consequently the inverse yield stress should scale almost linearly with $E_{GB} \cdot (N_{GB}/N_{total})$ where, for pure samples, E_{GB} is assumed constant (0.085 eV atom^{-1}). As shown in Ref. [29], N_{GB} decreased during thermal annealing due to GB relaxation, and not to a change in grain size. Eq. (7.1) then requires only a single fitting parameter (k_3), and the yield strength does not depend simply on grain size. In contrast to previous work using thermal annealing, N_{GB}/N_{total} is now left nearly constant (0.25), and E_{GB} is systematically varied by injecting solute into the GB. N_{GB}/N_{total} varies by less than 10% in the different samples, since the solute concentration is small. All samples have the same grain size and are annealed for the same amount of time. Fig. 31 demonstrates that the predicted scaling of yield strength with specific GB energy, E_{GB}, remains valid for these alloys. As an additional test of this model, NC Cu–Nb was created with two other grain sizes, 4 and 15 nm. Yield stresses as a function of E_{GB} of these samples doped with different amounts of Nb solute by

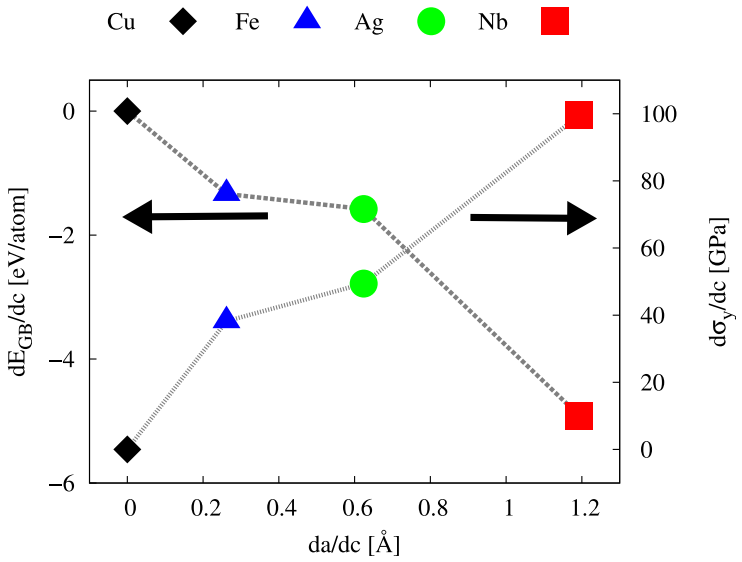

Figure 32: Efficiency of segregating solutes: Effect of the introduction of solutes on the GB energy an the yield strength for the studied NC Cu alloys as a function of atomic size mismatch.

the hybrid MD/MC method are also plotted in Fig. 31. The E_{GB} for these samples has been scaled, however, by N_{GB}/N_{total} for comparison with the 8 nm samples. These data fit very well with the trend of the 8 nm samples. Simulations at a lower strain rate ($1 \times 10^8 s^{-1}$) showed the same trend, although the absolute value of the yield strength decreased by about 10%.

In the previous chapter (Chap. 6), we showed that the strength of NC Pd–Au alloys scale with the GB volume. As discussed above, the yield stress in pure NC Cu scales with N_{GB} and thus scales also directly with GB volume. For the alloys, N_{GB} is no longer a valid measure of GB volume, since the different solutes have different atomic volumes. Here, however, a linear scaling between specific GB energy and specific GB volume was observed (Sec. 5.2). The linear relationship between these two quantities implies that the yield strength can be described either in terms of the GB volume or in terms of the GB energy for the presented case of segregating solutes.

7.1.2 *Efficiency of segregating solutes*

Lastly, we comment on the efficiency of each type of solute for increasing the yield strength. Plotted in Fig. 32 are the decrement of GB energy (dE_{GB}/dc) and the increment of yield strength ($d\sigma_y/dc$) as a function of lattice constant increment (da/dc) in single-crystalline Cu, i.e., lattice mismatch. The nearly linear trend shows that strength increases nearly proportionaly to the atomic size

mismatch. The finding, that strength increases with increasing atomic volume of the solute, agrees with the results of Ref. [108], where Lennard-Jones potentials were employed.

7.2 DISCUSSION

We could show for solute-doped NC Cu samples that (i) GB energy decreases as solute concentration increases, and (ii) the yield strength scales with the GB energy (and the GB volume). We revealed, moreover, that the GB energy depends on the type of solute in the GB. Solutes with a large size mismatch are more effective in reducing GB energies. The results suggest a new scaling behavior for the onset of plasticity in NC materials, one that is controlled not by the grain size alone, but by a combination of both the molar fraction of GB atoms and the degree of GB relaxation, as measured by the specific GB energy or the specific GB volume of the sample.

Our results fall in line with experimental results, where an increase in hardness was observed after annealing and GB segregation for the case of NC Ni [104]. Furthermore, a linear dependence between the mechanical strength of NC Cu and the amount of introduced Nb was reported also experimentally [175], where precipitation hardening could be excluded and GB hardening was suggested as explanation.

Part IV

CONTROLLING DISLOCATION MOTION AND ACTIVITY

In Sec. 6, we showed that the equilibration state of the GB has a significant influence on the macroscopic mechanical properties of NC alloys. Now we will study, whether the movement of dislocations in the grain interior is affected by the presence of solutes in a similar manner as observed for CG material.

Furthermore, it needs to be resolved, if dislocation motion in the grain interior is crucial for the ductility of NC samples. This is done studying intermetallic phases, where only GB mediated plasticity occurs.

The following section therefore deals with solid solution strengthening in NC metals and with plastic deformation of NC alloys where dislocation motion is prevented by grains consisting of an intermetallic phase.

8

SOLID SOLUTION STRENGTHENING

Regarding the mechanical properties of disordered NC Ni–Fe alloys several experimental observations are reported. NC disordered Ni–Fe (5.6 % Fe) with an average grain size of 10 nm showed a tensile yield strength in the order of 2 GPa and an increase in strength after annealing even though some grain growth was observed [191]. It was reported that plastic deformation processes in NC Ni–Fe (15 % Fe) undergo a transition with applied strain, where at low strains the strain is mainly accommodated by the grain boundaries while at large strains dislocation motion becomes dominant [190]. It is, however, not clarified, whether the observed strengthening results from conventional solid solution strengthening.

The interaction between substitutional solutes and dislocations can be explored by independently modulating the composition inside the grain interior. In this section, we present deformation simulations of disordered NC Ni–Fe. Samples with 5 nm and 15 nm average grain size were constructed (Sec. 3), characterized (Sec. 4) and tested in tensile straining experiments as described in Sec. 2.5. Several cases, where the composition in various parts of the microstructure is modified individually are compared.

8.1 RANDOM ALLOY (15 NM): VARYING THE GRAIN COMPOSITION

For CG material, the strengthening effect of substitutional solutes (i.e. solid solution strengthening) is widely known. In order to investigate, whether substitutional solutes in the grain interior have an effect on the macroscopic mechanical properties for the case of a NC solid solution, samples with differing composition inside the grains but identical GB (composition and structure) were compared. The initially equilibrated structure was identical for all cases with a concentration of 20 % Fe in the GBs. Different amounts of Fe (5 %, 15 % and 25 %) were then distributed randomly in the grain interior prior to deformation.

Fig. 33 shows slices through the initial microstructure for two different compositions, where the random distribution and differing amount of solute in the grain interior is visualized. Fig. 33 furthermore shows the stress-strain behavior and the evolution of dislocations in the microstructure under tensile load. Here it can be seen that a differing composition of the grain interior but identical GB

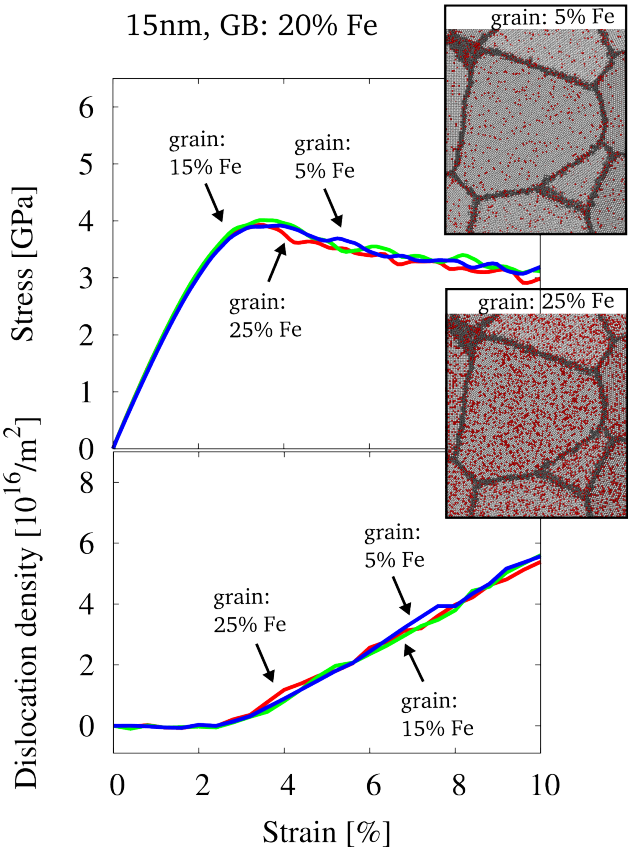

Figure 33: Stress-strain behavior and dislocation density for structures of 15 nm grain size, which were equilibrated by the hybrid MD/MC scheme at a global composition of 25 % Fe. The distribution of solutes in the grain interior only was then randomized and the composition inside the grains was changed prior to deformation. The data for three different concentrations inside the grains is shown. Additionally, two snapshots of the initial configuration visualize the solute distribution for two different compositions. Color coding is identical to Fig. 15.

structure (and composition) has little effect on the macroscopic behavior. Neither the stress-strain behavior nor the dislocation density show a dependence on the amount of solute, distributed randomly in the grain interior. The dislocation density for all cases, however, drastically increases during straining. This indicates, that for this grain size dislocation motion significantly contributes to plastic deformation, which is consistent with expectations [50]. An effect of differing solute concentrations on the mobility of dislocations, e.g. a pinning effect could therefore be expected, but is not observed. For the presented case, the stresses required for dislocation nucleation from the GBs are, however, so high that solutes inside the grains do not provide an effective barrier for dislocation motion.

8.2 random alloy (15 nm): varying the grain boundary composition

The delicate interplay between solute distribution and mechanical response of this NC alloy was further studied on samples, where the random solid solution inside the grain interior was held at a constant composition of 25 % Fe, but different amounts of solute were introduced into the GB during equilibration. That is, the NC structures were equilibrated via the MD/MC scheme at differing global compositions and the grain interior was then adjusted to a random solid solution with a constant composition (prior to deformation). Fig. 34 shows snapshots of a representative grain and the surrounding GBs inside the microstructure for two different cases, where a similar distribution of solutes is present inside the grains, but the GB composition is varied. The corresponding stress-strain behavior (Fig. 34) reveals, that there is a dependence on the amount of solute added to the GB via the MD/MC scheme, while the evolution of dislocations stays similar for all cases and is therefore not affected. The effect of different amounts of solute in the GB is more pronounced for the onset of plastic deformation. This is consistent with other studies, where it was reported that during the initial stages of deformation, GB plasticity contributes more significantly to the overall plastic deformation [50].

Similar to the case of a completely miscible system (Sec. 6), the amount of solutes inside the GB and the equilibration state of the GBs is controlling the strength of this NC alloy.

8.3 discussion

From the structures with an equilibrated GB and a random solid solution of varying composition inside the grain interior, we find, that there is little effect of the composition of the grain interior on the macroscopic mechanical properties. The DXA [158] reveals, that there is a considerable amount of dislocation activity inside the grains, which is in accordance with expectations for this grain size

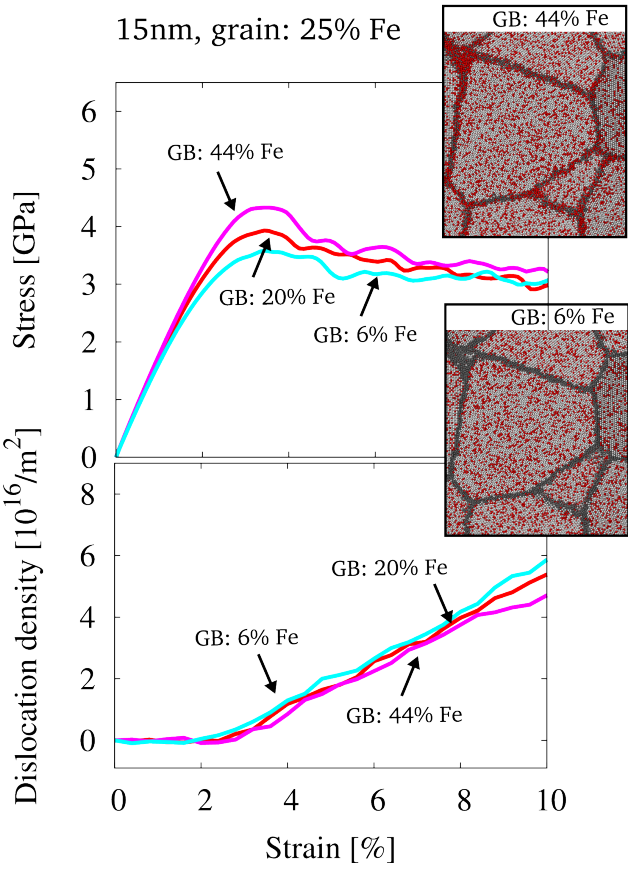

Figure 34: Stress-strain behavior and dislocation density for structures of 15 nm grain size, which were equilibrated by the hybrid MD/MC scheme at different global compositions (22, 25 and 29 % Fe). The distribution of solutes in the grain interior only was then randomized with a constant composition of 25 % inside the grains prior to deformation. The data for three different concentrations in the GB is shown. Additionally, two snapshots of the initial configuration visualize the solute distribution for two different GB compositions. Additionally, the snapshots of the atomic configuration at the according strain visualize the onset of intergranular fracture. Color coding is identical to Fig. 15.

[50]. It is concluded that solid solution hardening is not present in the described structures. The stresses, necessary for GB sliding and dislocation nucleation obviously exceed the stresses required for dislocation motion even in the presence of substitutional solutes.

We can furthermore conclude, that the barrier for dislocation nucleation is also not controlling the strength of the material. The barrier for the nucleation of dislocations, which is controlled by the GPFE and changes with composition (as shown in Sec. 5) apparently does not affect the mechanical response of the structures (Fig. 33).

From the samples with an equilibrated GB of varying composition and a random solid solution with constant composition inside the grains (Fig. 34), we observe, that the composition of the GB has an effect on the macroscopic mechanical properties. Here, an excess in Fe strengthens the structure, while a depletion in Fe decreases the strength. This is consistent with findings for miscible systems, where a maximum in the strengthening effect of solutes was observed for intermediate compositions (Sec. 6). Since the dislocation density inside the grains does not change also for this case, the differing strength must therefore result from the state of the GB. The drastic increase in dislocation density, however, shows that a large fraction of plastic deformation is carried by intragranular defects. This could explain, why the difference in the response vanishes for larger strains, where intragranular defects contribute more significantly, which is reported also from experiment [190].

9

SUPPRESSED DISLOCATION ACTIVITY

In metal alloys with a tendency for chemical ordering, like i.e. intermetallics, grain refinement to the nanometer scale has been considered as a possible route for achieving room temperature ductility in this otherwise brittle class of materials [192, 193]. The underlying assumption is that for very small grain sizes plasticity can be carried by GB mediated processes rather than by energetically expensive superlattice dislocations [194, 195]. The experimental realization of a NC microstructure of an ordered alloy, however, strongly depends on the route of preparation. For electrodeposited NC Ni–Fe alloys (up to 28 % Fe) a solid solution with no chemical order was observed [166]. In Ni_3Al, a partially ordered state was found after rolling at liquid nitrogen temperature to obtain a nanometer grain size [196]. In nanostructured Ni_3Al processed by ball milling [197] or high pressure torsion [198], on the contrary, a complete loss of order is observed during preparation. Grain refinement by SPD of B2 FeAl leads to a partial destruction of the long range order and the formation of ordered nanodomains with a size of about 2 nm, which can grow to the size of grains upon heating and restore the order [199].

In this chapter, we present deformation simulations of $L1_2$ ordered NC Ni–Fe. Samples with 5 and 15 nm average grain size as presented in Sec. 3 and Sec. 4 are tested in tensile straining experiments (Sec. 2.5), where different global compositions are compared.

9.1 ORDERED ALLOY (15 NM): VARYING THE GRAIN BOUNDARY COMPOSITION

For the case of an ordered grain interior, dislocation processes are suppressed, since the nucleation of superdislocations cannot be expected for the presented strain rates and no fcc-like slip planes are available in the $L1_2$ structure. The structures with an ordered grain interior as obtained by equilibration via the MD/MC scheme are therefore expected to deform mainly by GB mediated processes. Fig. 35 shows the stress-strain behavior and evolution of dislocations under tensile load for the structures of 15 nm grain size and varying composition. Obviously, the stress-strain behavior has a clear dependence on GB composition,

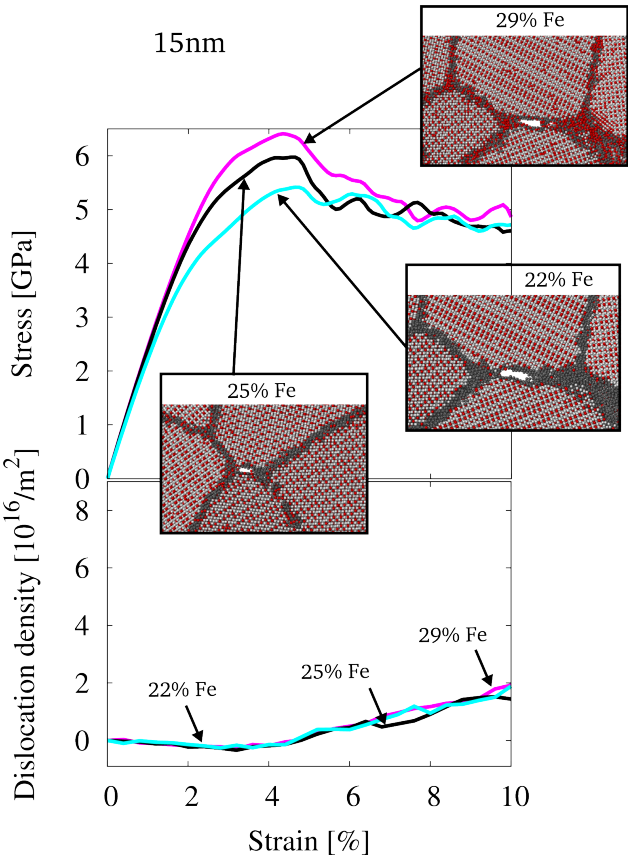

Figure 35: Stress-strain behavior and dislocation density for structures of 15 nm grain size, which were equilibrated by the hybrid MD/MC scheme at different global compositions (22, 25 and 29 % Fe). The snapshots of the atomic configuration at the according strain visualize the onset of intergranular fracture. Color coding is identical to Fig. 15.

while dislocation activity is suppressed. The yield stress is also here increased for the case of a structure with GBs enriched in Fe and decreased for a structure with GBs fully depleted in Fe. This is similar to the case of a disordered grain interior as reported above, but even more pronounced.

At the onset of plastic deformation, however, intergranular fracture occurs within the presented structures. This is visualized in the snapshots shown in Fig. 35, where slices through the atomic configuration are presented for various stages of deformation. Apparently, suppression of dislocation activity inside the grain interior leads to intergranular fracture, since GB mediated processes cannot be accommodated in samples with relatively large grains (15 nm).

9.2 ordered alloy (5 nm): varying the grain boundary composition

Since the suppression of dislocation activity leads to intergranular fracture for the 15 nm grain size, the data for the 5 nm grain size is presented here, where a larger contribution to plastic deformation by GB mediated processes can be expected. Fig. 36 shows the corresponding stress-strain behavior, evolution of dislocations and change in GB volume under tensile load. Representative slices through the microstructure at 10 % total strain are shown, which indicate that intergranular fracture did not occur for the structures with a grain size of 5 nm. From the stress-strain behavior, we find a strong dependence on the GB composition. The dislocation density reveals, that this is not caused by the evolution of intragranular defects, what is consistent with expectations based on the small grain size. Monitoring the state of the GB in terms of the GB volume (V_{GB}) shows that there is a strong similarity between the evolution of the GB volume and the stress during straining.

The analysis of data for the 5 nm grain size pronounces the observations made for the larger (15 nm) grain size. For the presented material, the configuration of the GB controls the mechanical properties in the nanometer regime.

9.3 controlling the strength - state of the grain boundary

For quantifying the relaxation state of the GB, we compute the change in GB volume during straining. In Fig. 36, it can be seen that the trend in the evolution of the GB volume and the stress during straining are quite similar. The correlation between the yield stress of the material and the change in GB volume at the yield point is analyzed in order to quantify the relation between the onset of plastic deformation and the increase in free volume in the GBs. Experimentally, it was observed, that the 0.2 % offset cannot be used as a yield criterion for NC metals (NC Ni–Fe) [190]. From *in-situ* X-ray peak profile analysis it was reported, that the transition from micro- to macroplasticity rather occurs around 0.7 % for NC Ni [200]. We therefore took the 0.7 % offset as a yield criterion for the presented data and extracted the yield stress as the stress at a plastic strain of 0.7 %. For the same plastic strain, the change in GB volume was extracted from the data. (It shall be noted, that the results are rather insensitive to the choice of the offset or employing the maxima in the stress-strain behavior as a criterion for yielding.) Fig. 37 shows the correlation between the yield stress and the change in GB volume. Obviously the data for different stages of equilibration and different stages of ordering falls on the same trend. Remarkably, even the data for different grain sizes lies on the same trend, irrespective of the state of the grain interior. (The data for structures, which were not discussed in detail is also shown.) It becomes evident, that the state of the GB and therefore the necessary increase in free volume controls the yield strength of the material. This is consistent with the observations made for

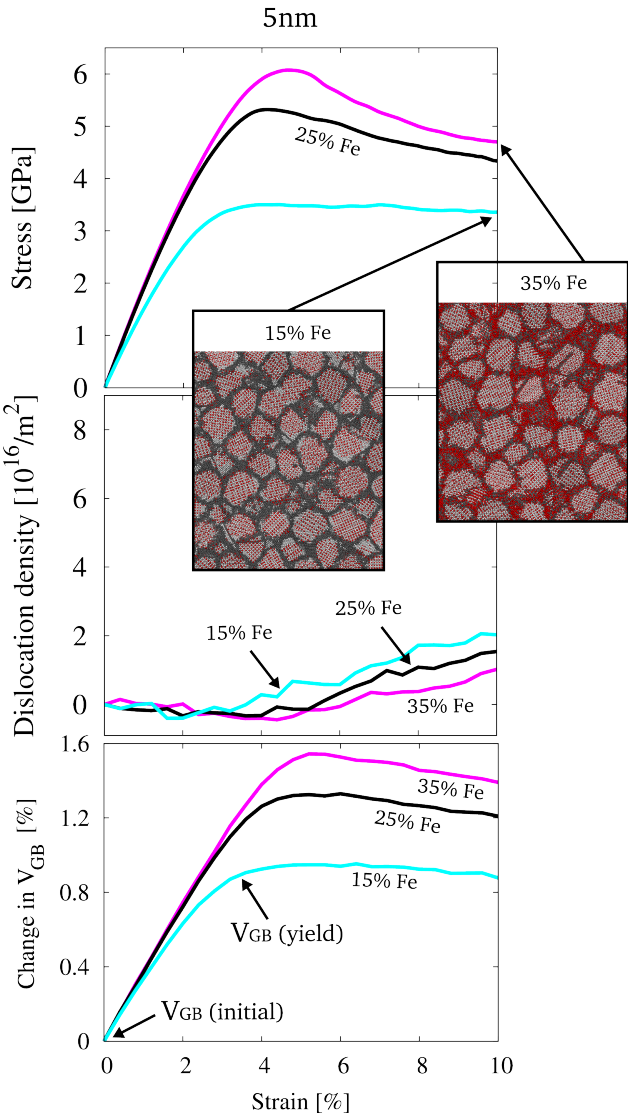

Figure 36: Stress-strain behavior, dislocation density and evolution of GB volume for structures of 5nm grain size, which were equilibrated by the hybrid MD/MC scheme at different global compositions (15, 25 and 35 % Fe). The representative slices through the microstructure at a total strain of 10 % visualize, that no intergranular fracture occurred. Color coding is identical to Fig. 15.

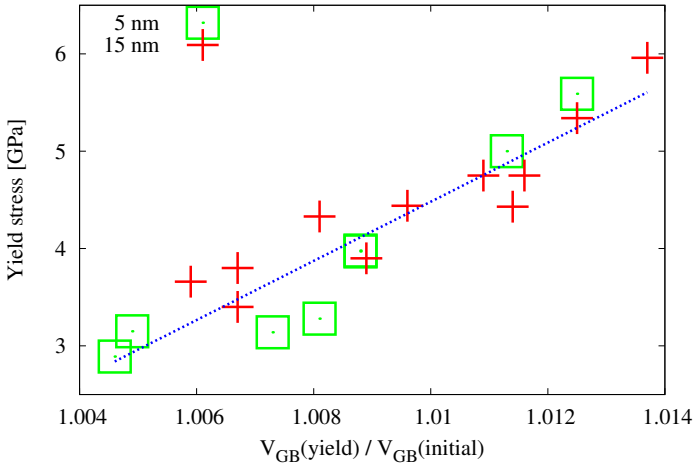

Figure 37: Correlation between yield stress (stress at plastic strain of 0.7 %) and the change in GB volume during deformation for 5 and 15 nm grain size and different states of relaxation. Open squares refer to the data for 5 nm grain size and crosses to the data for 15 nm grain size. (Also data for samples, which were not discussed in detail is shown here.)

the miscible systems (Sec. 6) and observations on materials where dislocation slip is completely inactive (ultrananocrystalline diamond), where it was observed, that the yield stress scales with the stress required for GB sliding [201].

9.4 DISCUSSION

Suppressing dislocation motion by leaving the grain interior in the energetically favored, ordered state resulted in a strong dependence on GB composition. For the 15 nm grain size, however, an ordered grain interior also leads to intergranular fracture. The processes in the GB can apparently not accommodate themselves for this grain size and dislocation activity is required to deform plastically. Ductility could here be conserved by increasing the volume fraction of the GBs, i.e. by a smaller grain size. For the 5 nm samples, we find no intergranular fracture during straining and a strong dependence of strength on GB composition. For the 5 nm grain size, where GB mediated processes contribute stronger to plastic deformation, the material stays ductile also for the case of ordered grains. Here, the macroscopic mechanical properties are controlled by the state of the GB only.

Part V

COUPLED MOTION VS. MESOSCOPIC SLIDING

After identifying the state of the GB and the GB mediated processes as the controlling parameters of the deformation in NC alloys in the preceding chapters, we will now discuss the delicate interplay between individual grain boundary processes.

For the case of stress coupled GB motion and mesoscopic GB sliding, it is explored, how they contribute to plastic deformation. Since mesoscopic GB sliding relies on the alignment of several neighboring GBs and stress coupled motion leads to the normal motion of a given GB, the two processes exclude each other or at least compete as potential deformation processes.

Here it is of interest to resolve, how the two processes contributes to room temperature deformation. Furthermore it needs to be understood, how the competition between the processes is affected by the presence of solutes in the GBs, since segregating solutes can affect both, stress coupled motion as well as GB sliding.

Therefore the following chapter discusses the competition between coupled GB motion and mesoscopic sliding in terms of their contribution to plastic deformation, the underlying atomistic processes and the way, they are influenced by different segregating solutes in the GBs.

10

STRESS COUPLED MOTION AND MESOSCOPIC SLIDING

Besides conventional dislocation activity, deformation modes in NC metals include GB sliding, grain rotation and normal GB motion (Sec. 1.3). It has been suggested that intergranular mechanisms can accommodate each other [202], which is decreasing the necessary amount of intragranular deformation as accommodation processes to ensure geometric compatibility.

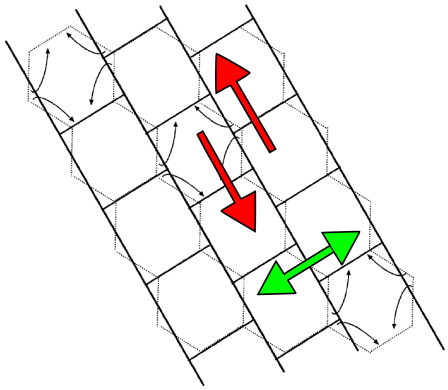

Figure 38: Schematics of aligned GBs in a microstructure. (On the basis of Materials Science and Engineering A **381**, 28 (2004), © 2004, with permission from Elsevier.) Red arrows indicate mesoscopic GB sliding along a subset of aligned GBs as described in Ref. [203, 204]; green arrows indicate stress coupled normal GB motion as described in [205, 202].

Furthermore, it was proposed that GB sliding can expand to a mesoscopic scale [203]. That is, neighboring grains can slide with respect to each other on distances typically exceeding the grain diameter (Fig. 38). This model was used to explain the observed deviation from the extrapolated Hall-Petch relation [206]. Microstructural evidence for the alignment of neighboring GBs is reported from experiments [207, 208] and simulation [209]. In general, the mechanism of mesoscopic GB sliding requires the alignment of neighboring GBs and the conservation of the orientation relation of adjacent grains throughout the course of deformation. Distinct from pure shearing, GBs can also contribute to plastic deformation by their normal motion [205, 78]. This normal motion of the GB can couple to a shear component and vice versa, where a non-zero degree of coupling has been determined for a variety of general GBs [202]. Evidence for coupled motion in NC microstructures is also reported from experiment and simulation [78, 38, 79, 210].

The magnitude of normal GB motion, however, depends on the orientation of opposing grains (the coupling factor of the resulting GB) and therefore varies along a mesoscopic slide plane consisting of grain boundaries of various types. Consequently, an alignment of GBs can also be destroyed by coupled motion as visualized in Fig. 38, where the two modes of deformation are indicated.

In this chapter, we use MD for investigating this problem. We perform a detailed analysis of the processes of deformation and the evolution of defects throughout straining and investigate the interplay of mesoscopic GB sliding and coupled GB motion.

10.1 DESIGN OF THE MICROSTRUCTURE

Padmanabhan et al. have suggested, that below a certain grain size in the lower nm range, boundary migration (and alignment) takes place entirely by diffusion [206, 211]. For the method used in the presented work, the time scales necessary for diffusion assisted GB migration are, however, not accessible. Thus, we started with specially designed microstructures shortcutting the process of initial alignment. To model bulk material, periodic boundary conditions were applied in all directions.

In order to investigate the influence of a potential mesoscopic slide plane on the mechanical properties, two distinctly different microstructures were prepared as described in Sec. 3.

In one case the positions of the grain centers were chosen such that a subset of the resulting GBs is aligned along a mesoscopic sliding plane which fully intercepts the microstructure (in accordance with periodic boundary conditions). The sliding plane is oriented under an angle of 45° with respect to the loading direction and therefore parallel to the direction of maximum resolved shear stress, favoring GB sliding within the plane. The structure consists of 24 grains of about 10 nm in diameter. The microstructure is expected to facilitate mesoscopic GB sliding due the presence of an appropriate sliding plane. This sample will be referred to as sample type A in the following, a slice through the initial microstructure is shown in Fig. 39.

In the second case, the grain centers were positioned on a fcc superlattice in order to obtain a unimodal size distribution. This structure is expected to show a high resistance against (mesoscopic) GB sliding, since any GB, which is oriented parallel to the direction of maximum resolved shear stress is aligned with grain centers of neighboring grains. GB sliding in this microstructure has therefore to be accommodated by a high amount of intragranular deformation in neighboring grains. The structure consists of 32 grains of about 10 nm in diameter. This sample will be referred to as sample type B in the following.

The orientation relation between neighboring grains (also along the potential sliding plane) was chosen at random, where low angle configurations were

suppressed. By studying multiple grain orientations (not shown) it was excluded, that the presented structure shows a singular behavior caused by the special arrangement of grain orientations.

Table 3: Different sample types and the description of the according microstructure

Type	**Microstructure**
A_{Pd}, A_{Cu} 	A subset of GBs is aligned along a potential sliding plane (see Fig. 39; the subscript denotes Pd and Cu, respectively).
B_{Pd}, B_{Cu} 	The grain centers are positioned on a fcc superlattice; the subscript denotes Pd and Cu, respectively.

Table 3 summarizes the different sample types and their respective microstructures described before.

After preparation and successive relaxation samples were deformed under uniaxial tensile and compressive load (as described in Sec. 2.5) at 300 K with a constant engineering strain rate (10^8 1/s). For distinguishing atoms located in GBs from atoms in the grain interior the CNA was used (Sec. 2.4.2). Extraction of dislocation structures from the atomistic data was done using DXA (Sec. 2.4.4).

10.2 STRESS-STRAIN BEHAVIOR AND DEFORMATION MECHANISMS

The observed stress-strain behavior for the two studied microstructures under tensile and compressive load is shown for Pd in Fig. 39. For the case of NC Cu (not shown) a similar trend is observed. Independent of the loading condition, the structure of type B exhibits a higher yield strength as compared to the structure of type A, where the mesoscopic slide plane offers an additional deformation path. In addition, the latter sample also shows a stronger tension-compression asymmetry than sample B having no mesoscopic slide planes. This trend is observed for both materials, Pd and Cu. The processes carrying plastic deformation in sample type A are therefore considered to be more sensitive to an applied pressure as compared to the processes being active in samples of type B. Most interestingly, samples of type A undergo a significant amount of strain hardening after yielding and approach the strength of samples of type B during the course of deformation. Close inspection of the microstructure and atomic displacements reveals, that samples of type A deform mainly via coupled GB motion and GB sliding. The contribution by the former destroys the initial alignment of the GBs, making sliding more difficult and therefore leads to the observed strain hardening. From the slices through the microstructure after 10% of strain (Fig. 39) it can be seen, that the subset of GBs which was aligned prior to deformation does not stay

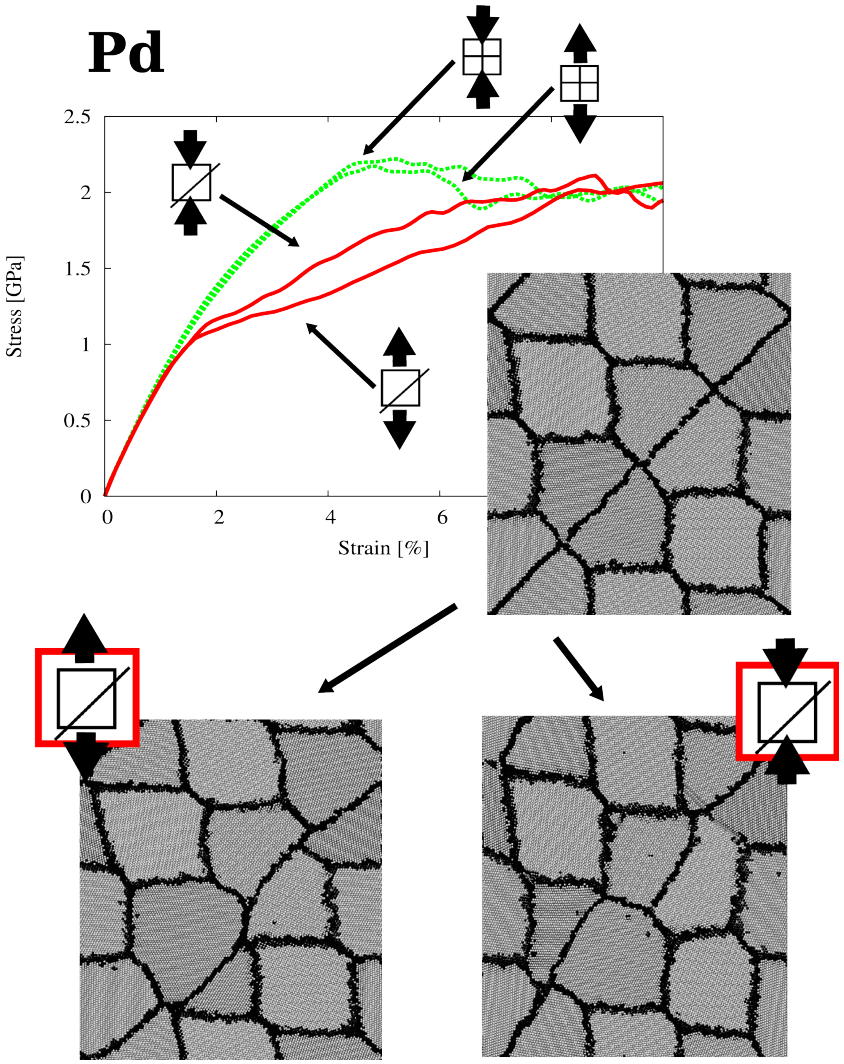

Figure 39: Microstructure and stress-strain behavior of nc Pd for different structures and loading conditions. The stress-strain behavior of sample type *A* under tension and compression is shown in red, solid line; the stress-strain behavior of sample type *B* is shown in green, dashed line. The upper slice shows the initial microstructure with an aligned subset of GBs (Type A). White denotes atoms in a fcc environment, black denotes atoms in a disturbed environment and grey denotes atoms adjacent to a stacking or twinning fault (according to CNA [152]). In the lower slices the structure of type A is shown after deformation under tensile (left) and compressive (right) load, respectively. (Structures are rescaled to initial dimensions to facilitate comparison.) Analysis and visualization was carried out, using OVITO [165].

aligned during the course of deformation. Several GBs move out of their initial position by normal motion. Comparing the microstructures for the two different loading conditions demonstrates that the normal motion must couple to the applied shear, since it reverses direction for a change in the loading direction. This finding demonstrates that coupled GB motion can hinder mesoscopic GB sliding by normal motion of neighboring GBs in opposite directions, which suppresses and/or destroys GB alignment. Since a wide range of GBs show coupled motion [202], this effect is expected to efficiently retard mesoscopic GB sliding in pure metals. Coupled GB motion therefore leads to the observed strengthening, where potentially aligned GBs are eliminated and a behavior similar to a structure with maximum resistance (sample type *B*) is observed.

10.3 MECHANISM OF STRESS COUPLED GRAIN BOUNDARY MOTION

For the case of symmetric tilt GBs atomic processes of coupled motion and the according coupling factors were analyzed in detail by Cahn et al. by atomistic bicrystal simulations [202]. Velasco et al. [210] integrated one GB, for which the occurrence of normal motion was reported from bicrystal simulations [109], into a 3-dim. NC microstructure and found also evidence for coupled motion. The reported coupling factor of the integrated GB was comparable to the one reported from the bicrystal simulations.

For the microstructure studied here, the coupling factor of a particular GB was estimated from the motion of marker lines during deformation (Fig. 40). For the examined GB, which moves by normal motion during straining, the misorientation angle is 33 ° but of general type with a (nonsymmetric) tilt and a twist component. Most interestingly, the estimated coupling factor of 0.5 is close to the value of 0.6 reported for a symmetric tilt GB ($\Sigma 53(720)$) with a misorientation angle of 32 ° by Cahn et al. [202] and is similar for the two studied materials. Given the differing character of the GB, where only the tilt component of the boundary is expected to lead to normal motion [212] and the observed non-planarity, which complicates an exact measure of the coupling factor, this is in fair agreement with the findings by Velasco et al. [210]. The result shows that the coupling of a GB is not severely hindered by the presence of triple lines and quadruple junctions.

For analyzing the precise nature of coupling in a 3-dim. microstructure the position of two test areas in the GB was tracked over time during the course of deformation at 300 K and 50 K temperature. The results for a test area of 9 and 49 nm^2 are shown in Fig. 41, respectively, together with the data for the low temperature deformation. It can be seen, that, irrespective of the applied temperature, the magnitude of normal motion is similar for all datasets. Furthermore, the movement of the GB occurs in a stick-slip fashion, which is as well consistent with the data for the symmetric tilt GBs reported by Cahn et al. [202] from bicrystal simulations and results from experiments, where a stick-slip movement

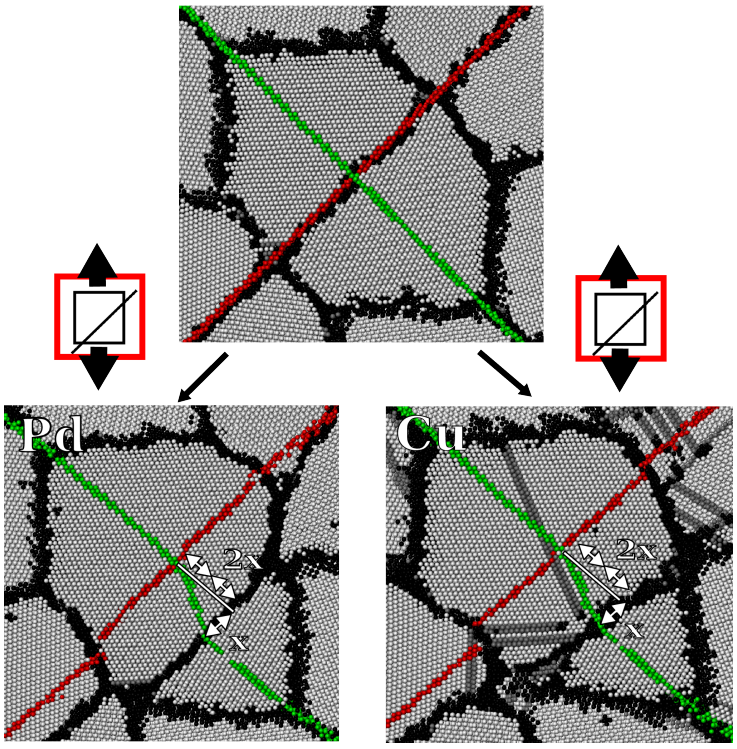

Figure 40: Coupled GB motion: Example of a GB with a misorientation angle of about 33° which moves by coupled motion for the two studied pure metals, Cu and Pd. The upper snapshot shows the initial configuration, the lower snapshot shows the same slice of the microstructure at 10 % total strain. Marker lines are introduced to facilitate analysis. They are labeling the atoms (initially) aligned with the potential mesoscopic slide plane and perpendicular to it, respectively. From the evolution of the position of the marker lines during straining, a coupling factor of 0.5 can be estimated.

of GBs was observed by in-situ HREM [213]. The observed characteristic length scale of normal GB motion, $\Delta r \approx 0.2$ nm (Fig. 41) is again of similar size as the characteristic increments of normal GB displacement reported for the bicrystals [202]. This characteristic increment is similar to the NN distance in the direction of motion of the GB as visualized in Fig. 41. The stick-slip behavior is more pronounced for smaller test areas of the GB, indicating that the normal motion of the GB is not happening uniformly over a large area but rather occurring through the successive movements of small fractions as suggested by Cahn et al. [202]. By varying the size of the test area, the critical nucleus size, i.e. the fraction of the GB which appears to move uniformly was estimated to be in the order of 10 nm^2. The atomistic processes, leading to normal motion of general GBs within a microstructure can therefore be considered to be very similar to the case of symmetric tilt GBs reported for bicrystals [202]. A characteristic structural unit could, however, not be identified for the presented case. From the configuration of the GB at various stages of deformation (Fig. 41) different potential constraints which might hinder normal motion can be observed. They range from disconnections in the GB (which are also discussed for the bicrystals [202]) to atomic clusters, which need to be rearranged.

From experiments on bicrystals it was reported, that coupled motion of a GB of general character can lead to the rotation of neighboring grains versus each other [212] and it was argued, that the coupling factor remains unchanged being dependent on the tilt component only, while the rotation couples to the twist component of the GB. For the presented GB, no rotation of the grains versus each other was observed. This might, however, be due to the constraints imposed by the surrounding microstructure, suppressing grain rotation at the imposed strain rate and temperature.

10.4 DISCUSSION

For the case of the pure metals, the presence of a mesoscopic sliding plane decreases the yield strength of the material for tensile and compressive deformation. This is confirmed by comparison with a reference structures, where grain centers were positioned on a superlattice and thus present a case with maximum resistance to mesoscopic GB sliding. For both studied materials (Cu and Pd), the mesoscopic slide plane is destroyed during the course of deformation. This occurs by stress coupled GB motion showing a reversed direction of the normal GB motion under a reversed resolved shear stress. Coupled GB motion therefore contributes to room temperature deformation in the presented NC microstructure. It furthermore suppresses mesoscopic GB sliding, since it destroys the major prerequisite, an aligned subset of neighboring GBs. This occurs only if neighboring GBs have a differing coupling factor. Since neighboring GBs are expected to have a random orientation relation and the coupling factor varies significantly

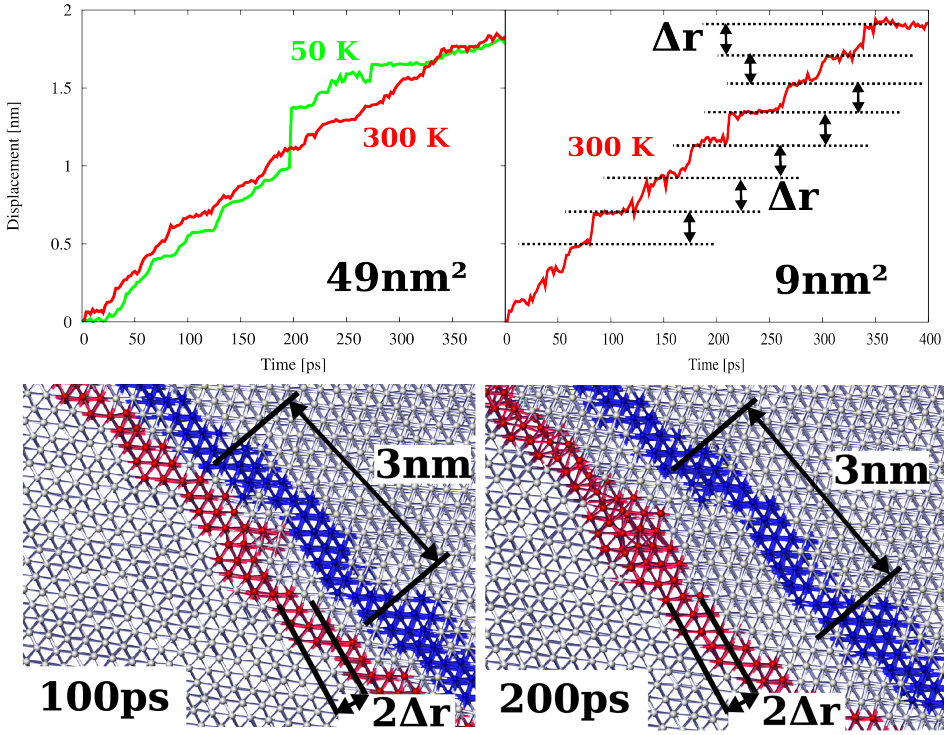

Figure 41: Upper line: Displacement as a function of time for one GB moving by normal motion in pure nc Cu. The data for a sample area of 49 and 9 nm^2, respectively of the same GB is shown. For the case of a sample area of 49 nm^2, data for straining at 50 K is also included. Lower line: Slices through the atomistic configuration of the selected GB at different time steps, where the GB is pinned and has to overcome configurational barriers. The initial position of the GB is indicated in blue, the GB configuration at the according time step is indicated in red. To facilitate comparison, the characteristic length scale of the stick-slip displacement and the lateral length of the smaller sample area are also included.

with the character of the GB [202], a random distribution of coupling factors for neighboring GBs is conceivable. The development of mesoscopic sliding as room temperature deformation mechanism in NC microstructures is therefore significantly hindered by coupled GB motion. Concerning the precise nature of coupled motion, we find that characteristic coupling factor and the stick-slip fashion of normal motion are in good agreement with results of GBs in a bicrystal of similar misorientation. We furthermore find that GBs do not move uniformly and planar, but fractionwise, where the characteristic size for one example was estimated to be in the order of 10 nm^2. The observed mechanisms are not specific to the studied material (NC Pd and NC Cu), but can be expected to be operational in all polycrystalline metals, where GB motion contributes to plastic deformation and there maybe hereto overlooked situations where stress-driven GB motion influences the mechanical response and microstructure stability [9].

11

THE EFFECT OF SEGREGATING SOLUTES

Mesoscopic GB sliding and coupled GB motion can hardly coexist as discussed in the previous chapter (Sec. 10). The former requires an alignment of GBs during deformation while the latter destroys any potential GB alignment by normal motion. The interplay between the two distinct modes of GB mediated plasticity is, however, complicated by the presence of solutes. Located in the vicinity of the GB solutes can prevent both, normal GB motion as well as GB sliding [108, 109, 110]. It was shown experimentally and by simulations that solutes can hinder normal GB motion [110, 112] and increase the necessary stress for coupled GB motion [113, 109]. Additionally, it was observed that segregated solutes can increase the resistance of GB with respect to sliding mechanisms [108]. The balance between these two competing modes of deformation in the presence of solutes and impurities is discussed in this section.

11.1 DESIGN OF THE MICROSTRUCTURE

In order to study the influence of segregating solutes on the interplay between coupled GB motion and mesoscopic GB sliding, identical microstructures as in the previous chapter (Sec. 10) were used. For the microstructure of type A (with a mesoscopic slide plane), two different ways of introducing solutes (Sec. 3) into the NC Cu microstructure were compared. Table 4 summarizes the different sample types. For the samples of type $CuNb_{rand}$ and $CuFe_{rand}$, atoms located in the GBs (according to CNA [152]) were chosen at random and their chemical identity was changed to Nb or Fe, respectively prior to relaxation. Afterwards structural relaxation by MD was carried out at 600 K for 1 ns at zero hydrostatic pressure following the same procedure as for the pure material. Slices through the initial microstructure of type $CuNb_{rand}$ are shown in Fig. 42, for type $CuFe_{rand}$ in Fig. 44.

For another set of samples, the hybrid MD/MC scheme (Sec. 2.3) was utilized for introducing the solute atoms. Here, relaxation and alloying was performed simultaneously at 600 K for 1 ns at zero hydrostatic pressure, where the temperature parameter for the Metropolis MC algorithm was also set to 600 K. The resulting

Table 4: Different sample types and the description of the according microstructure

Type	Microstructure
$CuNb_{rand}$ 	Identical to A_{Cu} but with a fraction of atoms in the GB having their chemical identity changed to Nb prior to equilibration (see text, Fig. 42).
$CuNb_{MC}$ 	Identical to $CuNb_{rand}$ but using hybrid MD/MC to introduce the Nb atoms into the GB and allow for structural relaxation (see text, Fig. 43).
$CuFe_{rand}$ 	Identical to A_{Cu} but with a fraction of atoms in the GB having their chemical identity changed to Fe prior to equilibration (see text, Fig. 44).

structures will be referred to as sample type $CuNb_{MC}$ in the following and slices through the initial microstructure can be seen in Fig. 43.

11.2 SEGREGATING SOLUTES - GRAIN BOUNDARY PINNING

In Fig. 42, the stress-strain behavior for sample type $CuNb_{rand}$ with 3 and 6 % of Nb in the GBs, respectively, is shown. It can be seen, how solutes increase the strength of the microstructure, where a higher concentration leads to a stronger increase. Depending on the composition, the solutes suppress coupled motion and pin the mesoscopic sliding plane. For the highest amount of solutes (6% of the GB atoms), the microstructure can deform mainly by mesoscopic GB sliding along the aligned GBs, which are locked in place by the dopants. In addition to the suppression of normal GB motion, a lower amount of stacking faults as compared to pure Cu is observed. This is consistent with the expectations, since in the case of Cu with 6% of Nb in the GBs, the microstructure can deform mainly by mesoscopic GB sliding while for the case of pure Cu the potential sliding plane is destroyed. If the GB alignment is destroyed, GB sliding has to be accommodated either by normal GB motion or dislocation slip where the slip of leading partial dislocations leads to the formation of stacking faults. For the intermediate composition (3% of Nb in the GBs), the solutes also affect the normal motion of the GBs and increase the strength of the microstructure. They do, however, not efficiently pin the GB, which still moves by coupled motion and leaves the solutes behind in the matrix (Fig. 42). Once the GBs break free from the solutes, the microstructure deforms by GB sliding accommodated by coupled motion and/or dislocation slip. From close inspection of the microstructure it can be seen that the presence of solutes decreases the amount of normal motion for the same total strain as compared to pure Cu.

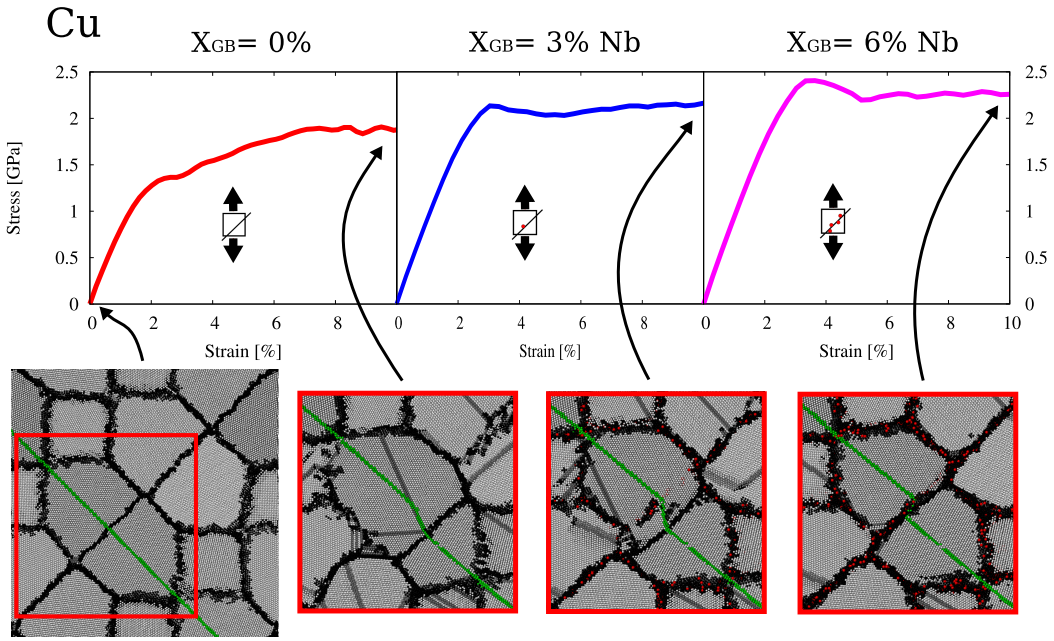

Figure 42: Initial microstructure and the stress-strain behavior for pure Cu (red) and the case of 3% and 6% of Nb atoms in the GBs (blue and pink, respectively) with the respective microstructures after deformation. Color coding for the microstructures is such that white atoms belong to the grain interior, black atoms to the GB and gray atoms are neighboring a stacking or twinning fault (according to CNA [152]). Solutes are enlarged and highlighted in red. A marker plane is introduced to facilitate comparison, which labels a subset of atoms perfectly aligned prior to deformation (green). Analysis and visualization was carried out, using OVITO [165]

The evolution of the dislocation density during deformation is shown in Fig. 43. During the course of deformation the dislocation density rises significantly for the case of pure Cu (sample type A_{Cu}). This can be explained by the evolution of the microstructure, where the initial GB alignment is destroyed by normal motion and deformation has also to be accommodated by intragranular processes. For the case of the alloyed structures the increase in dislocation density during deformation is less pronounced and almost vanishes for the case of 6% of Nb in the GBs (sample type $CuNb_{rand}$). For that case coupled GB motion is completely suppressed and the structure can deform by mesoscopic GB sliding. This explains the reduced increase in dislocation density, since intragranular deformation as a accommodation process is barely necessary. For the case of the lower concentration of solutes (3% of GB atoms), a slightly stronger increase in dislocation density is observed, since some segments of the mesoscopic slide plane still move by coupled motion (Fig. 42) and thus make dislocation activity necessary as accommodating mechanics.

In summary, segregating solutes have a strengthening effect on NC structures. Their presence in the GBs hinders both, sliding and coupled motion, resulting in an overall increased strength of the material. If the concentration of solutes is sufficiently high, coupled GB motion can be suppressed completely. A potentially aligned subset of GBs can then slide also on a mesoscopic scale and stay aligned even during room temperature deformation.

11.3 ROLE OF GRAIN BOUNDARY RELAXATION STATE

Chemical and structural GB equilibration can drastically increase the strength of NC alloys by reducing the GB energy i.e. the free volume in the GBs (Sec. 6, Sec. 7) [29]. In an additional step, solutes were introduced by employing the hybrid MD/MC algorithm (Sec. 11.1) leading to densely packed GB structures. A slice through the initial microstructure of sample type $CuNb_{MC}$ is shown in Fig. 43, where the solute distribution is not as homogeneous as in the case of a random distribution (as observed in sample type $CuNb_{rand}$). Depending on the type and misorientation of a particular GB, the introduction of solutes is facilitated or suppressed. The average composition of the GBs is, however for the presented case 7% and therefore similar to the sample with a random solute distribution and and GB concentration of 6%. In Fig. 43, the stress-strain behavior of the structure is shown. Structure $CuNb_{MC}$ has a drastically increased yield strength as compared to the structures with a random distribution (sample type $CuNb_{rand}$), which is due to the fact that GB mediated processes are suppressed by the reduction of free volume in the GB (Sec. 7).

After yielding a softening of the material is observed, which was also found for miscible and immiscible systems with a well equilibrated GB (Sec. 6, Sec. 7), and can be explained with structural changes within the GB during the course

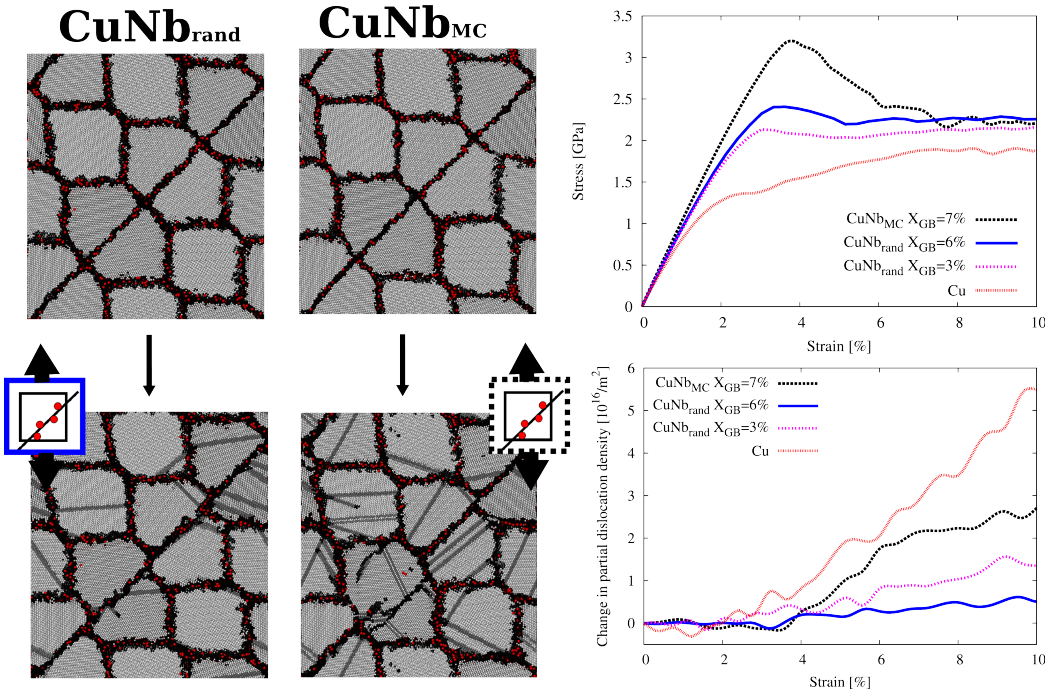

Figure 43: Microstructure, stress-strain behavior and change in dislocation density for NC Cu–Nb. Upper Left: Slices through the initial microstructures of type $CuNb_{rand}$ and $CuNb_{MC}$. Nb atoms are enlarged and highlighted in red. Lower left: Slices through the microstructures after 10% of tensile deformation for the two cases. Right: Stress-strain behavior and according change in dislocation density for NC Cu–Nb. Sample type $CuNb_{rand}$ with 3% and 6% of Nb in the GB is shown in pink and blue, respectively. The data for sample type $CuNb_{MC}$ (7% of Nb in the GB) and pure Cu is shown in black and red, respectively.

of deformation. The increase in dislocation density is clearly stronger than for the case of a random solute distribution. This means that the contribution by intragranular defects to the overall deformation is increased as compared to the structure of type $CuNb_{rand}$. Equilibrating the solute distribution by a hybrid MD/MC scheme allows to distribute the impurities to energetically favored positions and reduce the free volume in the GBs at the same time. This not only suppresses coupled GB motion as for the case of a random solute distribution and hinders GB sliding, it also strengthens the GBs in such a manner, that despite the presence of a mesoscopic sliding plane, dislocation nucleation and motion contributes more significantly to plastic deformation. This is how NC Cu doped with segregating solutes can approach the theoretical strength of the material (Sec. 7). It shall be noted, however, that coupled motion of GBs is not completely suppressed for the case of this distribution of solutes. It can be seen from the slices through the deformed microstructure (Fig. 43) that one GB still moves by coupled motion, leaving the initially segregated solutes in the interior of the growing grain. Most interestingly, the amount of observed coupled motion is similar to the case of structure type $CuNb_{rand}$ with 3% of Nb in the GBs. Additionally, it was observed that the GB, which still moves by coupled motion for the case of structure type $CuNb_{MC}$, has a GB concentration of about 3% Nb. This particular GB has therefore less favorable sites for the introduction of solutes leading to a reduced concentration for the case of alloying by the MD/MC scheme and therefore coupled GB motion is more likely.

11.4 TRANSFERABILITY TO DIFFERENT SEGREGATING SOLUTES

For studying the influence of the particular solute, also samples of Cu–Fe were studied. Since Fe has a small atomic size mismatch as compared to Cu, GB sliding should not be strongly affected by the equisized substitutional solutes, as reported by Millett et al. [108]. Coupled GB motion on the other hand should still be hindered by the presence of solutes, mainly caused by the positive heat of mixing. As described in (Sec. 11.1) different amounts of iron were introduced randomly into the GB. Consequently, the structures are referred to as sample type $CuFe_{rand}$. As compared to Cu–Nb higher amounts of solutes were introduced into the GB to observe a change in the mechanical response of the structure.

Regarding the yield point of the samples the trends are the same as observed for Cu–Nb. As the concentration of solutes is increased, the yield stress of the material also increases. This is consistent with expectations based on the reported findings, where solutes hinder the coupled motion of the GBs, increasing the necessary stress for their normal motion. After yielding the difference between the pure metal and the alloyed structure decreases for the case of Cu–Fe. This is different from the case of Cu–Nb, but still in agreement with the reported observations, since the structure here mainly deforms by GB sliding accommo-

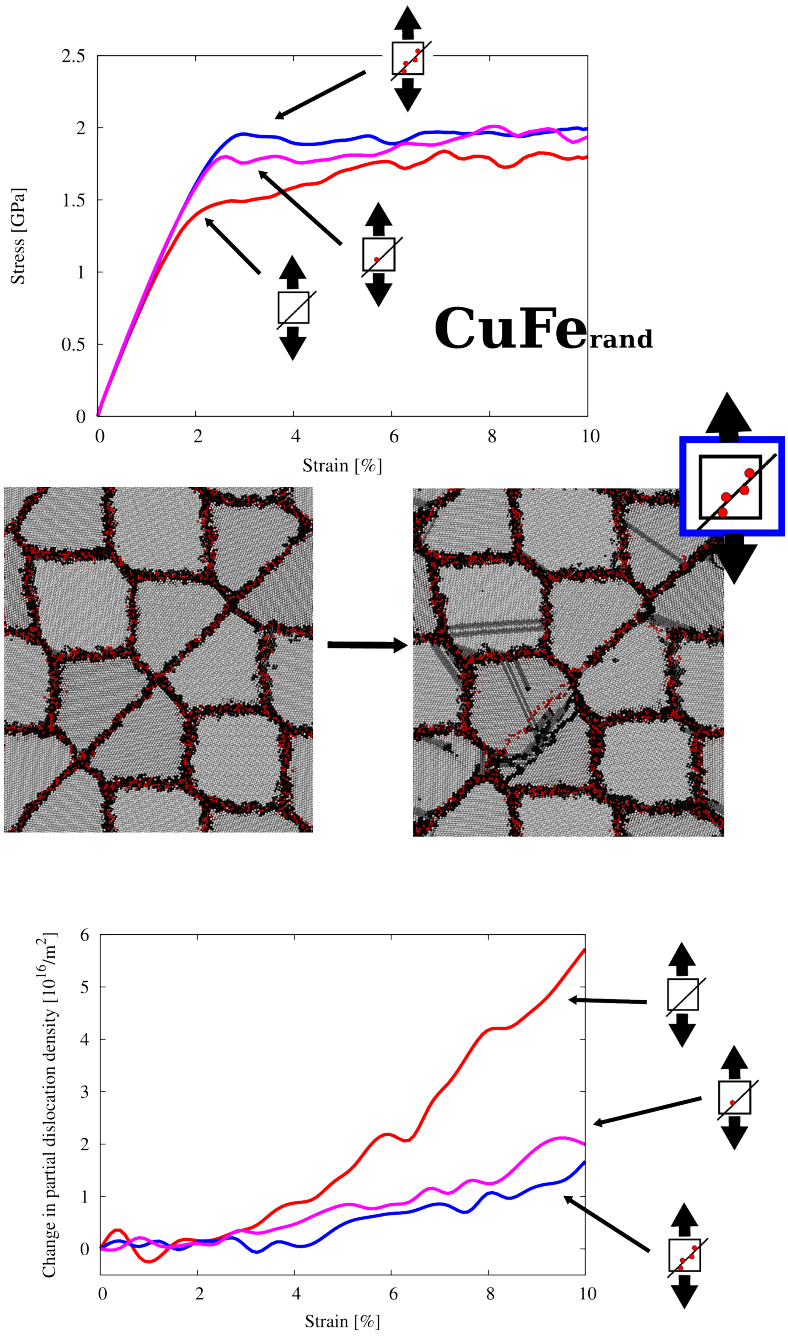

Figure 44: Top: Stress-strain behavior for sample Type $CuFe_{rand}$ with two different amounts of solutes. Pink and Blue denote 13% and 24% of Fe in the GB, respectively. To facilitate comparison, the data for pure Cu (red) is also shown. Middle: Slices through the microstructures of sample Type $CuFe_{rand}$ before straining and after 10% of tensile deformation, respectively (Fe atoms are highlighted in red). Bottom: Change in partial dislocation density as a function of strain for sample Type $CuFe_{rand}$ with 0%, 13% and 24% of Fe in the GB, respectively.

dated by dislocation slip and coupled GB motion (within the pure material), which is less affected by equisized substitutional solutes. The evolution of defects within the grain interior supports this picture. Here, the change in dislocation density is smaller for the case of the alloyed structures, which is consistent with the pinning of GBs and an increased contribution to plastic deformation by GB sliding. As the structures are deformed, the defect density also within the alloyed structures raises, showing the necessity for accommodating processes caused by the destruction of the mesoscopic slide plane. From the slices through the microstructure (Fig. 44) it can be observed, that also for the highest amount of Fe introduced into the GB (24% of the GB atoms) normal motion is observed. Here, one GB with a high coupling factor (the one reported in Sec. 10.3) breaks free from the pinning effect of the solutes and propagates via coupled motion. The introduced (equisized) solutes are left behind in the matrix, where they occupy perfect lattice positions. The hindering effect of solutes on the GB propagation by normal motion therefore drastically depends on the type and mismatch of segregating solutes in the GB.

11.5 DISCUSSION

Segregating solutes can alter the balance between normal GB motion and mesoscopic GB sliding as competing deformation mechanisms. For the case of NC Cu, the presence of Nb impurities in the GB resulted in an increased resistance to coupled GB motion and a drastically raised yield strength. Depending on the concentration of impurities, coupled motion can be suppressed completely and GB sliding can develop to a mesoscopic scale. Stabilization of potential GB alignments does not need to be caused by knowingly introduced solutes, but can also be due to segregating impurities picked up during sample preparation. Crucial for the contribution by GB mediated processes in general is, however, the degree of GB equilibration and the related amount of free volume in the GBs. Here, a reduced free volume in the GBs (as obtained by relaxation via the hybrid MD/MC scheme) can increase the structural stability of the GBs, approaching the theoretical strength of the material (Sec. 7) and leads to a stronger contribution by intragranular defects to the overall deformation. The measured dislocation density does (in general) not allow for conclusions on the contribution by dislocations to crystal deformation since it is solely controlled by the distance covered by mobile dislocations. For the present case, where all initial dislocations are located in the GBs and mostly immobile, an increase in dislocation density is caused by a nucleation of a (partial) dislocation into the otherwise defect-free grain interior. Since initially no obstacles inside the grains are present prior to deformation, an increased dislocation density resembles an increased contribution to deformation by dislocation slip. For the dislocation densities, we find a drastically decreasing slope in the change of dislocation density as the concentration of impurities in the

GBs is raised. This can be explained with the pinned GBs allowing for deformation solely by mesoscopic GB sliding, which does not need to be accommodated by intragranular slip.

The pinning force of solutes mainly depends on their atomic size mismatch, where a large mismatch refers to a large pinning force. A comparable high amount of equisized solutes (Fe in Cu) could not suppress coupled motion completely and equisized solutes are therefore less efficient in pinning the GBs in place.

We conclude that segregating solutes and their distribution in the GBs not only alters the balance between coupled GB motion and mesoscopic GB sliding as room temperature deformation mechanisms, their precise distribution also triggers the contribution by intragranular defects in a sensible manner.

Part VI

HIERARCHY OF DEFORMATION PROCESSES

The results by conventional MD straining simulations are influenced by the high strain rates adherent to this simulations. Improved simulation techniques may allow to overcome this limitations.

The following part deals with hybrid MD/MC straining simulations. Here, the MC scheme allows for local relaxation by the exchange of atomic species, shortcutting diffusional processes.

The effect on the macroscopic behavior is investigated and the implications on the interpretation of conventional MD simulations and their comparison to experiments is discussed.

12

ON THE HIERARCHY OF DEFORMATION PROCESSES

In MD simulations the typical deformation strain rates are significantly higher than in conventional experimental setups [180]. The hierarchy between different deformation mechanisms with individual activation enthalpies and activation volumes is therefore affected by the applied strain rate [22, 84] and transferring insights from simulations to experimental conditions is not directly possible [60, 180].

In the past, several approaches have been made [214] to boost the speed of atomistic simulations of stress-driven processes by coarse-graining atomic vibrations [215]. Atomic-strain-based adaptive hyperdynamics [216] or combinations of MD and MC methods [217, 218, 219] have been used in this context. Also, the kinetics of selected thermally activated processes were evaluated independently with transition state theory [220]. These attempts are, however, mostly limited to small structures, simplified geometries and single-component systems.

The influence of solutes, commonly present in experimental samples (often in unknown concentrations), has rarely been considered in atomistic simulations [6, 51]. Additions of solutes, can, however, influence the mechanical response of nc metals significantly (Sec. 13), [67]. In the following, the time scale problem inherent in MD is overcome by applying the hybrid ND/MC scheme, which brings the system towards equilibrium by swapping atomic species [106].

12.1 METHODOLOGY

We employ the hybrid MD/MC scheme described in Sec. 2.3 during straining. This allows for local chemical and structural relaxation by shortcutting diffusional processes. The frequency between local relaxation and the imposed straining is modulated. Thus, the balance between competing processes with a differing dependence on local relaxation can be altered and its effect on the macroscopic behavior can be studied. The scheme is applied to a NC Pd–Au 50% alloy, where deformation under tensile load is studied for various conditions. The NC model structures are identical to the ones discussed above (Sec. 6), where the elemental distribution for the completely miscible Pd–Au system was found to be not homogeneous and a depletion in Au is observed in the GBs (Sec. 4).

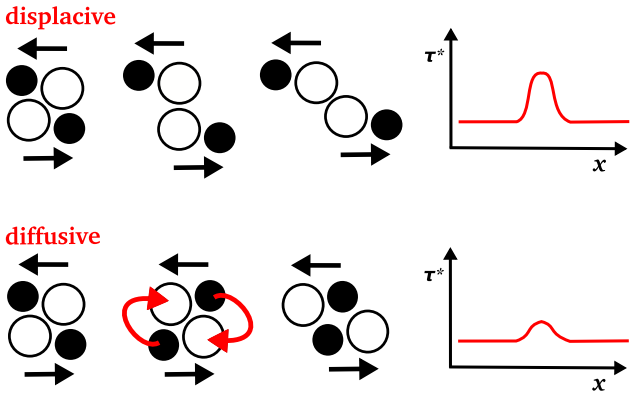

Figure 45: Schematic of processes in the GB under an applied shear stress. The upper line shows solely displacive atomic motion, where atoms need to overcome a substantial barrier to move past each other resulting in a high necessary resolved shear stress τ^*. The lower line visualizes, how diffusive processes can alter local barriers by an exchange of atoms, reducing the necessary resolved shear stress for the displacement.

The contribution of dislocation slip events to the overall deformation was analyzed, using the method by Stukowski and Arsenlis (Sec. 2.4.5, [159]).

Samples are deformed at 300 K by imposing a constant engineering strain rate (10^8 1/s) in uniaxial direction on the simulation cell.

During straining the hybrid MD/MC scheme is employed. Coupling to an external reservoir through the semi-grandcanonical MC scheme allows for atomic exchanges without accounting for the explicit exchange mechanisms but leads to a redistribution of the solute atoms and thus to a local relaxation. Fig. 45 shows schematically, how atomic exchanges may locally facilitate the relative shearing of atoms. Applying the MC scheme during straining is therefore expected to alter the barriers for displacive processes. The control parameter for the MC scheme, namely the difference in chemical potentials $\Delta\mu$, is identical to the one during the initial annealing for all simulations. Additionally, the variance control [145] is used to fix the global composition of the structure to the composition after initial alloying (50 % of Au).

The balance between MD steps (imposing the tensile straining) and local relaxation by MC steps is varied either by modifying the swap fraction or by modifying ΔMD. The swap fraction is the fraction of the atoms in the system, on which trial exchanges are carried out during one MC step and ΔMD is the number of MD steps between two successive MC steps.

Table 5 summarizes the various testing conditions and introduces the corresponding labels.

Table 5: Tensile testing conditions and the according labels. Swap fraction denotes the fraction of atoms in the system which are treated during one step by the MC algorithm. ΔMD is the number of MD steps, carried out between two successive (partial) MC steps (see text).

Label	**Swap fraction**	**ΔMD**	**Brief description**
noMC	-	-	No MC is carried out during straining.
1.0	1.0	10	Every 10 MD steps, MC is carried out on all atoms.
0.1	0.1	10	Every 10 MD steps, MC is carried out on 10 % of the atoms.
0.01	0.01	10	Every 10 MD steps, MC is carried out on 1 % of the atoms.
0.001	0.001	10	Every 10 MD steps, MC is carried out on 0.1 % of the atoms.
1.0<->0.1	1.0 or 0.1	10	Alternating swap fraction between 1.0 and 0.1.
0.1<->0.01	0.1 or 0.01	10	Alternating swap fraction between 0.1 and 0.01.
ΔMD 1000	1.0	1000	Every 1000 MD steps, MC is carried out on all atoms.
ΔMD 10000	1.0	10000	Every 10000 MD steps, MC is carried out on all atoms.

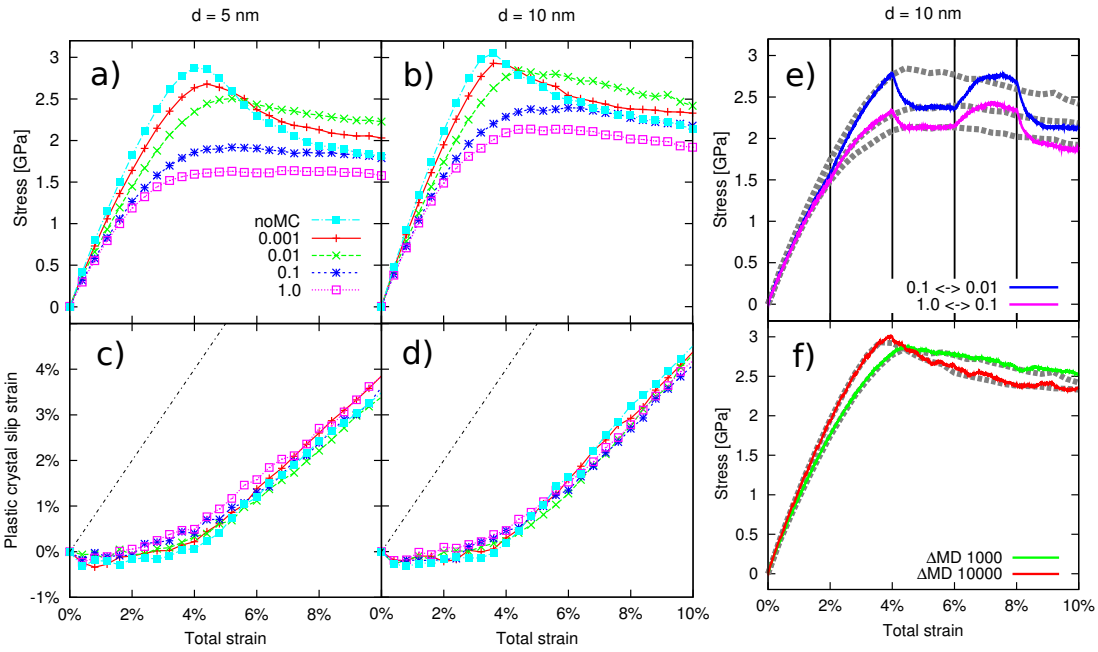

Figure 46: a-d): Stress-strain behavior and plastic crystal slip strain of NC Pd–Au 50% for various testing conditions and two different grain sizes, where a) and c) show the 5 nm case and b) and d) show the data for the 10 nm grain size. The crystal slip strain is measured for the structures under the applied load. e): Stress-strain behavior for the case of an alternating MC swap fraction (the swap fraction is changed at constant time intervals as indicated by the vertical black lines) for the 10 nm grain size. In dashed grey, the reference data is shown, where the swap fraction was not changed during straining (same data as in b)). f): Stress-strain behavior during straining with an altered number of MD steps between two successive MC steps (ΔMD). Reference data (dashed, grey) is shown which corresponds to the cases of an identical time interval for one full MC step obtained by a change in the swap fraction (same data as in b)).

12.2 STRESS-STRAIN BEHAVIOR AND CRYSTAL SLIP

The stress-strain behavior for structures of 5 and 10 nm grain size with 50 % of Au tested at various deformation conditions is shown in Fig. 46 a) and b). Independent of the grain size, the slope in the elastic regime is larger for the samples where no MC is carried out during straining and the lowest for the structures, where the local relaxation occurs with the highest frequency. Also, the yield stress shows a clear dependence on the straining conditions. Here, a similar trend is observed. The yield stress shows the highest value for the case of conventional MD (noMC), whereas an increased frequency of local relaxation leads to a drastic decrease in yield strength. Regarding the occurrence of an overshoot in the stress-strain behavior, which is often explained by the ultra-high strain rates in MD simulations [54], it can be seen that local relaxation by MC trial exchanges drastically reduces the amount of overshooting. For the highest MC rates, the overshoot even vanishes completely.

The structures were analyzed at different straining stages with respect to the initial structure and the contribution by dislocation slip was extracted. Fig. 46 c) and d) show that there is no detectable difference in the contribution by crystal slip for the various testing conditions. The dislocation activity for a given total strain must therefore be similar and independent of the local relaxation. The relationship between the total strain and the irreversible plastic strain, however, delicately depends on the deformation conditions as will be discussed in the following section. Comparing the data for the different studied grain sizes, it can be seen that the contribution by dislocation slip is slightly increased for the 10 nm structures as compared to the 5 nm grain size. It shall be noted, that the analysis algorithm detects not only dislocation slip in the grain interior but also movement of dislocation networks (low angle GBs) and the movement of twinning dislocations on twin boundaries as plastic crystal slip. This might complicate the comparison with respect to grain size, since a larger fraction of twin boundaries is observed after annealing for the 5 nm structures (not shown).

In a next step jump test were carried out, where the balance between MD steps and local relaxation by MC trial exchanges was varied during straining to test the influence of straining history of the sample. Fig. 46 e) shows the stress-strain behavior for two cases, where the swap fraction was altered between two values within constant time intervals (as indicated by vertical black lines). As a reference, the data for the cases, where the swap fraction was constant during straining, is also shown (dashed, grey). Evidently, altering the balance between MD straining and local relaxation affects the deformation properties, independent of the straining stage. The results furthermore show that after a short time, the system reaches a steady-state deformation regime independent of the straining history of the sample.

Fig. 46 f) shows, how the results are affected by the time constant for coupling to the external reservoir. Different ways to modify the balance between straining and

local relaxation are compared. Results of simulations, where ΔMD was altered, are compared with data, where ΔMD was kept constant but the swap fraction was changed to obtain an identical time interval until one exchange attempt is carried out on every atom in the system on average. The data with a modified ΔMD is shown as colored solid lines, whereas the reference data with a modified swap fraction (same data as in Fig. 46 b)) is shown as dashed, grey lines. Interestingly, the results are independent of the time constant for the coupling to the external reservoir, if the time interval to carry out one exchange attempt on average on every atom in the system is unchanged. The response of the system is therefore similar, regardless whether local relaxation is carried out frequently on a small fraction of atoms or less frequent on all atoms as long as the overall rate stays the same.

12.2.1 *Reversibility*

Close inspection of the microstructure after unloading revealed that several contributions to plastic deformation are reversible. This is most pronounced for the case, where no MC is carried out during straining. Fig. 47 a) shows how the microstructure changes during loading. Here, the color coding according to the displacement from the initial position reveals some grain movement as well as partial dislocation motion and the nucleation of a twin embryo (detectable by discontinuities in the color scheme and stacking faults). When the structure is unloaded and relaxed after deformation to a total strain of 4 %, most of the displacement is reversed. Most surprisingly, also partial dislocations, which fully intercepted the grain interior and were absorbed by the opposing GB reverse their motion. This leads to an annealing of stacking faults, twin embryos and therefore to a negligible irreversible plastic strain. For the case with the highest frequency of local relaxation during straining on the contrary (Fig. 47 b)), we find less reversibility after unloading. Here, less displacement during loading and no dislocation activity for this part of the microstructure during the initial stages of straining is observed. The displacement which occurs (mostly in the vicinity of the GB), however, does not disappear after unloading.

In a next step, we unloaded the structures at various straining states and quantified the amount of irreversible plastic deformation to further investigate the ratio between reversible and irreversible strain. Fig. 48 shows the total irreversible strain after unloading as a function of the total strain for the various testing conditions. Obviously, irreversible straining occurs much earlier for the cases, where local relaxation is facilitated by the MC trial exchanges. Most interestingly, for the case of straining by conventional MD, the deformation of the material is fully reversible up to a total strain of about 5 and 4 % for the 5 and 10 nm structures, respectively. As can be seen from the snapshots (Fig. 47) and the evolution of plastic crystal slip (Fig. 46) this is not caused by a fully elastic

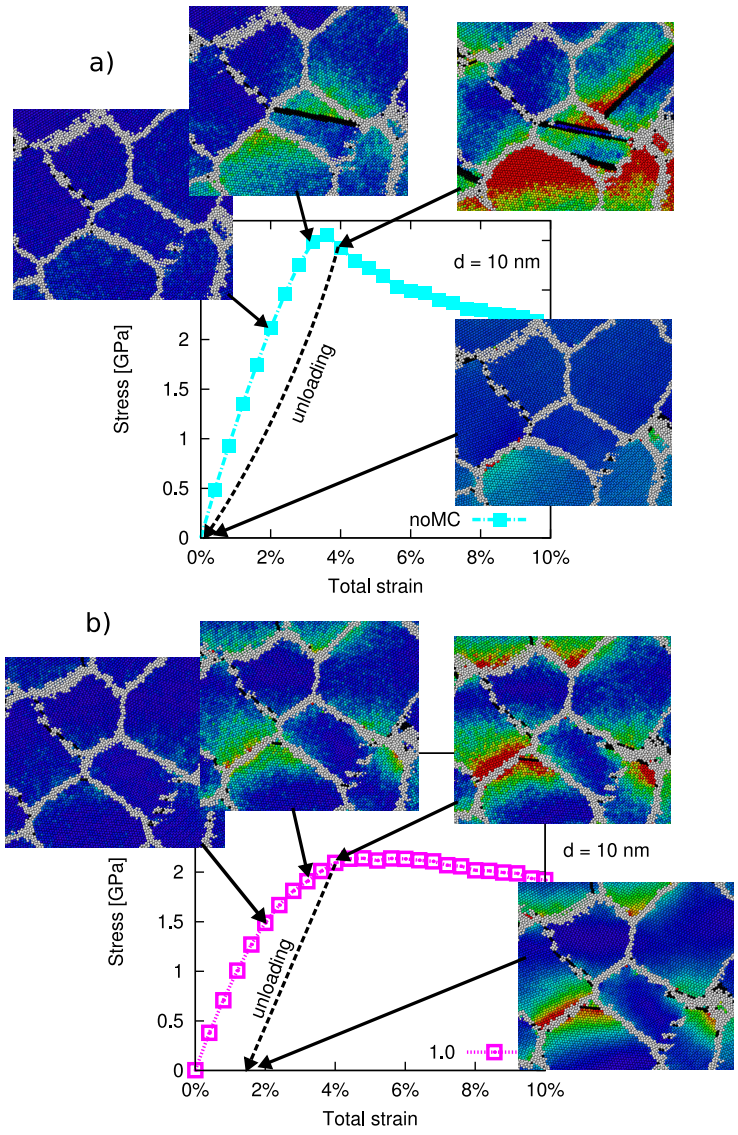

Figure 47: Microstructure and the stress-strain behavior of NC Pd–Au 50% with a grain size of 10 nm, where a) no MC is carried out during straining and b) local relaxation is carried out during straining with the highest frequency. In the snapshots the gradient color scheme is according to the displacement from the initial atomic positions. The structures are rescaled to the initial size and the imposed deformation does therefore not contribute to a local displacement. GB and stacking fault atoms are highlighted in white and black, respectively. The arrows indicate the state of the snapshot on the stress-strain curve, where three snapshots under tensile load (at a total strain of 2, 3.2 and 4 %, respectively) and one snapshot under zero external load (after unloading from a total strain of 4 %) are shown. Analysis and visualization was carried out, using OVITO [165].

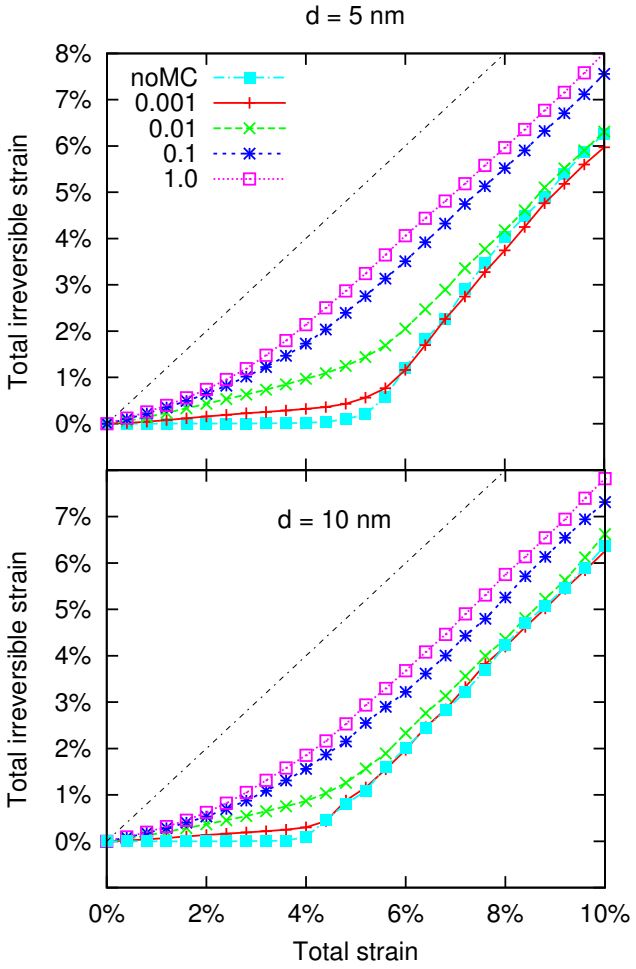

Figure 48: Total irreversible strain measured after unloading as a function of the total strain for various testing conditions and the two studied grain sizes.

response since dislocation activity and atomic displacement in the vicinity of the GB is already detectable. The reversibility must therefore be due to back stresses, which revert the various events carrying local plasticity. Apparently, the high strain rates in conventional MD simulations do not allow for local accommodation of the processes contributing to plastic deformation. This might be at the heart of the overshoot phenomena in the stress-strain behavior reported frequently from MD simulations, resulting from an excess of elastic energy in the system due to large back stresses.

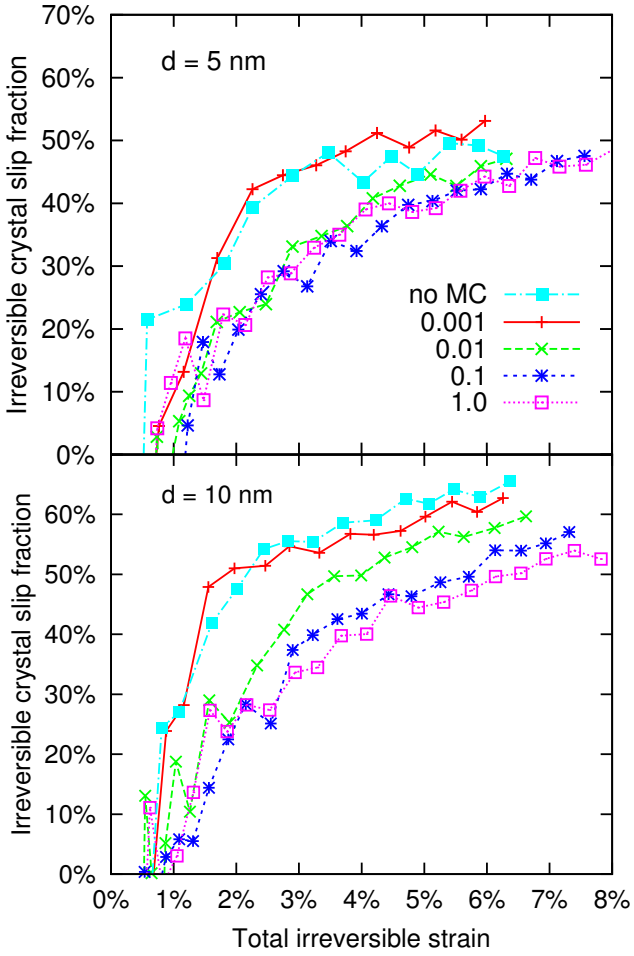

Figure 49: Contribution of crystal slip to the irreversible strain for various testing conditions and the two studied grain sizes.

12.2.2 *Irreversible contributions*

After it was observed, that the plastic strain is partly reversible, if no local relaxation allows for the accommodation of the deformation processes, the contribution of dislocation slip to the irreversible plastic strain was quantified. We therefore analyzed the unloaded structures with respect to the amount of crystal slip (as compared to the initial structure). Fig. 49 shows the contribution of irreversible crystal slip to the overall irreversible strain.

Although some of the dislocation slip events are reversed under unloading, their contribution to the irreversible strain does depend on the local relaxation. Here, enhancing the local relaxation decreases the contribution by dislocation

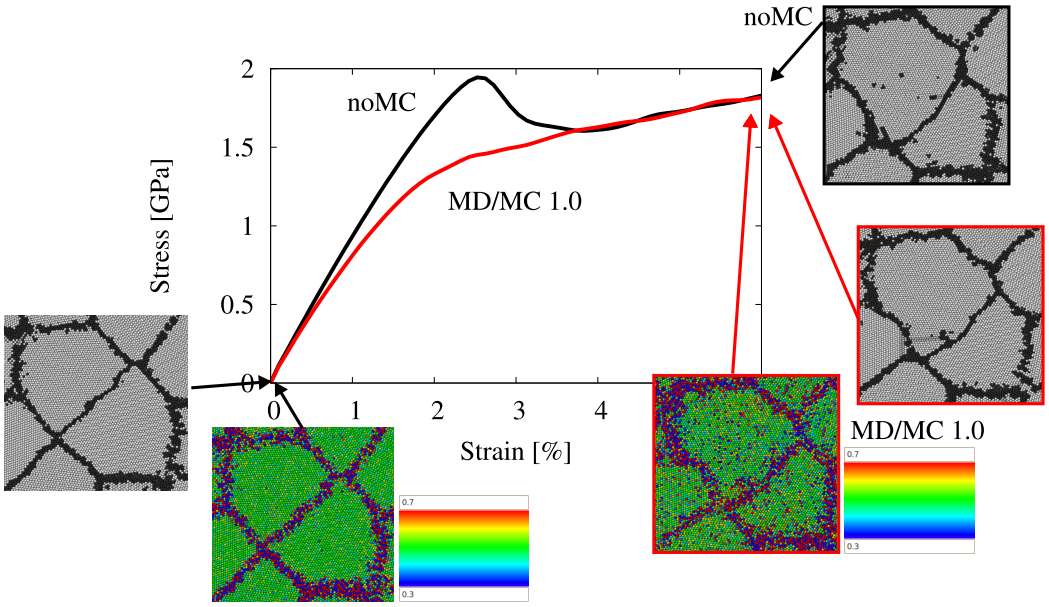

Figure 50: Snapshots and stress-strain behavior of NC Pd–Au 50% with a microstructure, where several GBs were initially aligned and which is known to deform by stress coupled GB motion (Sec. 10). The case of conventional MD (noMC) is compared to straining, where local relaxation is accounted for by the MC algorithm with a swap fraction of 1.0 and a ΔMC of 10. Color coding for the microstructures is such, that white atoms belong to the grain interior, black atoms to the GB and gray atoms are neighboring a stacking or twinning fault (according to CNA [152]). The gradient color scheme shows the local atomic concentration as the average site occupancy during the MC trial exchanges. Visualization was carried out, using OVITO [165].

slip to plastic deformation. This indicates, that the contribution by GB mediated processes such as GB sliding or normal motion as well as the movement of triple lines and quadruple nodes is more pronounced, if local relaxation takes place. Comparing the different studied grain sizes, it can be seen, that the decrease in the contribution by dislocation slip with local relaxation is stronger for the larger grain size.

12.3 EFFECT ON GB MEDIATED PLASTICITY

The effect of local relaxation on a specific GB mediated process was exemplarily studied for the case of coupled motion. Here, we tested the mechanical response of a microstructure with an average grain size of about 10 nm, which evidently deforms by stress coupled GB motion (Sec. 10). The initial microstructure (grain orientation and size) was identical to the one in Sec. 10, where a subset of GBs was

perfectly aligned prior to deformation. At the onset of yielding, stress coupled normal GB motion sets in and contributes to plastic deformation for this particular microstructure.

Prior to deformation, the sample was annealed and alloyed following the identical procedure as described for the samples above. Here, solute atoms (50 % of Au) were introduced into the microstructure via the hybrid MD/MC scheme at 600 K for 1 ns. Fig. 50 shows a part of a slice through the initial alloyed microstructure together with a slice colored according to the local atomic concentration (the average atomic occupancy during alloying by the MD/MC scheme). It can be seen, how a subset of grain boundaries is aligned prior to deformation. From the slice with the gradient color scheme according to the local concentration, it becomes evident that the GBs in this microstructure show a deviation from the composition in the grain interior. The width and magnitude of the deviation is similar to the structures discussed above as shown in Sec. 4.

The sample was then put under tensile load at a strain rate of 10^8 1/s and the evolution of the microstructure was monitored. Fig. 50 shows the stress-strain behavior for the case of tensile testing without MC and for the case where local relaxation was carried out with the highest frequency using the MC algorithm (with a swap fraction of 1.0 and a ΔMD of 10). Evidently, the stress-strain behavior for this microstructure shows similar trends as reported above. For the case, where local relaxation is not carried out, the tensile modulus as well as the yield strength are drastically increased. For both cases, the microstructure deforms by coupled GB motion, as can be seen from the slices after deformation. This demonstrates, that the barrier for the onset of normal GB motion is higher if local relaxation does not take place.

Visualizing the evolution of the local concentration during straining shows that the depletion zone around the initial GB position follows the position of the GB during straining. Local relaxation by MC swap attempts therefore also allows to mobilize the compositional gradients.

12.4 DISCUSSION

We performed hybrid MD/MC simulations of NC Pd–Au 50% alloys of two different grain sizes at various deformation conditions, which allows for local chemical and structural relaxation during straining. The stress-strain behavior of our model structures strongly depends on the frequency of local relaxation. If local relaxation through coupling to an external reservoir is carried out, the tensile modulus as well as the yield strength are drastically decreased. This effect is observed for both studied average grain sizes (5 nm and 10 nm). If local relaxation is carried out during straining the overshooting in the stress-strain behavior vanishes. Monitoring the irreversible plastic strain for different straining stages reveal that several contributions to plastic strain are reversible, if deformation

processes are not accommodated by local relaxation. Close inspection of the microstructure shows that atomic displacements in the vicinity of the GB as well as dislocation slip and the nucleation of twins can be reversed under unloading. Here, the remaining back stresses are obviously large enough, to force the different contributions out of the system. Regarding the contributions to irreversible strain we find that the fraction of dislocation slip is smaller, if local relaxation is carried out. This indicates that conventional MD straining simulations overestimate the contribution of dislocation slip to plastic deformation of nanocrystals as compared to experiments, where local relaxation is facilitated due to the much reduced strain rate. By studying the influence of local relaxation on a single GB mediated deformation mechanism (Fig. 50), namely stress driven coupled GB motion, we observe that the local relaxation drastically decreases the stress, necessary for the onset of coupled GB motion. The amount of dislocation slip as a function of total strain, on the contrary (Fig. 46 c),d)), is not affected by local relaxation.

From our observations, one can therefore reason that the barrier for dislocation nucleation and propagation is not (or less) affected by local relaxation. The barrier for the GB mediated processes such as GB sliding or normal motion, on the contrary, is severely reduced by local relaxation. Fig. 51 schematically illustrates the effect of local relaxation on the barriers for the different contributions.

The coupling to an external reservoir, which allows for atomic exchanges without accounting for the precise excange mechanisms, apparently lowers the barrier for GB plasticity. In that way, the hierarchy between different contributions to plastic deformation can be modulated. This results in a stronger contribution of dislocation slip events to plastic deformation for cases, where the frequency of local relaxation is low as compared to the imposed straining. (Such as low temperature or high strain rates.) The results do not allow for an extrapolation or translation to experimental conditions, but clarify how the contributions of individual processes to global plasticity depend on the deformation conditions. Furthermore, this might explain, why experimental works suggest a transition from GB mediated processes to regular dislocation slip at a grain size in the order of 100 nm [22, 208], while MD simulations report a transition towards dislocation mediated plasticity at around 10-20 nm grain size [59, 50].

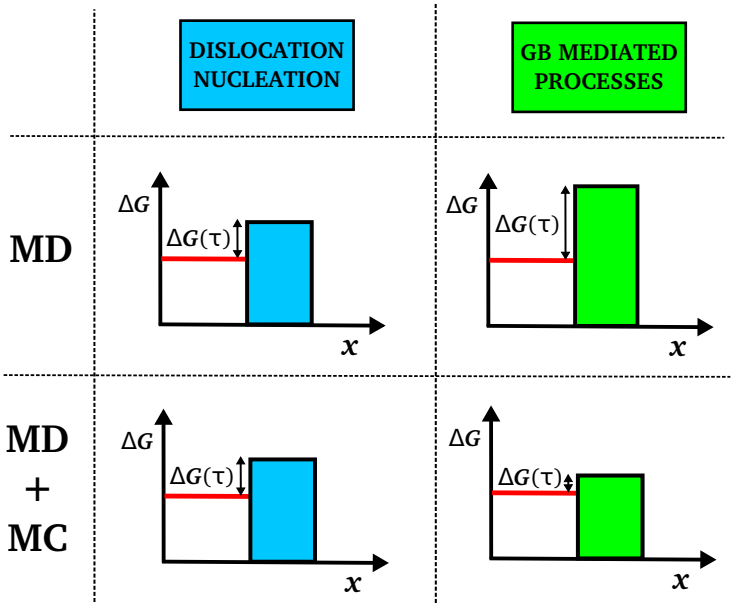

Figure 51: Schematic of the barrier for different processes under different deformation conditions. The emission, propagation and absorption of dislocations from GBs is less affected by local relaxation through coupling to an external reservoir. The barrier for GB mediated processes such as GB sliding or normal motion shows a strong dependency on local relaxation and can be effectively lowered in our simulations through coupling to the reservoir. In this way, the hierarchy between the different processes can be modulated.

Part VII

CREEP CONDITIONS

The atomistic processes of deformation at moderate temperature were the subject of the preceeding chapters. It was shown that the state of the GB can drastically influence the mechanical properties of the structures. For deformation at elevated temperature, the GBs can play an important role also for the case of CG materials. At the according temperatures, also CG materials deform by GB creep [221], where thermally activated mass transport through the GBs is the major carrier of plastic deformations. The area of predominance of Coble creep in polycrystalline fcc material is widened by a decrease in grain size [221], whereas the introduction of segregating solutes can narrow it [222].

For a NC microstructure, which has a high density of GBs it is therefore expected, that the predominance of GB creep sets in at lower temperatures, as discussed in the introduction (Sec. 1.2.2). Since solute atoms were found to drastically influence the macroscopic deformation behavior at moderate temperature, their presence in the GB may change the deformation behavior also here, where the contributing processes are restricted to the GB region.

The following chapter is therefore devoted to processes in the GBs during high temperature deformation. The thermal stability of the prepared samples is discussed and the influence of different solutes on the creep compliance of our NC model structures is evaluated.

13

GRAIN BOUNDARY CREEP

The role of diffusional GB creep has received little attention in NC materials despite its obvious implications for the use of these materials at elevated temperatures. For example, it is still uncertain whether GB diffusion processes in pure NC Cu contribute to deformation at low homologous temperatures, $T/T_m < 0.3$ [223]. In this regard, it has been demonstrated that pure NC Cu (about 28 nm grain size) can be elongated to more than 5000% at room temperature without strain hardening, suggesting GB-based mechanisms are indeed operative [34, 2]. Other work identified non-negligible creep deformation at room temperature also in NC Ni [44]. Several studies have shown further that creep rates in NC metals are proportional to d^{-3} [224] or d^{-2} [225], suggesting Coble [226] or Nabarro-Herring creep behavior [227, 228]. Other results, however, report a creep resistance orders of magnitude higher than Coble creep [229, 230]. Meyers *et al*. suggest that contamination of the GB with impurities suppresses grain-boundary sliding and thus explains these differences [2]. For example, interstitial dopants (Boron in Nickel) have been shown to significantly enhance the creep resistance of NC materials [31].

Only few studies on creep in NC structures using MD simulation have been reported, largely due the limited time-scales accessible by these simulations. It has been shown, nevertheless, that diffusional creep in these materials can be simulated via MD simulations if sufficiently high temperatures are employed [225]. While this requirement is a severe limitation, such simulations can still be useful for examining different creep mechanisms [69].

In this chapter, we employ such an approach to examine the effect of solutes on the macroscopic creep compliance of various dilute Cu alloys (Cu–Nb, Cu–Fe, Cu–Zr), focusing on Cu–Nb. The samples are identical to the ones previously tested at room temperature as presented in Sec. 7. They have an average grain size of 8 nm and solute atoms were introduced using the hybrid MD/MC scheme as discussed in Sec. 3 which locates them on energetically favorable sites.

The samples were deformed at various temperatures (ranging from 0.4 to 0.86 T_m), where T_m denotes the melting temperature of pure Cu (around 1290 K for the interatomic potential used here), to test the creep compliance of the material. Deformation was carried out under uniaxial compression with a constant

load as described in Sec. 2.5. For most simulations, the uniaxial compressive stress was set to 500 MPa. This led to strain rates on the order of 10^5-10^8 s^{-1}. The applied stress, although high, remained well below the yield stresses of the NC Cu alloys, which exceed 1 GPa. The stresses perpendicular to the compression axis were maintained near zero.

13.1 CREEP BEHAVIOR - INFLUENCE OF SOLUTES

Studying diffusional creep in NC materials by MD simulations at high temperatures requires suppression of grain growth [225]. In previous studies on pure metals, grain growth was suppressed by the microstructural design of the structure [231, 232, 225, 233]. Here, we rely solely on the pinning force of solute in the grain boundaries [89], and thus we can study systems with three dimensional microstructures and randomly oriented grains of varying size. Our procedure, however, limits the creep tests to alloys with Nb concentrations greater than 3 at.% local concentration within the GB.

Representative strain versus time curves at constant load are shown in Fig. 52 for four different samples: two with solute additions, one with Nb precipitates added to the quadruple nodes of the GBs, and the last, for pure Cu. The load in each case was 500 MPa. The initial elastic response is not shown. The strain for all of the samples initially increases approximately linearly with time. The strain rates in the two alloy samples are noticeably smaller than in the two other samples, and the reduction is seen to be larger for the alloy with higher concentration. It is noteworthy that the presence of precipitates in the quadruple nodes of the GB's has little effect on the creep rate. For larger strains a continuous transition to higher creep rates is most evident for the sample with 5.3% Nb. This will be discussed in more detail in what follows. At this point, however, we can already state this transition is unlikely associated with grain growth, since (i) Coble and Nabarro-Herring creep rates both decrease with increasing grain size and (ii) no grain growth was observed.

Fig. 53 a) shows the creep rate as a function of strain for the Cu-6.4 at.% Nb alloy at different temperatures. The creep rates increase significantly with temperature, but the general behavior of an increasing creep rate with increased strain is common to all samples. A similar behavior was observed for the case of pure NC Pd [232]. In this case the transition was attributed to the elimination of triple junctions and the associated formation of mobile dislocations. In the present study the possibility of irreversible structural changes can be ruled out, since re-equilibration of the local chemistry by the MD/MC method sets the creep rate back to its initial value (Fig. 53 a)). The observed transition is thus caused by creating chemical disorder and by driving the system from local equilibrium, rather than altering microstructural features. It is noteworthy that relaxation of creeped samples by MD alone has little effect on the creep rate after re-loading,

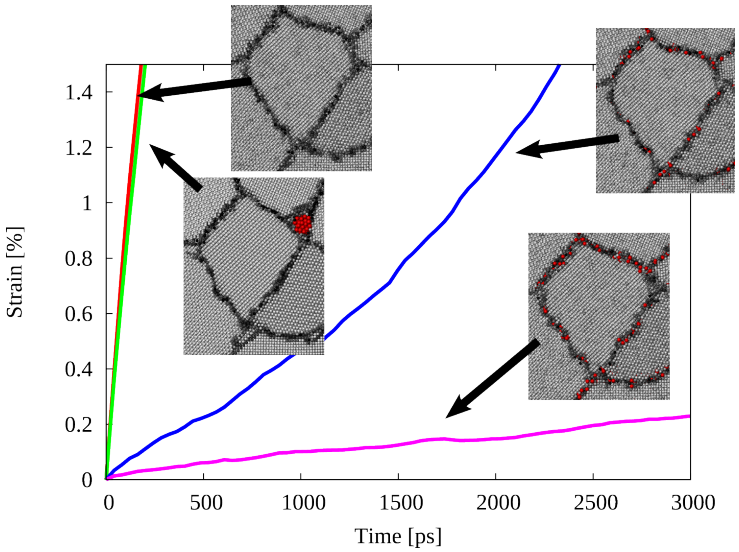

Figure 52: Thermal creep: Strain as a function of time at 0.8 T_m and a uniaxial load of 500 MPa for different compositions. The initial elastic response is not shown. (The data for the samples with 5.0 and 8.3% of Nb in the GB are shown in blue and pink, respectively.) Pure Cu (red) and a structure, where the solutes were positioned in spherical precipitates in the quadruple nodes (green) serve as references.

which provides additional evidence that the variation of creep rates is related to chemical disordering.

Fig. 53 b) shows the dependence of creep rate on the alloy composition at 0.84 T_m. Increasing the Nb concentration in the GBs strongly reduces the initial creep rate. Similar to Fig. 53 a), a transition to larger creep rates with increased strain can be observed. For reference, Fig. 53 b) additionally shows creep data for structures where solutes were introduced at random positions in the GBs and not equilibrated using the MD/MC algorithm. (These samples underwent otherwise identical treatments as the MD/MC ones, including initial equilibration by MD for 1 ns at 500 K.) The introduction of Nb at random positions does not provide chemical short-range order, and thus leads to larger creep rates. It is interesting that the creep rate (i) is insensitive to solute concentration when the solute is not located in equilibrium sites and (ii) requires only a strain of $\approx 4\%$ to convert the samples prepared with the MC/MD method to the non-equilibrated state. As we will show later, most of the solute atoms have moved at least one atomic distance after a strain of 4%.

Fig. 53 c) shows the dependence of the initial creep rate on temperature for three of the MD/MC alloys. The same general dependence of initial creep rate on temperature is observed for the three alloys. Clearly seen, however, is a strong

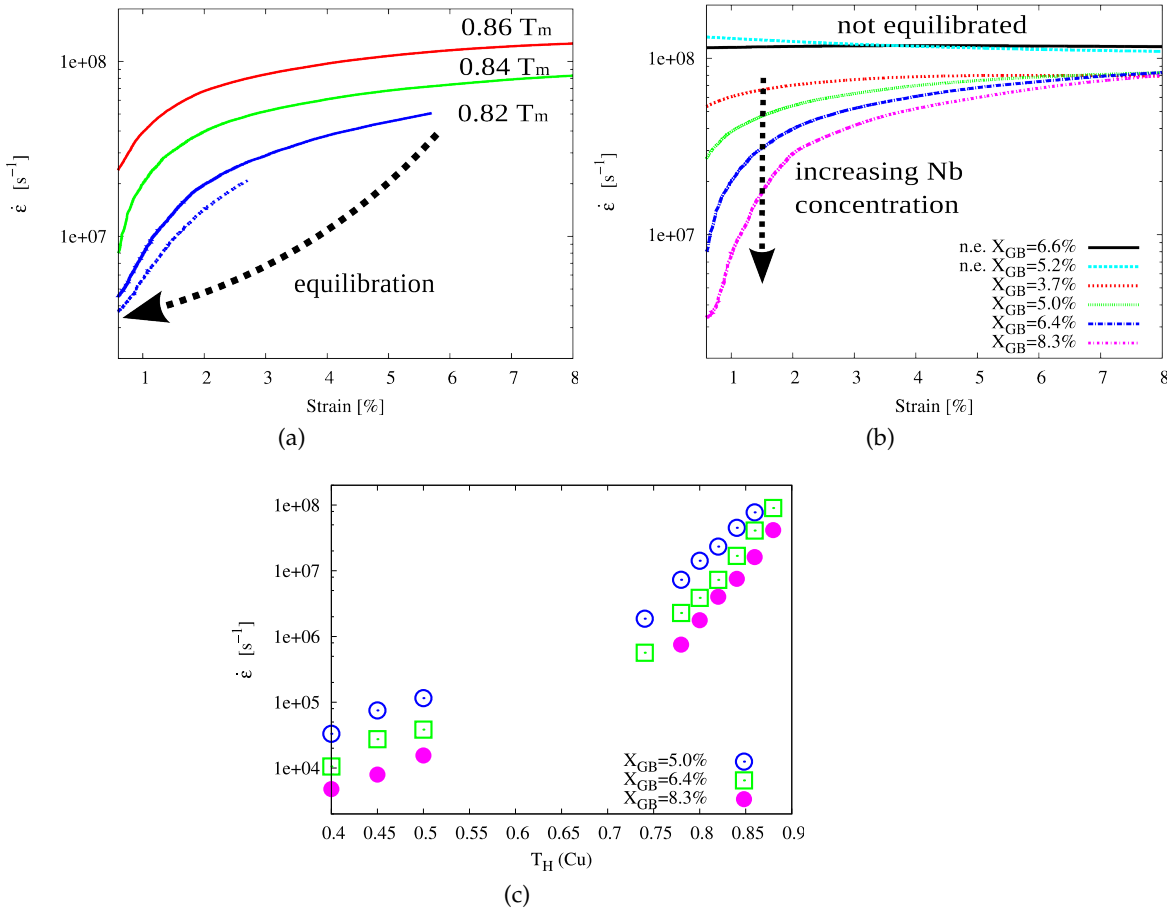

Figure 53: Temperature and equilibration effects: a) Creep rate as a function of strain for an uniaxial load of 500 MPa and different temperatures for the structure with 6.4% Nb in the GB. For one case (0.82 T_m), the structure was re-equilibrated using the MD/MC scheme after a strain of 6%. The subsequent creep rate following equilibration is plotted as a blue dashed line. b) Creep rate as a function of strain at 0.84 Tm and a uniaxial load of 500 MPa for different compositions and different relaxation states (equilibrated by MD/MC or not equilibrated (n.e.)). c) Observed initial creep rate as a function of testing temperature.

change in the temperature dependence in going from low to high temperatures, with the apparent activation energy increasing from 0.3 eV to $\approx$ 3 eV.

13.1.1 *Atomic mobility in the grain boundaries*

In a previous work on pure NC Pd it was shown that high-temperature deformation takes place by GB diffusional (Coble) creep [232]. We examined the deformation mode in the present NC Cu–Nb alloys by monitoring the relative displacements of atoms during straining. Relative atomic motion, i.e., the Lagrangian reference frame, is convenient for measuring diffusion in the present study since it avoids complications arising from the change in shape of the sample. Similar to Ref. [234], we thus define the relative displacement vector $\boldsymbol{R}_i$ by

$$\boldsymbol{R}_i = [\boldsymbol{x}_i(t + \Delta t) - \boldsymbol{x}_i(t)] - [\boldsymbol{x}_{COM}(t + \Delta t) - \boldsymbol{x}_{COM}(t)], \tag{13.1}$$

where $\boldsymbol{x}$ is the position vector and i and COM label atom i and the center of mass of the neighbors of atom i at the time t, respectively. No atoms located in the grain interiors were observed to undergo relative motion; only atoms in the GB's are observed to move. This excludes Nabarro-Herring creep and dislocation motion as potential contributors to plastic deformation. Since virtually all Nb atoms are located in the GB's we use only these atoms, for convenience, to obtain the GB diffusion coefficient. Thermal noise in the displacement vectors was suppressed by quenching the structures to 0 K after each time interval before computing $\boldsymbol{R}_i$. In addition, we excluded relative displacements smaller than half of the first nearest-neighbor (NN) distance to avoid displacements arising from local relaxations. The threshold of half the NN distance was chosen for this purpose because it reflects the barrier for diffusional atomic displacements, and it is consistent with the observed minima in the histogram of displacements (not shown). The results of these calculation are presented in Fig. 54, where a strong correlation is found between the fraction of atoms undergoing relative displacements during a fixed time step Δt (200 ps) and the measured creep rates. Remarkably, the data for various concentrations, different temperatures, and even for different stages of excitation follow the same trend. The data thus clearly illustrate that creep indeed derives from atomic motion within the GB's. For better understanding the creep mechanism, we thus focus our attention on the effect of solutes on atomic mobility in GB's.

Previous studies have revealed a relationship between GB diffusion and GB energy [235]. A similar connection can also be found between GB diffusion and excess volume (Eq. 5.2), and we examine this latter relationship here. In Fig. 55, we plot both the fraction of Nb atoms with relative displacements larger than the next-neighbour distance and the excess atomic volume as functions of time for an initially random and an equilibrated solute distribution. A clear relationship between ΔV_{at} and the number of atoms undergoing displacements (Δt = 200ps)

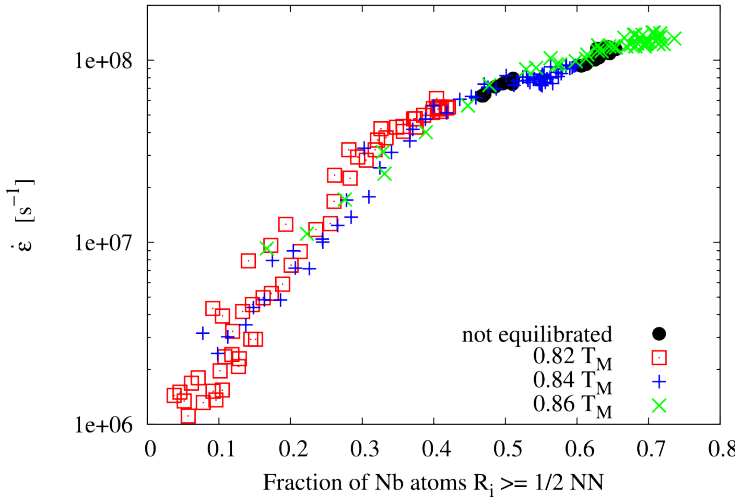

Figure 54: GB mobility controlling deformation: Creep rate as a function of the mobility of the Nb atoms in the GB, for different compositions, different temperatures and different relaxation states. The mobility is measured in terms of the fraction of Nb atoms which underwent a relative displacement with respect to neighboring Nb atoms, which exceeded half of the NN distance. (For clarity, the data for different compositions is not shown independently.)

is observed as shown in Fig. 55b. This relationship holds for both of the fully equilibrated structures and the structures where the solute atoms were inserted at random positions. While a correlation between GB diffusion and ΔV_{at} or GB energy is found during creep deformation, we do not find the simple relationship reported by Gupta [235] linking GB diffusion to GB energy, namely the so called Borisov model [189], where

$$D_{GB} = D_L \exp\left(\frac{\gamma}{\rho RT}\right). \tag{13.2}$$

D_{GB} and D_L refer to the GB and lattice diffusion coefficients, respectively, γ is the GB energy, and ρ is a constant relating the GB area to volume. Notice also that at high temperatures, the apparent activation energy is larger than lattice diffusion in Cu (2.03 - 2.09 eV) [236, 237].

13.1.2 *Transferability to other Cu alloys*

We calculated the effect of other solutes on the creep properties of NC Cu to further test the role of excess volume. These samples were produced following the same simulation scheme as described above, starting from identical initial NC Cu configurations.

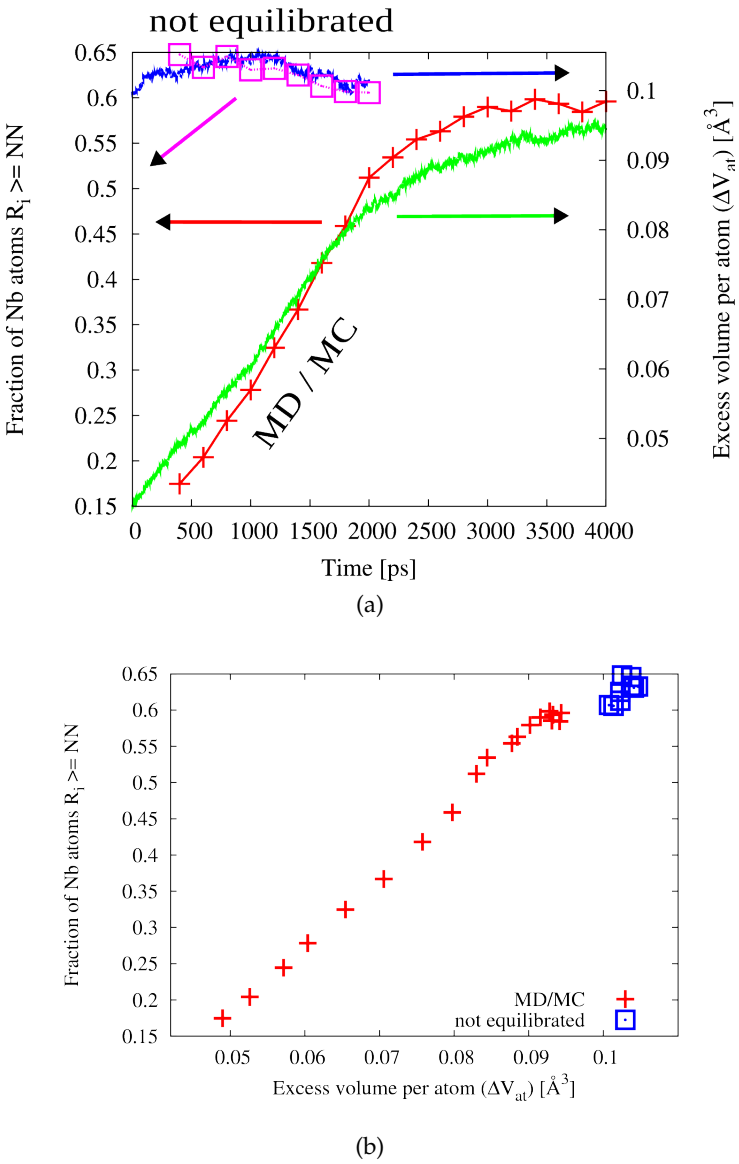

Figure 55: Correlation to excess volume: a) Fraction of atoms undergoing a relative displacement exceeding first NN distances (lines with symbols) and atomic excess volume (lines) as a function of time, where the atomic excess volume is defined as the difference in average atomic volume as compared to a single crystal of identical composition at the same temperature (see text). Shown is the data for a structure equilibrated by MD/MC (green, red) and a structure which was not equilibrated (blue, pink) with 6.4 and 5.2% of Nb in the GB, respectively. b) Correlation between the fraction of atoms undergoing a diffusive displacement and the atomic excess volume for the two data sets.

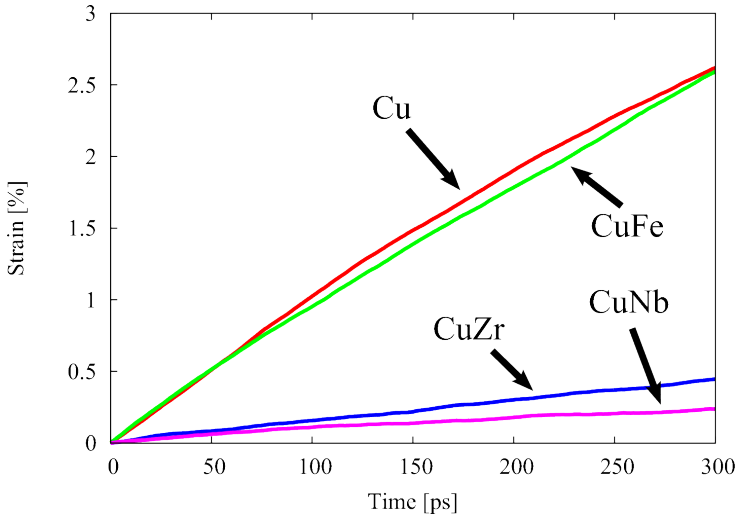

Figure 56: Transferability: Strain as a function of time at 0.82 Tm and an uniaxial load of 500 MPa for different material systems. (Pure Cu is shown as a reference.)

Fig. 56 shows the compressive strain as function of time at $0.82T_m$ for 3 different NC Cu alloys and pure NC Cu as a reference. Zr, when dissolved in fcc Cu has an atomic volume of 1.8 Ω_{Cu}, where Ω_{Cu} corresponds to the atomic volume of Cu in a fcc single crystal as reproduced by the potential [142]. This is a similarly large atomic volume as observed for Nb in fcc Cu (2.1 Ω_{Cu}) [135]. Fe, on the other hand, has a comparable atomic volume as Cu, when dissolved in a fcc Cu matrix (1.2 Ω_{Cu}) [139]. The Zr solutes are observed to greatly reduce the creep rate in NC Cu, a factor of ≈ 5, which is comparable to that of the Nb solutes. Fe has a much reduced effect, thus establishing atomic volume when dissolved in the matrix as a key parameter in suppressing GB diffusion. In the cases of pure Cu and Cu–Fe, but not Cu–Zr and Cu–Nb, we observe in addition to high creep rates, severe grain growth. This dependence of grain growth on solute size agrees with previous MD studies [90], and it is consistent with the idea that grain growth and creep are both controlled by atomic mobility in GB's.

13.1.3 *Atomistic mechanisms*

A detailed examination of the atomic motion within the GBs during creep deformation reveals that depending on the state of GB relaxation, atomic motion occurred either as independent displacements or by collective motion. We distinguish these two modes as follows. First, all atoms (independent of their type) moving more than half the NN distance within a 200 ps time window were identified as a function of time. The nature of movement of those atoms was then analyzed, following an approach by Donati et al. [160], where atomic motion

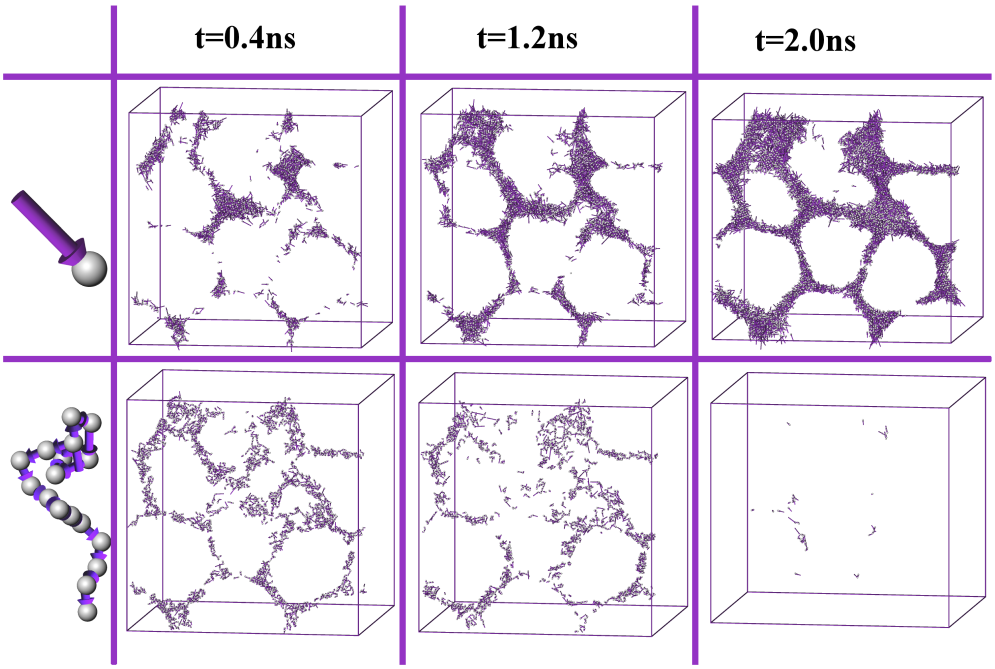

Figure 57: Atomistic mechanisms: Cross-sections through the structures at different stages of deformation at T = 0.84 T_m. The upper line shows the atoms, which underwent an independent displacement. The lower line shows the atoms which underwent a string-like collective displacement where the number of involved atoms was larger than two. (The displacements occurred during a fixed time interval of 200 ps.)

is considered stringlike or collective if the former position of a moving particle is occupied by another mobile particle. Otherwise the motion was considered independent. Fig. 57 identifies those atoms undergoing independent (top) or collective (bottom) motion in a representative slice through the simulation cell at different stages of deformation. The sample in this figure contained 6.4% Nb, was simulated at 0.84 T_m and initially equilibrated by the MC/MD method. During the initial stages of deformation, while the sample is still well equilibrated, transport in the GB's occurs predominantly by collective motion of atoms. By 2 ns, however, a clear shift to an independent displacement mode is observed. From Fig. 55, it is seen that after 2 ns $\approx$ 50% of the Nb atoms have moved. Thus, during straining at elevated temperature, the system is driven out of the well equilibrated state and the contribution by independent displacements greatly increases, with the contribution from collective motion becoming insignificant.

These findings can be understood in terms of several recently published papers. Zhang *et al.* [238, 239] showed by MD simulations that string-like cooperative motion is a regular feature of the dynamics of structurally relaxed GBs (in NC Ni at 0.48 - 0.86 T_m). These authors noted, moreover, that the dynamics of GB motion

was very similar to that found in supercooled liquids. Complementing these observations, Nagamanasa et al. report glassy dynamics at grain boundaries in colloidal crystals also for the zero-driving force limit, a regime inaccessible by MD [240]. In another study, which also employed MD simulations [241], Ritter and Albe showed that in bulk metallic glasses (BMGs) below T_g, diffusion occurred by a cooperative motion of atoms, if the glasses were well relaxed. In highly excited regions, on the other hand, e.g., within shear bands, the atomic motion occurred rather by individual displacements. These findings are thus consistent with the present results for GBs in nanocrystals, where string-like cooperative motion is most pronounced in the initial, well equilibrated state. During straining, the system is driven from this low-energy state, increasing the free volume in the GB's and thus allowing for individual displacements.

We further explored this similarity between the atomic motion in GB's in the NC Cu–Nb alloys and Cu–Nb metallic glasses by comparing the creep behavior in these materials. The metallic glass was prepared by first quenching pure liquid Cu to 50 K where equilibration and the introduction of solutes was carried out for 1 ns using the same MD/MC scheme as employed for the NC material. The creep response of the resulting structure, which contained 7 at% Nb, was then obtained as a function of temperature using a uniaxial compressive load of 100 MPa. The results comparing the creep behavior of the NC and amorphous Cu–Nb alloys are shown in Fig. 58 in an Arrhenius plot. While the apparent activation energies are different for NC and amorphous alloys, they both show a transition from high to low values as the temperature is reduced below 0.5-0.7 T_m. This is just the temperature regime that we find using MD for the glass temperature, T_g, of this alloy.

13.1.4 *Discussion*

We used MD simulations to study the effect of Nb solute on thermal creep in NC Cu structures. Using the hybrid MD/MC algorithm, the solutes were introduced at energetically favored positions. No Nb was therefore introduced within the grains of the NC structure, consistent with the thermodynamic driving force for segregation. The amount of solutes may in some cases correspond to an oversaturated solid solution where the precipitation of a second phase was suppressed by the barrier of forming a nucleus of critical size. One outcome of adding Nb solute is that it stabilizes the structures against grain growth, allowing for the treatment of a system consisting of grains of varying size and shape. The GB energy of the Cu–Nb samples was shown to decrease linearly with Nb concentration, in agreement with earlier studies. The highest concentration of Nb solutes corresponded to a vanishing GB energy. During testing under uniaxial compression at various elevated temperatures, no severe grain growth was observed. This is consistent with a fairly reduced GB energy. It is furthermore

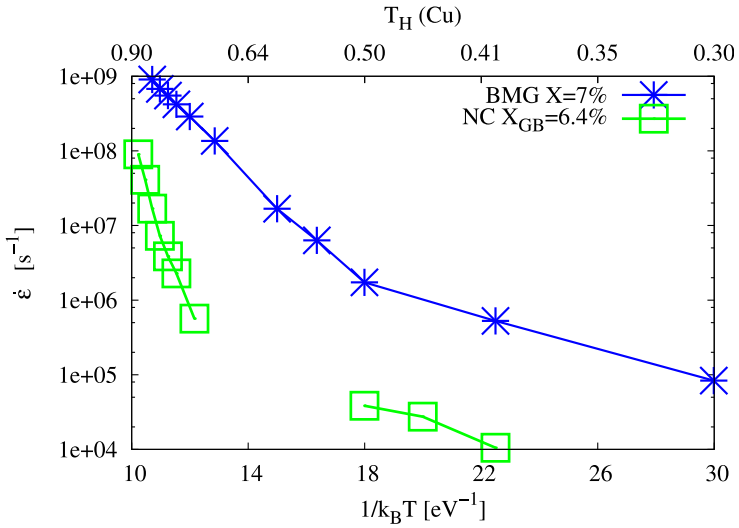

Figure 58: Comparison of initial creep rates in amorphous and NC Cu–Nb alloys: Initial creep rates of an amorphous Cu–Nb alloy (bulk metallic glass, blue) and a NC Cu–Nb alloy (green) of similar composition for various temperatures.

consistent with the observed trend for the transition in creep rate, where we find an increasing creep rate. For the case of grain growth, we would expect a decreasing trend, which we do observe for pure NC Cu, where grain growth occurs. For all tests, the applied uniaxial stress was in the range between 100 and 500 MPa which is high as compared to the stresses applied in experimental creep tests at elevated temperatures. We could, however, exclude that the applied stresses exceed the yield or flow stress of the studied material at the given temperatures.

Monitoring the resulting creep rates revealed that the introduction of solutes at favored positions and the successive relaxation results in a drastically reduced creep rate followed by a transition to higher creep rates as deformation proceeds. Comparison to structures were the segregating solutes were introduced at random positions within the GB proofed, that the lowered creep rate is due to the introduction of the solutes at energetically favored positions. Deformation of the samples therefore destroys the low energy configuration of the GB and a transition towards the creep behavior of a random distribution is observed as deformation proceeds.

Apparently, straining at elevated temperature under a high external load drives the GB configuration away from the well equilibrated state where the MD timescale is not sufficient to allow a redistribution of solutes and relaxation to obtain the energetically favored configuration by diffusional processes. A strong correlation between the mobility of the atoms within the GB and the observed creep rate could proof that the introduction of solutes can lower the overall mobil-

ity of the atoms located in the GB. The mechanism to lower the mobility in the GB is the reduction of the free volume. Introducing solutes at energetically favored positions can reduce the free volume and increase the density of the GB, resulting in a higher creep resistance and resistance to low temperature deformation as shown earlier (Sec. 7).

Comparison of the observed creep behavior for different material systems could show that the magnitude of the effect depends on the size of the solutes in the matrix. Therefore segregating solutes of differing size can drastically influence the creep behavior of NC metals by reducing the free volume in the GB.

Regarding the atomistic processes allowing for mass transport in the GBs of this NC material, we found that there are strong similarities between the NC structures and bulk amorphous material of similar composition. We demonstrated that the displacement in well equilibrated grain boundaries occurs as string-like collective motion of several atoms while a transition to single displacements is found if the system is driven out of the well-equilibrated state. This is similar to the observations made for bulk amorphous material, where string-like collective motion also occurs, but vanishes as the system is disturbed (e.g. in a shear band) [241]. The mechanism of atomic transport therefore depends in a similar manner on the local relaxation for both, GBs in NC material and BMGs. This is consistent with observations regarding the similarity between mobility in glass-forming liquids and GBs in single phase NC materials [239]. Additionally, we find a similar temperature dependence of the observed creep rates for NC and amorphous material, underlining the similarities.

Part VIII

SUMMMARY AND CONCLUSIONS

14

SUMMARY AND CONCLUSIONS

The main focus of this thesis was the investigation of atomic structures and mechanical properties of NC alloys. Several distinct material systems and microstructures were studied under different loading conditions. The key findings are summarized below.

SIMULATION OF NC ALLOYS WITH MD/MC

- The hybrid MD/MC scheme utilized in this work is well suited to introduce solutes into a given microstructure. It places the solute atoms at energetically favorable positions in accordance with the microstructure. As observed in this work, the macroscopic response of a system strongly depends on the way, solute atoms are introduced.
- The elemental distribution in a NC microstructure may deviate locally from the global composition also for the case of a completely miscible system. For the case of NC Pd–Au we showed, that for a chemically equilibrated structure, the GBs are depleted in Au.
- For a system with an ordering tendency (Ni–Fe), we could show that a NC microstructure widens the phase field of the ordered ground state. Here, the high density of GBs can act as buffer layer and accommodate any excess in either chemical species.
- The excess volume in the GBs scales with the GB energy and the concentration of segregating solutes. Segregating solutes with a large size mismatch reduce the GB energy more drastically. Segregating solutes can thus be used to modulate the GB energy as well as the GB free volume.

GRAIN BOUNDARY MEDIATED PLASTICITY

- For miscible NC alloys we observe that the intrinsic material parameters have little effect on the strength of the microstructure. For Pd–Au, we show that the macroscopic behavior is not strongly correlated to intrinsic

properties such as the stacking fault energy, the shear modulus or the burgers vector.

- For different alloys, the deformation properties are delicately dependent on the way, solute atoms are introduced into the system. We observe, that introducing the solutes by the hybrid MD/MC scheme, where the solutes are placed at energetically favored positions yields an enhanced strength as compared to placing the solutes randomly in the microstructure.
- Regarding the strength controlling parameter, we find that the change in free volume in the GBs is proportional to the maximum stress in the stress strain behavior. If the GBs are well equilibrated and the free volume in the GBs is decreased, it needs to be raised more drastically in order to allow for plastic deformation.
- For different segregating solutes, the strengthening effect scales (in the dilute limit) linearly with the concentration of the solute. The strength of the scaling depends on the atomic mismatch of the solute atoms with the matrix. A larger mismatch results in a stronger increase in the macroscopic strength. Since GB free volume and GB energy also scale linearly with composition, the strength of the material scales linearly with the GB free volume and the GB energy as well.
- Conventional solid solution strengthening is not observed for NC alloys. Varying the composition in the grains of a random NC alloy (Ni–Fe) does not affect the macroscopic mechanical properties.
- Dislocation processes in the interior are, however important for the overall ductility. For the case of an intermetallic grain interior, the samples failed by the formation of intergranular cracks for a grain size of 15 nm. Only if the grain size is further reduced to about 5 nm, the microstructure deforms plastically also for intermetallic grains. Here, the contribution by GB mediated processes is large enough to account for the deformation.

COUPLED MOTION AND MESOSCOPIC GB SLIDING

- Stress coupled GB motion contributes to plastic deformation in three dimensional NC microstructures.
- Stress coupled GB motion always competes with mesoscopic GB sliding. The prerequisite for mesoscopic GB sliding are aligned GBs. Stress coupled normal motion, however, destroys most GB alignments.
- The atomic processes of coupled motion in a high angle GB are similar to the ones observed in bicrystal simulations. The boundaries do not move at

once but in parts. The size of a typical fraction, moving at once is in the order of 10 nm^2. Characteristic structural units could not be identified.

- The competition between coupled motion and mesoscopic sliding is affected by the presence of segregating solutes. Segregating solutes can hinder coupled motion, allowing for the stabilization of a potential alignment and therefore enhance mesoscopic sliding.
- Equilibration of the solute distribution by the MD/MC scheme can strengthen the GB such that both, normal motion as well as mesoscopic sliding are suppressed.
- Regarding the transferability of the findings to different alloys, we observe, that solutes with a smaller segregation tendency (smaller atomic mismatch) pin the GBs less efficiently. For solutes with a small atomic size mismatch, stress coupled motion can occur also for the case of high solute concentrations.

HIERARCHY OF DEFORMATION PROCESSES

- By modulating local relaxation attempts during straining we showed, that during the initial stages of straining several contributions to plastic strain are reversible, if they are not locally accommodated. High strain rates therefore do not allow for the reduction of local back stresses.
- Regarding the different contributions to irreversible strain, we find that the contribution by dislocation processes is smaller, if local relaxation by trial exchanges is carried out. This indicates that conventional MD straining simulations overestimate the contribution by dislocation processes to plastic deformation.
- Studying individual deformation processes such as coupled motion with and without local relaxation showed that the barrier for the onset of coupled motion is drastically decreased, if local relaxation attempts are carried out. The evolution of dislocation density, on the contrary, is little affected by a change in local relaxation attempts. Local relaxation is therefore supposed to influence mainly the barrier for GB accommodated processes such as sliding or normal motion.
- The modified hierarchy of deformation processes at high strain rates, where local relaxation can not occur by diffusional processes, is the reason for the discrepancies between MD straining simulations and experiments. In this way, the smaller grain size at which a transition to dislocation mediated plasticity occurs as reported by MD simulations can be explained.

- When it comes to deformation at reduced strain rates, the role of GB mediated processes as discussed in previous parts of the thesis might therefore be even more important and valid for a grain size range even larger than only the smallest nanometer sizes.

GRAIN BOUNDARY CREEP

- Given a thermally stable microstructure, GB creep can be simulated with MD by an increase in temperature.
- Segregating solute in the GB increase the creep resistance, if they are located in energetically favored positions. For a random introduction of solute into the GB, the effect on the creep compliance is less severe.
- The creep resistance is increased by a reduction of the mobility in the GB. This is caused by lowering the free volume in the GB through introduction of solute atoms at energetically favorable positions.
- For a well equilibrated GB structure, atomic motion occurs by stringlike collective motion; otherwise it occurs by individual jump events. The processes of atomic transport through the GBs is therefore similar to the case of amorphous material.

OUTLOOK

The presented work has answered several open questions regarding the plasticity of NC alloys. It does, however, also serve as a starting point for ongoing work, where further research could either establish the gathered understanding and / or develop it further.

For the energetic state of the GB, we could show that it is a controlling parameter for the macroscopic strength of a NC alloy. This is qualitatively consistent with experimental findings, where a well equilibrated GB also needs to be destroyed to deform plastically. The goal, however, would be to compare the results regarding the energetic state and mechanical properties also quantitatively. Here the effect of equilibration on the state of the GB and the mechanical properties should be accessed for equivalent samples also experimentally.
Initial experimental results showed that deformation of NC microstructures not only affects the energetic state of the GBs but also stabilizes the microstructure against grain growth (Sec. 6.2.1). In order to identify the origin of this stabilization and / or to understand the atomistic processes leading to an enhanced thermal stability after deformation, additional computer simulations should be conducted. Here it could be examined, whether an imposed deformation stabilizes the structures against grain growth also for the case of a simulated NC structure. If similar effects occur, the computational model might allow to resolve the atomistic origin of the observed stabilization.
For the case of mesoscopic GB sliding, we could show that its contribution to plastic deformation is hindered by normal GB motion. This aspect should be considered in mesoscopic models, which attempt to explain macroscopic properties of NC metals on the basis of the underlying processes. Furthermore it should be analyzed, whether normal GB motion as contributor to plastic deformation and potential controlling parameter has been overlooked in other cases while interpreting results from experiments and simulations.
Regarding the limitations of classical MD straining simulations, we found that the combination of MD with MC attempts, where local relaxation effects are taken into account can influence the simulation results. The search for alternative simulation techniques, capable of overcoming several limitations, is, however, only at its beginning. Here, the main emphasis should be to develop new hybrid or stand alone methods, which allow for the simulation of experimental conditions while conserving an atomic resolution.

CONTRIBUTIONS

The results on NC Pd–Au mainly presented in Chap. 6, which were published in one article [A1], originate from a joint project with A. Stukowski. Here, A. Stukowski contributed the development of the interatomic potential (Sec. 2.1.2), the implementation of the semigrandcanonical MC routine into the MD code (Sec. 2.3) and its detailed testing to model NC Pd–Au. My contributions include the preparation, thermal annealing and characterization of the samples (Sec. 4.1.1), the simulations of plastic deformation and the according analysis and interpretation of the results (Chap. 6).

The results on dilute NC Cu alloys mainly presented in Chap. 7, which were published in one article [A2], originate from a joint project and include data from N. Vo. For Chap. 7, N. Vo contributed the simulations of plastic deformation and their analysis while my contributions include the preparation, thermal annealing and characterization (Sec. 5.2) of the samples.

The results on NC Pd–Au mainly presented in Chap. 12, which were published in one article [A7], originate from a joint project with A. Stukowski. Here, A. Stukowski contributed the method to extract dislocation slip contributions to crystal plasticity (Sec. 2.4.5) and carried out the analysis. My contributions include the preparation, thermal annealing and characterization of the samples, the simulations of plastic deformation and the according analysis and interpretation of the results (Chap. 12).

ERKLÄRUNG – DISCLAIMER

Die vorliegende Arbeit wurde im Zeitraum von Januar 2009 bis Juli 2012 im Fachgebiet Materialmodellierung am Institut für Materialwissenschaft der Technischen Universität Darmstadt bei Herrn Prof. Dr. rer. nat. Karsten Albe angefertigt.

Hiermit versichere ich an Eides statt, dass ich die vorliegende Arbeit selbstständig und nur unter Verwendung der angegebenen Hilfsmittel angefertigt habe. Von mir wurde weder an der Technischen Universität Darmstadt noch an einer anderen Hochschule ein Promotionsversuch unternommen.

Darmstadt, den 01. März 2013

Jonathan Schäfer

DANKSAGUNG – ACKNOWLEDGMENTS

Dank für die Unterstützung während meiner Zeit als wissenschaftlicher Mitarbeiter an der TU Darmstadt und während dem Anfertigen dieser Arbeit gebührt einer Reihe von Personen.

Prof. Dr. Karsten Albe danke ich für eine hervorragende Betreuung und die vielen fachlichen Diskussionen, die mir oft das Verständnis erleichtert haben und mein Interesse stets beflügelten. Auch jenseits der thematischen Grenzen hat seine zwischenmenschliche Kompetenz und sein erfrischender Humor zum Erfolg meiner gesamtheitlichen Ausbildung innerhalb seiner Arbeitsgruppe beigetragen.

Prof. Dr.-Ing. Horst Hahn danke ich für die Begutachtung meiner Arbeit.

Renate Hernichel danke ich für ihre sympathische Art und ihre Hilfsbereitschaft, welche mir erlaubten, die bürokratischen Hürden des Lebens widerstandslos zu nehmen.

Einen sehr großen Anteil an der positiven Arbeitsatmosphäre hat außerdem die gesamte MM-Arbeitsgruppe zu verantworten. Für Fragen, Probleme oder Ideen jeglicher Natur findet sich hier schnell ein kompetenter und hilfsbereiter Ansprechpartner. Besonderer Dank gilt Dr. Alexander Stukowski, der sich unabhängig von seinem eigenen Zeitplan stets für meine Probleme interessiert hat und maßgeblich am Gelingen meiner Arbeit beteiligt war. Bei Melanie Gröting, Dr.-Ing. Yvonne Ritter, Manuel Diehm, Dr. Daniel Sopu und Dr. Antti Tolvanen bedanke ich mich für die angenehme Büroatmosphäre, technischen Support, ihre Diskussionsbereitschaft sowie ihre Kommentare zu dieser Arbeit.

I am very greatful to the people from the Materials Science and Engineering department for their hospitatity during my stay at the University of Illinois. In particular Dr. Nhon Vo, Dr. Yinon Ashkenazy, Prof. Dr. Robert Averback and Prof. Dr. Pascal Bellon supported me in my work and beyond.

Der persönlichste Dank gilt meiner Familie, die mich fortwährend unterstützt hat und wesentlicher Teil meines außeruniversitären Lebens ist.

Die vorliegende Arbeit wurde finanziert von der Deutschen Forschungsgemein-

schaft durch die Forschergruppe DFG714, 'Plastizität in nanokristallinen Metallen und Legierungen'. Die Zusammenarbeit mit der University of Illinois wurde durch ein Doktorandenstipendium des Deutschen Akademischen Austauschdienstes ermöglicht. Rechenzeit wurde gewährt durch das Forschungszentrum Jülich, das Center for Scientific Computing der Goethe Universität Frankfurt und das D-Grid Projekt des Bundesministeriums für Bildung und Forschung (bwGRiD an der Universität Mannheim).

Curiculum Vitae

Personal data

Name	Jonathan Schäfer
Address	Caroline-Herschel-Str. 18 64293 Darmstadt
Email	schaefer@mm.tu-darmstadt.de
Date of birth	28. May 1983 Darmstadt, Germany

University Education

01/2013	Defense of PhD-Thesis
01/2009–07/2012	**PhD Thesis:** *"Atomistic simulations of plasticity in nanocrystalline alloys"* Materials Modeling Division (Prof. K. Albe), Technische Universität Darmstadt, Germany
05/2008–11/2008	**German Diploma Thesis:** *"Plasticity in nanocrystalline bcc Materials: A Molecular Dynamics Approach"* Materials Modeling Division (Prof. K. Albe), Technische Universität Darmstadt, Germany
10/2003–11/2008	**Studies:** Materials Science, Technische Universität Darmstadt, Germany
04/2003–09/2003	**Studies:** Physics, Technische Universität Darmstadt, Germany

Research Experience and Internships

01/2009–Present	**Research Associate** (Wissenschaftlicher Mitarbeiter), Materials Modeling Division (Prof. K. Albe), Technische Universität Darmstadt, Germany
08/2010–12/2010	**Visiting Scientist**, Department of Materials Science and Engineering (Prof. Robert Averback), University of Illinois, Urbana-Champaign, USA
11/2009–12/2009	**Visiting Scientist**, Division of Materials Physics (Prof. Kai Nordlund), University of Helsinki, Helsinki, Finland

11/2008–12/2008	**Visiting Scientist**, Division of Materials Physics (Prof. Kai Nordlund), University of Helsinki, Helsinki, Finland
05/2008–11/2008	**Research Assistant**, Materials Modeling Division (Prof. K. Albe), Technische Universität Darmstadt, Germany
05/2007–08/2007	**Industrial Internship**, element6 Ltd., Springs, South Africa
08/2006–10/2006	**Industrial Internship**, Andreas Stihl AG & Co. KG, Waiblingen, Germany
08/2005–12/2005	**Visiting Scientist**, Department of Materials Engineering (Prof. Keith Bowman), Purdue University, West Lafayette, USA
11/2004–08/2005	**Research Assistant**, Materials Science, Ceramics Group (Prof. J. Rödel), Technische Universität Darmstadt, Germany

Military Service

09/2002–03/2003	Military skiing team of LogRgt47, Dornstadt, Germany
07/2002–09/2002	Basic military service, Bruchsal, Germany

School Education

06/2002	Graduation from secondary school (*Abitur*), Gymnasium Michelstadt, Michelstadt, Germany
1993–2002	**Secondary School:** Gymnasium Michelstadt, Michelstadt, Germany

Peer Reviewed Articles

A1 J. Schäfer, A. Stukowski and K. Albe, *Plastic deformation of nanocrystalline PdAu alloys: On the interplay of grain boundary solute segregation, fault energies and grain size*, Acta Materialia **59**, 2957 (2011).

A2 N.Q. Vo, J. Schäfer, R.S. Averback, K. Albe, Y. Ashkenazy and P. Bellon, *Reaching theoretical strengths in nanocrystalline Cu by grain boundary doping*, Scripta Materialia **65**, 660 (2011).

A3 J. Schäfer and K. Albe, *Influence of solutes on the competition between mesoscopic grain boundary sliding and coupled grain boundary motion*, Scripta Materialia **66**, 315 (2012).

A4 J. Schäfer, Y. Ashkenazy, K. Albe and R.S. Averback, *Effect of solute segregation on thermal creep in dilute nanocyrstalline Cu alloys*, Materials Science and Engineering A **546**, 307 (2012).

A5 J. Schäfer and K. Albe, *Plasticity of nanocrystalline alloys with chemical order: On the strength and ductility of nanocrystalline Ni–Fe*, submitted.

A6 J. Schäfer and K. Albe, *Competing deformation mechanisms in nanocrystalline metals and alloys: Coupled motion versus grain boundary sliding*, Acta Materialia **60**, 6076 (2012).

A7 J. Schäfer, A. Stukowski and K. Albe, *The hierarchy of deformation processes in nanocrystalline metals: On the interplay of grain boundary mediated plasticity, intergranular slip and diffusional grain boundary relaxation*, submitted.

A8 A. Kobler, A. Castrup, J. Lohmiller, J. Schäfer, M. Kerber, A. Kashiwar, T. Scherer, P. Gruber, K. Albe, H. Hahn and C. Kübel, *Graingrowth and Twinning/detwinning in Tensiled Magnetron Sputtered Nanocrystalline Palladium*, in preparation.

Other Publications

A9 J. Schäfer, *Plasticity in nanocrystalline bcc Materials: A Molecular Dynamics Approach*, Diplomarbeit (2008).

A10 K. Albe, A. Stukowski, J. Schäfer, Y. Ritter and D. Farkas, *Deformation processes in nanostructured metals and alloys*, Proceedings of the NIC Symposium, FZ Jülich, Germany (2010).

Oral Presentations at International Conferences

J. Schäfer and K. Albe, *Plasticity in Nanocrystalline Tungsten*, DPG Frühjahrstagung, Dresden, Germany, 2009.

J. Schäfer, A. Stukowski and K. Albe. *Dislocation nucleation from grain boundaries in nanocrystalline Pd and Pd-Au studied by Molecular Dynamics simulations*, TMS Annual Meeting, Seattle, USA, 2010.

J. Schäfer, A. Stukowski and K. Albe, *Influence of solutes on the deformation behaviour of nanocrystalline alloys: A molecular dynamics study of PdAu*, DPG Frühjahrstagung, Regensburg, Germany, 2010.

J. Schäfer, A. Stukowski and K. Albe, *Plastic deformation of nanocrystalline PdAu alloys: On the interplay of grain boundary solute segregation, fault energies and grain size*, Tri-lateral symposium on Atomic Transport in bulk nanostructured materials and related unique properties, Rouen, France, 2010.

J. Schäfer, A. Stukowski and K. Albe, *Plasticity in nanocrystalline $FeNi_3$: On the interplay of composition, ordering and GB relaxation*, MRS Fall Meeting, Boston, USA, 2010.

J. Schäfer and K. Albe, *Mesoscopic grain boundary sliding in nanocrystalline metals and their alloys: On the interplay of grain boundary sliding, coupled grain boundary motion and segregating solutes*, International Symposium on Bulk Nanostructured Materials, Ufa, Russia, 2011.

J. Schäfer, A. Stukowski and K. Albe, *Controlling the strength of nanocrystalline metals and alloys: On the influence of the grain boundary relaxation*, International Workshop on the Plasticity of Nanocrystalline Metals, Bosen, Germany, 2011.

J. Schäfer and K. Albe, *Grain boundary mediated plasticity in nanocrystalline metals and their alloys: On the interplay of mesoscopic sliding, coupled motion and segregating solutes*, DPG Frühjahrstagung, Berlin, Germany, 2012.

Poster Presentations at International Conferences

J. Schäfer, Y. Ritter, A. Stukowski and K. Albe, *Mechanical properties of nanoscaled bcc materials / Tungsten*, Towards reality in nanoscale materials, Levi, Finland, 2008.

J. Schäfer, Y. Ritter, A. Stukowski and K. Albe, *Deformation of nanocrystalline (nc) body centered cubic (bcc) Tungsten: A Molecular Dynamics (MD) Approach*, International Workshop on the Plasticity of Nanocrystalline Metals, Bosen, Germany, 2008.

A. Stukowski, J. Schäfer and K. Albe, *Automated dislocation detection in atomistic simulations*, DPG Frühjahrstagung, Regensburg, Germany, 2010.

A. Stukowski, J. Schäfer and K. Albe, *Tailoring the mechanical properties of nc fcc metals: A MD study on the effects of twins and miscible solutes*, MSE 2010 - Materials Science and Engineering, Darmstadt, Germany, 2010.

J. Schäfer and K. Albe, *Mesoscopic sliding vs. coupled motion of grain boundaries: On the role of solutes in in nanocrystalline metals*, International Workshop on the Plasticity of Nanocrystalline Metals, Bosen, Germany, 2011.

J. Schäfer and K. Albe, *Strengthening nanocrystalline metals: On the effect of various types of solutes on the mechanical properties*, International Workshop on the Plasticity of Nanocrystalline Metals, Bosen, Germany, 2011.

Darmstadt, März 2013

BIBLIOGRAPHY

[1] H. Gleiter, Progress in Materials Science **33**, 223 (1989).

[2] M. A. Meyers, A. Mishra, and D. J. Benson, Progress in Materials Science **51**, 427 (2006).

[3] K. S. Kumar, H. Van Swygenhoven, and S. Suresh, Acta Materialia **51**, 5743 (2003).

[4] M. Dao, L. Lu, R. J. Asaro, J. T. M. De Hosson, and E. Ma, Acta Materialia **55**, 4041 (2007).

[5] F. A. Mohamed and Y. Li, Materials Science And Engineering A-Structural Materials Properties Microstructure And Processing **298**, 1 (2001).

[6] C. Suryanarayana, Advanced Engineering Materials **7**, 983 (2005).

[7] R. A. Andrievski and A. M. Glezer, Physics-Uspekhi **52**, 315 (2009).

[8] H. Van Swygenhoven and J. R. Weertman, Materials Today **9**, 24 (2006).

[9] T. J. Rupert, D. S. Gianola, Y. Gan, and K. J. Hemker, Science **326**, 1686 (2009).

[10] E. Orowan, Zeitschrift fur Physik A **89**, 605 (1934).

[11] M. Polanyi, Zeitschrift fur Physik **89**, 660 (1934).

[12] K. Lu, L. Lu, and S. Suresh, Science **324**, 349 (2009).

[13] E. O. Hall, Proceedings Of The Physical Society Of London Section B **64**, 747 (1951).

[14] N. J. Petch, Journal Of The Iron And Steel Institute **174**, 25 (1953).

[15] Y. T. Zhu and X. Z. Liao, Nature Materials **3**, 351 (2004).

[16] R. Birringer, Materials Science and Engineering: A **117**, 33 (1989).

[17] V. Y. Gertsman, R. Birringer, R. Z. Valiev, and H. Gleiter, Scripta Metallurgica et Materialia **30**, 229 (1994).

[18] R. Valiev, Nature Materials **3**, 511 (2004).

[19] H. Gleiter, Acta Materialia **48**, 1 (2000).

[20] V. Yamakov, D. Wolf, S. R. Phillpot, A. K. Mukherjee, and H. Gleiter, Nature Materials **1**, 45 (2002).

[21] V. Yamakov, D. Wolf, S. R. Phillpot, A. K. Mukherjee, and H. Gleiter, Nature Materials **3**, 43 (2004).

[22] J. Weissmuller and J. Markmann, Advanced Engineering Materials **7**, 202 (2005).

[23] X. L. Wu and E. Ma, Applied Physics Letters **88**, 231911 (2006).

[24] A. V. Sergueeva, N. A. Mara, and A. K. Mukherjee, Materials Science And Engineering A-Structural Materials Properties Microstructure And Processing **463**, 8 (2007).

[25] M. Koslowski, D. W. Lee, and L. Lei, Journal of the Mechanics and Physics of Solids **59**, 1427 (2011).

[26] Y. M. Wang, S. Cheng, Q. M. Wei, E. Ma, T. G. Nieh, and A. Hamza, Scripta Materialia **51**, 1023 (2004).

[27] A. J. Detor and C. A. Schuh, Journal of Materials Research **22**, 3233 (2007).

[28] N. Q. Vo, R. S. Averback, P. Bellon, and A. Caro, Physical Review B **78**, 241402 (2008).

[29] N. Q. Vo, R. S. Averback, P. Bellon, and A. Caro, Scripta Materialia **61**, 76 (2009).

[30] W. M. Yin, S. H. Whang, and R. A. Mirshams, Acta Materialia **53**, 383 (2005).

[31] W. M. Yin and S. H. Whang, Scripta Materialia **44**, 569 (2001).

[32] A. Caro, D. Farkas, E. M. Bringa, G. H. Gilmer, and L. A. Zepeda-Ruiz, Materials Science Forum **633-634**, 21 (2010).

[33] R. K. Rajgarhia, D. E. Spearot, and A. Saxena, Journal of Materials Research **25**, 411 (2010).

[34] L. Lu, M. L. Sui, and K. Lu, Science **287**, 1463 (2000).

[35] Y. Champion, C. Langlois, S. Guerin-Mailly, P. Langlois, J. L. Bonnentien, and M. J. Hytch, Science **300**, 310 (2003).

[36] S. R. Agnew, B. R. Elliott, C. J. Youngdahl, K. J. Hemker, and J. R. Weertman, Materials Science And Engineering A-Structural Materials Properties Microstructure And Processing **285**, 391 (2000).

[37] L. Kurmanaeva, Y. Ivanisenko, J. Markmann, K. Yang, H. J. Fecht, and J. Weissmuller, Physica Status Solidi-rapid Research Letters **4**, 130 (2010).

[38] T. H. Fang, W. L. Li, N. R. Tao, and K. Lu, Science **331**, 1587 (2011).

[39] Y. M. Wang and E. Ma, Acta Materialia **52**, 1699 (2004).

[40] R. Z. Valiev, I. V. Alexandrov, Y. T. Zhu, and T. C. Lowe, Journal of Materials Research **17**, 5 (2002).

[41] I. Brooks, G. Palumbo, G. D. Hibbard, Z. R. Wang, and U. Erb, Journal of Materials Science **46**, 7713 (2011).

[42] M. Ames, M. Grewer, C. Braun, and R. Birringer, Materials Science and Engineering: A **546**, 248 (2012).

[43] S. X. McFadden, R. S. Mishra, R. Z. Valiev, A. P. Zhilyaev, and A. K. Mukherjee, Nature **398**, 684 (1999).

[44] B. Moser, T. Hanlon, K. S. Kumar, and S. Suresh, Scripta Materialia **54**, 1151 (2006).

[45] A. H. Chokshi, A. Rosen, J. Karch, and H. Gleiter, Scripta Metallurgica **23**, 1679 (1989).

[46] F. A. Mohamed and H. Yang, Metallurgical and Materials Transactions A: Physical Metallurgy and Materials Science **41A**, 823 (2010).

[47] F. Louchet, J. Weiss, and T. Richeton, Physical Review Letters **97**, 075504 (2006).

[48] J. C. M. Li, Applied Physics Letters **90**, 041912 (2007).

[49] J. Chen, L. Lu, and K. Lu, Scripta Materialia **54**, 1913 (2006).

[50] N. Q. Vo, R. S. Averback, P. Bellon, S. Odunuga, and A. Caro, Physical Review B **77**, 134108 (2008).

[51] H. Van Swygenhoven, Materials Science and Engineering: A **483-484**, 33 (2008).

[52] J. Li, A. H. W. Ngan, and P. Gumbsch, Acta Materialia **51**, 5711 (2003).

[53] J. Schiotz, F. D. Di Tolla, and K. W. Jacobsen, Nature **391**, 561 (1998).

[54] J. Schiotz and K. W. Jacobsen, Science **301**, 1357 (2003).

[55] H. VanSwygenhoven and A. Caro, Nanostructured Materials **9**, 669 (1997).

[56] H. Van Swygenhoven, M. Spaczer, A. Caro, and D. Farkas, Physical Review B **60**, 22 (1999).

[57] S. L. Frederiksen, K. W. Jacobsen, and J. Schiotz, Acta Materialia **52**, 5019 (2004).

[58] Z. L. Pan, Y. L. Li, and Q. Wei, Acta Materialia **56**, 3470 (2008).

[59] J. Schiotz, Scripta Materialia **51**, 837 (2004).

[60] D. Wolf, V. Yamakov, S. R. Phillpot, A. Mukherjee, and H. Gleiter, Acta Materialia **53**, 1 (2005).

[61] H. Van Swygenhoven and J. R. Weertman, Scripta Materialia **49**, 625 (2003).

[62] J. Schiotz, T. Vegge, F. D. Di Tolla, and K. W. Jacobsen, Physical Review B **60**, 11971 (1999).

[63] H. Van Swygenhoven, P. M. Derlet, and A. Hasnaoui, Advanced Engineering Materials **5**, 345 (2003).

[64] A. Hasnaoui, H. Van Swygenhoven, and P. M. Derlet, Acta Materialia **50**, 3927 (2002).

[65] J. P. Hirth, Metallurgical Transactions **3**, 3047 (1972).

[66] C. W. Price and J. P. Hirth, Materials Science and Engineering **9**, 15 (1972).

[67] P. M. Derlet, A. Hasnaoui, and H. Van Swygenhoven, Scripta Materialia **49**, 629 (2003).

[68] D. H. Warner and W. A. Curtin, Acta Materialia **57**, 4267 (2009).

[69] Y. J. Wang, A. Ishii, and S. Ogata, Physical Review B **84**, 224102 (2011).

[70] Q. Wei, Journal of Materials Science **42**, 1709 (2007).

[71] Y. T. Zhu and T. G. Langdon, Materials Science And Engineering A-Structural Materials Properties Microstructure And Processing **409**, 234 (2005).

[72] K. Kadau, T. C. Germann, P. S. Lomdahl, B. L. Holian, D. Kadau, P. Entel, M. Kreth, F. Westerhoff, and D. E. Wolf, Metallurgical and Materials Transactions A: Physical Metallurgy and Materials Science **35A**, 2719 (2004).

[73] Z. W. Shan, E. A. Stach, J. M. K. Wiezorek, J. A. Knapp, D. M. Follstaedt, and S. X. Mao, Science **305**, 654 (2004).

[74] Y. M. Wang, A. V. Hamza, and E. Ma, Acta Materialia **54**, 2715 (2006).

[75] R. J. Asaro and S. Suresh, Acta Materialia **53**, 3369 (2005).

[76] H. Conrad, Nanotechnology **18**, 325701 (2007).

[77] D. S. Gianola, D. H. Warner, J. F. Molinari, and K. J. Hemker, Scripta Materialia **55**, 649 (2006).

[78] F. Mompiou, M. Legros, and D. Caillard, Journal of Materials Science **46**, 4308 (2011).

[79] J. A. Sharon, P. C. Su, F. B. Prinz, and K. J. Hemker, Scripta Materialia **64**, 25 (2011).

[80] M. W. Chen, E. Ma, K. J. Hemker, H. W. Sheng, Y. M. Wang, and X. M. Cheng, Science **300**, 1275 (2003).

[81] Z. Budrovic, H. Van Swygenhoven, P. M. Derlet, S. Van Petegem, and B. Schmitt, Science **304**, 273 (2004).

[82] D. H. Warner, W. A. Curtin, and S. Qu, Nature Materials **6**, 876 (2007).

[83] H. Van Swygenhoven, M. Spaczer, and A. Caro, Acta Materialia **47**, 3117 (1999).

[84] Y. J. Wei, A. F. Bower, and H. J. Gao, Acta Materialia **56**, 1741 (2008).

[85] B. Gunther, A. Kumpmann, and H. D. Kunze, Scripta Metallurgica et Materialia **27**, 833 (1992).

[86] J. Weissmuller, J. Loffler, and M. Kleber, Nanostructured Materials **6**, 105 (1995).

[87] A. J. Detor and C. A. Schuh, Acta Materialia **55**, 371 (2007).

[88] S. G. Mayr and D. Bedorf, Physical Review B **76**, 024111 (2007).

[89] P. C. Millett, R. P. Selvam, and A. Saxena, Acta Materialia **54**, 297 (2006).

[90] P. C. Millett, R. P. Selvam, and A. Saxena, Acta Materialia **55**, 2329 (2007).

[91] P. C. Millett, R. P. Selvan, S. Bansal, and A. Saxena, Acta Materialia **53**, 3671 (2005).

[92] A. J. Detor and C. A. Schuh, Acta Materialia **55**, 4221 (2007).

[93] J. R. Trelewicz and C. A. Schuh, Physical Review B **79**, 094112 (2009).

[94] R. Kirchheim, Acta Materialia **50**, 413 (2002).

[95] C. E. Krill, H. Ehrhardt, and R. Birringer, Zeitschrift Fur Metallkunde **96**, 1134 (2005).

[96] I. S. Choi, R. Schwaiger, L. Kurmanaeva, and O. Kraft, Scripta Materialia **61**, 64 (2009).

[97] H. Van Swygenhoven, P. M. Derlet, and A. G. Froseth, Nature Materials **3**, 399 (2004).

[98] N. Bernstein and E. B. Tadmor, Physical Review B **69**, 094116 (2004).

[99] E. B. Tadmor and N. Bernstein, Journal Of The Mechanics And Physics Of Solids **52**, 2507 (2004).

[100] S. Kibey, J. B. Liu, D. D. Johnson, and H. Sehitoglu, Acta Materialia **55**, 6843 (2007).

[101] S. A. Kibey, L. L. Wang, J. B. Liu, H. T. Johnson, H. Sehitoglu, and D. D. Johnson, Physical Review B **79**, 214202 (2009).

[102] D. Udler and D. N. Seidman, Physica Status Solidi B-Basic Research **172**, 267 (1992).

[103] T. J. Rupert, J. C. Trenkle, and C. A. Schuh, Acta Materialia **59**, 1619 (2011).

[104] X. F. Zhang, T. Fujita, D. Pan, J. S. Yu, T. Sakurai, and M. W. Chen, Materials Science And Engineering A-Structural Materials Properties Microstructure And Processing **527**, 2297 (2010).

[105] C. A. Schuh, T. G. Nieh, and H. Iwasaki, Acta Materialia **51**, 431 (2003).

[106] T. Frolov, K. Darling, L. Kecskes, and Y. Mishin, Acta Materialia **60**, 2158 (2012).

[107] D. E. Spearot and D. L. McDowell, Journal Of Engineering Materials And Technology-Transactions Of The Asme **131**, 041204 (2009).

[108] P. C. Millett, R. P. Selvam, and A. Saxena, Materials Science And Engineering A-Structural Materials Properties Microstructure And Processing **431**, 92 (2006).

[109] A. Elsener, O. Politano, P. M. Derlet, and H. Van Swygenhoven, Acta Materialia **57**, 1988 (2009).

[110] D. S. Gianola, B. G. Mendis, X. M. Cheng, and K. J. Hemker, Materials Science And Engineering A-Structural Materials Properties Microstructure And Processing **483-84**, 637 (2008).

[111] R. K. Rajgarhia, D. E. Spearot, and A. Saxena, Modelling and Simulation in Materials Science and Engineering **17**, 055001 (13 pp.) (2009).

[112] D. A. Molodov, T. Gorkaya, and G. Gottstein, Journal of Materials Science **46**, 4318 (2011).

[113] S. Brandstetter, K. Zhang, A. Escuadro, J. R. Weertman, and H. Van Swygenhoven, Scripta Materialia **58**, 61 (2008).

[114] M. P. Allen and D. J. Tildesley, *Computer Simulation of Liquids* (Clarendon Press, Oxford, 1986).

[115] Y. Ritter, Ph.D. thesis, TU Darmstadt, 2011.

[116] S. Plimpton, Journal of Computational Physics **117**, 1 (1995).

[117] W. C. Swope, H. C. Andersen, P. H. Berens, and K. R. Wilson, Journal of Chemical Physics **76**, 637 (1982).

[118] D. C. Rapaport, *The art of molecular dynamics simulation* (Cambridge University Press, Cambridge, 1995).

[119] M. J. Buehler, A. Hartmaier, H. J. Gao, M. Duchaineau, and F. F. Abraham, Computer Methods In Applied Mechanics And Engineering **193**, 5257 (2004).

[120] M. S. Daw and M. I. Baskes, Physical Review B **29**, 6443 (1984).

[121] A. Stukowski, B. Sadigh, P. Erhart, and A. Caro, Modelling and Simulation in Materials Science and Engineering **17**, 075005 (2009).

[122] A. Caro, M. Caro, E. M. Lopasso, and D. A. Crowson, Applied Physics Letters **89**, 121902 (2006).

[123] M. W. Finnis and J. E. Sinclair, Philosophical Magazine A-Physics Of Condensed Matter Structure Defects And Mechanical Properties **50**, 45 (1984).

[124] S. M. Foiles and J. J. Hoyt, Technical report, Sandia National Laboratories (unpublished).

[125] G. J. Ackland, G. Tichy, V. Vitek, and M. W. Finnis, Philosophical Magazine A-Physics Of Condensed Matter Structure Defects And Mechanical Properties **56**, 735 (1987).

[126] in *Landolt–Börnstein* (Springer Berlin Heidelberg, ADDRESS, 2002), Vol. Group IV Physical Chemistry, Chap. Binary Systems, pp. 283–286.

[127] A. Nagasawa, Y. Matsuo, and J. Kakinoki, Journal of the Physical Society of Japan **20**, 1881 (1965).

[128] Y. Matsuo, A. Nagasawa, and J. Kakinoki, Journal of the Physical Society of Japan **21**, 2633 (1966).

[129] S. Curtarolo, D. Morgan, and G. Ceder, Calphad-Computer Coupling Of Phase Diagrams And Thermochemistry **29**, 163 (2005).

[130] M. H. F. Sluiter, C. Colinet, and A. Pasturel, Physical Review B **73**, 174204 (2006).

[131] I. Atanasov and M. Hou, Surface Science **603**, 2639 (2009).

[132] G. Bonny, R. C. Pasianot, and L. Malerba, Philosophical Magazine **89**, 711 (2009).

[133] M. I. Mendelev, S. Han, D. J. Srolovitz, G. J. Ackland, D. Y. Sun, and M. Asta, Philosophical Magazine **83**, 3977 (2003).

[134] A. F. Voter and S. P. Chen, Characterization of Defects in Materials Symposium 175 (1987).

[135] M. J. Demkowicz and R. G. Hoagland, Journal of Nuclear Materials **372**, 45 (2008).

[136] Y. Mishin, M. J. Mehl, D. A. Papaconstantopoulos, A. F. Voter, and J. D. Kress, Physical Review B **63**, 224106 (2001).

[137] R. A. Johnson and D. J. Oh, Journal of Materials Research **4**, 1195 (1989).

[138] P. L. Williams, Y. Mishin, and J. C. Hamilton, Modelling and Simulation in Materials Science and Engineering **14**, 817 (2006).

[139] M. Ludwig, D. Farkas, D. Pedraza, and S. Schmauder, Modelling and Simulation in Materials Science and Engineering **6**, 19 (1998).

[140] A. Voter, Technical report, Los Alamos National Laboratory (unpublished).

[141] G. Simonelli, R. Pasianot, and E. J. Savino, Materials Theory and Modelling Symposium 567 (1993).

[142] M. I. Mendelev, D. J. Sordelet, and M. J. Kramer, Journal of Applied Physics **102**, 043501 (2007).

[143] M. I. Mendelev and G. J. Ackland, Philosophical Magazine Letters **87**, 349 (2007).

[144] M. I. Mendelev, M. J. Kramer, C. A. Becker, and M. Asta, Philosophical Magazine **88**, 1723 (2008).

[145] B. Sadigh, P. Erhart, A. Stukowski, A. Caro, E. Martinez, and L. Zepeda-Ruiz, Physical Review B **85**, 184203 (2012).

[146] P. Erhart, A. Caro, M. S. de Caro, and B. Sadigh, Physical Review B **77**, 134206 (2008).

[147] F. M. Marquez, C. Cienfuegos, B. K. Pongsai, M. Y. Lavrentiev, N. L. Allan, J. A. Purton, and G. D. Barrera, Modelling and Simulation in Materials Science and Engineering **11**, 115 (2003).

[148] N. L. Allan, G. D. Barrera, M. Y. Lavrentiev, C. L. Freeman, I. T. Todorov, and J. A. Purton, Computational Materials Science **36**, 42 (2006).

[149] A. Stukowski, Ph.D. thesis, TU Darmstadt, 2010.

[150] H. B. Aaron and G. F. Bolling, Surface Science **31**, 27 (1972).

[151] C. H. Rycroft, G. S. Grest, J. W. Landry, and M. Z. Bazant, Physical Review E **74**, 021306 (2006).

[152] J. D. Honeycutt and H. C. Andersen, J. Phys. Chem. **91**, 4950 (1987).

[153] C. L. Kelchner, S. J. Plimpton, and J. C. Hamilton, Physical Review B **58**, 11085 (1998).

[154] D. Faken and H. JÃşnsson, Computational Materials Science **2**, 279 (1994).

[155] H. Tsuzuki, P. S. Branicio, and J. P. Rino, Computer Physics Communications **177**, 518 (2007).

[156] J. M. Cowley, Physical Review **77**, 669 (1950).

[157] A. Stukowski and K. Albe, Modelling and Simulation in Materials Science and Engineering **18**, 025016 (2010).

[158] A. Stukowski and K. Albe, Modelling and Simulation in Materials Science and Engineering **18**, 085001 (2010).

[159] A. Stukowski and A. Arsenlis, Modelling and Simulation in Materials Science and Engineering **20**, 035012 (2012).

[160] C. Donati, J. F. Douglas, W. Kob, S. J. Plimpton, P. H. Poole, and S. C. Glotzer, Physical Review Letters **80**, 2338 (1998).

[161] G. Z. Voronoi, J. Reine Angew. Math. **134**, 199 (1908).

[162] H. J. C. Berendsen, J. P. M. Postma, W. F. van Gunsteren, A. DiNola, and J. R. Haak, Journal of Chemical Physics **81**, 3684 (1984).

[163] H. Y. Wang, R. Najafabadi, D. J. Srolovitz, and R. Lesar, Philosophical Magazine A-Physics Of Condensed Matter Structure Defects And Mechanical Properties **65**, 625 (1992).

[164] A. P. Sutton, Philosophical Transactions Of The Royal Society Of London Series A-Mathematical Physical And Engineering Sciences **341**, 233 (1992).

[165] A. Stukowski, Modelling and Simulation in Materials Science and Engineering **18**, 015012 (2010).

[166] C. Cheung, F. Djuanda, U. Erb, and G. Palumbo, Nanostructured Materials **5**, 513 (1995).

[167] M. J. Mayo, A. Suresh, and W. D. Porter, Reviews on Advanced Materials Science **5**, 100 (2003).

[168] S. Kibey, Ph.D. thesis, University of Illinois, 2007.

[169] J. A. Zimmerman, H. J. Gao, and F. F. Abraham, Modelling and Simulation in Materials Science and Engineering **8**, 103 (2000).

[170] J. R. Rice, Journal Of The Mechanics And Physics Of Solids **40**, 239 (1992).

[171] E. B. Tadmor and S. Hai, Journal of the Mechanics and Physics of Solids **51**, 765 (2003).

[172] X. L. Wu and Y. T. Zhu, Applied Physics Letters **89**, 031922 (2006).

[173] R. K. Rajgarhia, A. Saxena, D. E. Spearot, K. T. Hartwig, K. L. More, E. A. Kenik, and H. Meyer, Journal of Materials Science **45**, 6707 (2010).

[174] Y. Purohit, L. Sun, D. L. Irving, R. O. Scattergood, and D. W. Brenner, Materials Science And Engineering A-Structural Materials Properties Microstructure And Processing **527**, 1769 (2010).

[175] E. Botcharova, J. Freudenberger, and L. Schultz, Acta Materialia **54**, 3333 (2006).

[176] E.-M. Steyskal, B. Oberdorfer, W. Sprengel, M. Zehetbauer, R. Pippan, and R. Wurschum, Physical Review Letters **108**, 055504 (2012).

[177] R. Birringer, C. E. Krill, and M. Klingel, Philosophical Magazine Letters **72**, 71 (1995).

[178] H. Zhang and D. J. Srolovitz, Acta Materialia **54**, 623 (2006).

[179] F. Tang and J. M. Schoenung, Materials Science And Engineering A-Structural Materials Properties Microstructure And Processing **493**, 101 (2008).

[180] C. Brandl, P. M. Derlet, and H. Van Swygenhoven, Philosophical Magazine **89**, 3465 (2009).

[181] Z. H. Jin, P. Gumbsch, E. Ma, K. Albe, K. Lu, H. Hahn, and H. Gleiter, Scripta Materialia **54**, 1163 (2006).

[182] Z. H. Jin, P. Gumbsch, K. Albe, E. Ma, K. Lu, H. Gleiter, and H. Hahn, Acta Materialia **56**, 1126 (2008).

[183] S. Yip, Nature **391**, 532 (1998).

[184] H. Conrad and J. Narayan, Applied Physics Letters **81**, 2241 (2002).

[185] H. Conrad and J. Narayan, Acta Materialia **50**, 5067 (2002).

[186] A. Stukowski, K. Albe, and D. Farkas, Physical Review B **82**, 224103 (2010).

[187] M. Deckarm, C. Braun, K. Schmitt, and R. Birringer (unpublished).

[188] M. A. Tschopp and D. L. McDowell, Applied Physics Letters **90**, 121916 (2007).

[189] V. Borisov, V. Golikov, and G. Scherbedinskiy, Physics of Metals and Metallography **17**, 80 (1964).

[190] H. Q. Li, H. Choo, Y. Ren, T. A. Saleh, U. Lienert, P. K. Liaw, and F. Ebrahimi, Physical Review Letters **101**, 015502 (2008).

[191] R. Schwaiger, J. T. Reszat, K. Bade, J. Aktaa, and O. Kraft, International Journal of Materials Research **100**, 68 (2009).

[192] R. Bohn, T. Haubold, R. Birringer, and H. Gleiter, Scripta Metallurgica et Materialia **25**, 811 (1991).

[193] T. Haubold, R. Bohn, R. Birringer, and H. Gleiter, Materials Science And Engineering A-Structural Materials Properties Microstructure And Processing **153**, 679 (1992).

[194] M. J. Marcinkowski, N. Brown, and R. M. Fisher, Acta Metallurgica **9**, 129 (1961).

[195] B. H. Kear and H. G. Wilsdorf, Transactions of the Metallurgical Society of Aime **224**, 382 (1962).

[196] Z. Bojar, P. Jozwik, and J. Bystrzycki, Scripta Materialia **55**, 399 (2006).

[197] J. S. C. Jang and C. C. Koch, Journal of Materials Research **5**, 498 (1990).

[198] C. Rentenberger and H. P. Karnthaler, Acta Materialia **53**, 3031 (2005).

[199] C. Gammer, C. Mangler, H. P. Karnthaler, and C. Rentenberger, Scripta Materialia **65**, 57 (2011).

[200] S. Brandstetter, H. Van Swygenhoven, S. Van Petegem, B. Schmitt, R. Maass, and P. M. Derlet, Advanced Materials **18**, 1545 (2006).

[201] Y. F. Mo, D. Stone, and I. Szlufarska, Journal of Physics D-applied Physics **44**, 405401 (2011).

[202] J. W. Cahn, Y. Mishin, and A. Suzuki, Acta Materialia **54**, 4953 (2006).

[203] K. A. Padmanabhan and J. Schlipf, Materials Science and Technology **12**, 391 (1996).

[204] H. Hahn and K. A. Padmanabhan, Philosophical Magazine B-physics of Condensed Matter Statistical Mechanics Electronic Optical and Magnetic Properties **76**, 559 (1997).

[205] J. W. Cahn and J. E. Taylor, Acta Materialia **52**, 4887 (2004).

[206] K. A. Padmanabhan, G. P. Dinda, H. Hahn, and H. Gleiter, Materials Science And Engineering A-Structural Materials Properties Microstructure And Processing **452**, 462 (2007).

[207] J. Markmann, P. Bunzel, H. Rosner, K. W. Liu, K. A. Padmanabhan, R. Birringer, H. Gleiter, and J. Weissmuller, Scripta Materialia **49**, 637 (2003).

[208] Y. Ivanisenko, L. Kurmanaeva, J. Weissmueller, K. Yang, J. Markmann, H. Rosner, T. Scherer, and H. . J. Fecht, Acta Materialia **57**, 3391 (2009).

[209] A. Hasnaoui, H. Van Swygenhoven, and P. M. Derlet, Physical Review B **66**, 184112 (2002).

[210] M. Velasco, H. Van Swygenhoven, and C. Brandl, Scripta Materialia **65**, 151 (2011).

[211] K. A. Padmanabhan and H. Gleiter, Materials Science And Engineering A-Structural Materials Properties Microstructure And Processing **381**, 28 (2004).

[212] T. Gorkaya, K. D. Molodov, D. A. Molodov, and G. Gottstein, Acta Materialia **59**, 5674 (2011).

[213] K. L. Merkle, L. J. Thompson, and F. Phillipp, Interface Science **12**, 277 (2004).

[214] A. F. Voter, F. Montalenti, and T. C. Germann, Annual Review of Materials Research **32**, 321 (2002).

[215] J. Li, S. Sarkar, W. T. Cox, T. J. Lenosky, E. Bitzek, and Y. Z. Wang, Physical Review B **84**, 054103 (2011).

[216] S. Hara and J. Li, Physical Review B **82**, 184114 (2010).

[217] V. Tomar, Journal of Applied Physics **101**, 103512 (2007).

[218] V. Tomar, Physica Status Solidi A-Applications And Materials Science **204**, 3340 (2007).

[219] P. Tiwary and A. van de Walle, Physical Review B **84**, 100301 (2011).

[220] L. D. Nguyen, K. L. Baker, and D. H. Warner, Physical Review B **84**, 024118 (2011).

[221] M. F. Ashby, Acta Metallurgica **20**, 887 (1972).

[222] E. D. Hondros and P. J. Henderson, Metallurgical Transactions A-physical Metallurgy and Materials Science **14**, 521 (1983).

[223] H. Conrad, Metallurgical and Materials Transactions A: Physical Metallurgy and Materials Science **35A**, 2681 (2004).

[224] B. Cai, Q. P. Kong, L. Lu, and K. Lu, Scripta Materialia **41**, 755 (1999).

[225] V. Yamakov, D. Wolf, S. R. Phillpot, and H. Gleiter, Acta Materialia **50**, 61 (2002).

[226] R. L. Coble, Journal of Applied Physics **34**, 1679 (1963).

[227] D. L. Wang, Q. P. Kon, and J. P. Shui, Scripta Metallurgica et Materialia **31**, 47 (1994).

[228] J. Deng, D. L. Wang, Q. P. Kong, and J. P. Shui, Scripta Metallurgica et Materialia **32**, 349 (1995).

[229] P. G. Sanders, M. Rittner, E. Kiedaisch, J. R. Weertman, H. Kung, and Y. C. Lu, Nanostructured Materials **9**, 433 (1997).

[230] G. W. Nieman, J. R. Weertman, and R. W. Siegel, Journal of Materials Research **6**, 1012 (1991).

[231] P. Keblinski, D. Wolf, and H. Gleiter, Interface Science **6**, 205 (1998).

[232] A. J. Haslam, V. Yamakov, D. Moldovan, D. Wolf, S. R. Phillpot, and H. Gleiter, Acta Materialia **52**, 1971 (2004).

[233] A. P. Gerlich, L. Yue, P. F. Mendez, and H. Zhang, Acta Materialia **58**, 2176 (2010).

[234] W. L. Chan, R. S. Averback, and Y. Ashkenazy, Physical Review B **82**, 020201 (2010).

[235] D. Gupta, Metallurgical Transactions A-physical Metallurgy and Materials Science **8**, 1431 (1977).

[236] A. Kuper, H. Letaw, L. Slifkin, E. Sonder, and C. T. Tomizuka, Physical Review **96**, 1224 (1954).

[237] K. Maier, C. Bassani, and W. Schule, Physics Letters A **A 44**, 539 (1973).

[238] H. Zhang, D. J. Srolovitz, J. F. Douglas, and J. A. Warren, Physical Review B **74**, 115404 (2006).

[239] H. Zhang, D. J. Srolovitz, J. F. Douglas, and J. A. Warren, Proceedings of the National Academy of Sciences of the United States of America **106**, 7735 (2009).

[240] K. H. Nagamanasa, S. Gokhale, R. Ganapathy, and A. K. Sood, Proceedings of the National Academy of Sciences of the United States of America **108**, 11323 (2011).

[241] Y. Ritter and K. Albe, Acta Materialia **59**, 7082 (2011).